Numerical simulation of jet impingement cooling of the inside of a hemisphere with application to SCRAP

by

David McDougall

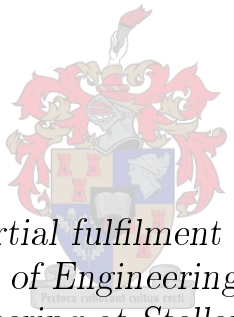

Thesis presented in partial fulfilment of the requirements for the degree of Master of Engineering (Mechanical) in the Faculty of Engineering at Stellenbosch University

Supervisor:	Prof. T.W. von Backström
Co-supervisors:	Dr. M. Lubkoll Prof. A.B. Sebitosi

April 2019

The financial assistance of the National Research Foundation (NRF) towards this research is hereby acknowledged. Opinions expressed and conclusions arrived at, are those of the author and are not necessarily to be attributed to the NRF.

Stellenbosch University https://scholar.sun.ac.za

Declaration

By submitting this thesis electronically, I declare that the entirety of the work contained therein is my own, original work, that I am the sole author thereof (save to the extent explicitly otherwise stated), that reproduction and publication thereof by Stellenbosch University will not infringe any third party rights and that I have not previously in its entirety or in part submitted it for obtaining any qualification.

Date: April 2019 .....

Copyright © 2019 Stellenbosch University
All rights reserved.

Stellenbosch University https://scholar.sun.ac.za

Abstract

Numerical simulation of jet impingement cooling of the inside of a hemisphere with application to SCRAP

D. McDougall

Department of Mechanical and Mechatronic Engineering,
University of Stellenbosch,
Private Bag X1, Matieland 7602, South Africa.

Thesis: MEng (Mech)

April 2019

Conventional concentrating solar power (CSP) plants use Rankine cycles as their thermal power generation cycle. Recent developments have shown the potential for combined cycle (CC) CSP plants to achieve higher efficiencies and lower costs than conventional CSP plants. One configuration of the Brayton cycle of a CC plant is to utilise a pressurised air receiver between the compressor and turbine to offset or omit fuel consumption. The Spiky Central Receiver Air Pre-heater (SCRAP) concept, categorised as a metallic tubular pressurised air receiver, has been shown to exhibit promising performance for the purpose of pre-heating the air stream prior to it entering a combustion chamber or cascading secondary receiver.

The receiver's absorber assemblies, the so-called spikes, are designed to transfer the incoming solar radiation energy to the pressurised air stream. With the hemisphere of the spike tip exposed to the solar field, it experiences the highest flux with the maximum expected at the hemisphere's centre. Jet impingement is employed here because the elevated local heat transfer around the maximum flux region cools the receiver material, which reduces external thermal losses. A reduced maximum temperature also permits a wider range of materials.

This thesis presents further insight into the local heat transfer characteristics and fluid mechanical properties of the spike tip jet impingement, which is critical to the concept feasibility. Impingement cooling, in the context of a Brayton cycle, presents a trade-off between the internal pressure drop and the external heat losses.

To analyse the local heat transfer characteristics of the cooling mechanism in the SCRAP receiver, a computational fluid dynamics (CFD) model was

Stellenbosch University https://scholar.sun.ac.za

developed and validated against experimental data, from literature, of a flow field of a similar nature. It was found that the three-equation k-ω SST RANS turbulence model, with the intermittency transition extension, performs well at predicting the Nusselt number surface distributions for designs with dimensionless characteristics similar to those of the SCRAP receiver's spike tip. Area-weighted averages of the distributions were predicted within 10 % of the experimental results from literature.

It was identified that adding a nozzle to the spike tip is necessary to achieve the required cooling of the spike tip, which experiences highly concentrated solar flux. Using the validated CFD model, a detailed parametric analysis was conducted to characterise the jet impingement cooling capabilities in the spike tip of SCRAP. It was found that the nozzle diameter is the most sensitive geometric parameter. Decreasing the nozzle diameter drastically increases pressure drop. However, this accelerates the fluid, which significantly increases heat transfer.

The pressure drop and thermal efficiency of a pressurised air receiver both affect the Brayton cycle efficiency. For this reason, a method of calculating a cycle efficiency that considers receiver pressure drop and thermal losses was suggested. The resulting efficiency is a quantity that permits a trade-off between heat transfer and pressure drop. A set of design points with varying nozzle diameters, d, showed that a maximum cycle efficiency is achieved for $10\,\text{mm} \leq d \leq 12\,\text{mm}$. The suggested efficiency quantification tool can be used in further work for design analyses of solarised gas turbines.

Stellenbosch University https://scholar.sun.ac.za

Uittreksel

Numeriese simulasie van straalversnelling afkoeling van die binnekant van 'n halfrond met toepassing op SCRAP

("Numerical simulation of jet impingement cooling of the inside of a hemisphere with application to SCRAP")

D. McDougall

Departement Meganiese en Megatroniese Ingenieurswese,
Universiteit van Stellenbosch,
Privaatsak X1, Matieland 7602, Suid Afrika.

Tesis: MIng (Meg)

April 2019

Konvensionele gekonsentreerde sonkrag (GSK) stasies maak gebruik van die Rankine siklus as die termiese kragopwekking siklus. Onlangse ontwikkelings vir gekombineerde siklus (GS) GSK stasies het potensiaal getoon om hoër doeltreffendheid teen 'n laer koste as konvensionele GSK stasies te behaal. Een aspek van die Brayton-siklus van 'n GS-aanleg is om 'n hoëdruk lugontvanger tussen die kompressor en turbine te gebruik om brandstofverbruik te verskuif of vry te spring. Die Stekelrige Sentrale Ontvanger Lug Voorverwarmer (SCRAP) konsep, gekategoriseer as 'n metaalbuis hoëdruk lug ontvanger, het belowende verrigting getoon vir die doel om die lugstroom te voorverhit voordat dit die verbrandingskamer of inlyn sekondêre ontvanger binnegaan.

Die ontvanger se absorpsie-samestellings, die sogenaamde spikes, is ontwerp om die inkomende stralingsenergie van die son na die hoëdruk lugstroom oor te dra. Met die halfrond van die spitspunt wat aan die sonveld blootgestel word, ervaar dit die hoogste hitte-vloed met die maksimum wat by die middelpunt van die halfrond verwag word. Straal botsing word hier ingespan omdat die verhoogde plaaslike hitte-oordrag rondom die maksimum vloedgebied die ontvangermateriaal afkoel, wat eksterne termiese verliese verminder. 'n Verlaagde maksimum temperatuur laat ook 'n wyer verskeidenheid materiale toe.

Hierdie proefskrif bied 'n verdere insig in die plaaslike hitte-oordrag eienskappe en vloei-meganiese eienskappe van die spitspunt straalbotsing wat krities is vir die konsep haalbaarheid. Straalbotsing verkoeling in die konteks

Stellenbosch University https://scholar.sun.ac.za

van 'n Brayton siklus bied 'n oorweging tussen die interne drukval en eksterne hitteverliese.

Om die plaaslike hitte-oordrag eienskappe van die verkoelingsmeganisme in die SCRAP ontvanger te ontleed, is 'n berekeningsvloeistofdinamika (CFD) model ontwikkel en bevestig teen eksperimentele data uit die literatuur van 'n vloeibare veld van soortgelyke aard. Daar is bevind dat die drievergelyking k-ω SST RANS turbulensie model met die afwisseldende oorgang uitbreiding goed vaar met die voorspelling van die Nusselt nommer oppervlakverdelings vir ontwerpe met dimensielose eienskappe soortgelyk aan dié van die SCRAP ontvanger se spitspunt. Gebied-geweegde gemiddeldes van die verspreidings is voorspel binne 10 % van die eksperimentele resultate uit literatuur.

Dit is vasgestel dat die toevoeging van 'n spuitstuk aan die spitspunt nodig is om die vereiste verkoeling van die spitspunt te behaal wat hoogs gekonsentreerde hittevloed van die son sal ervaar. Met behulp van die bevestigde CFD model, is 'n gedetailleerde parametriese analise uitgevoer om die straal botsing in die spitspunt van SCRAP te beskryf. Daar is bevind dat die spuitdiameter die sensitiefste geometriese parameter is. Vermindering in die spuitstuk diameter verhoog drasties die drukval, maar dit versnel die vloeistof wat hitte-oordrag aansienlik verhoog.

Die drukval en die termiese doeltreffendheid van 'n hoëdruk lugontvanger het 'n invloed op die Brayton-siklus doeltreffendheid. Om hierdie rede is 'n metode vir die berekening van 'n siklusdoeltreffendheid voorgestel, wat die ontvanger se drukval en termiese verliese in ag neem. Die gevolglike doeltreffendheid is 'n hoeveelheid wat 'n afwisseling tussen hitte-oordrag en drukval moontlik maak. 'n Stel ontwerppunte met veranderedne spuitstuk diameters, d, het getoon dat 'n maksimum siklusdoeltreffendheid word behaal vir $10\,\text{mm} \leq d \leq 12\,\text{mm}$. Die voorgestelde doeltreffendheid kwantifisering instrument kan gebruik word in verdere werk vir ontwerp ontledings van sonkrag gasturbines.

Stellenbosch University https://scholar.sun.ac.za

Acknowledgements

I would like to express my sincere gratitude to the following people and organisations:

- Prof von Backström for his enthusiasm and continued support,
- Dr Lubkoll for his invaluable contribution and mentorship,
- Prof Sebitosi for his useful guidance,
- STERG for the research environment and cohesion,
- My STERG colleagues for friendship and helpful research conversations,
- My family and friends for advice, love, encouragement and prayers,
- Judy McDougall, my mom, for editing my thesis so willingly,
- The NRF for their financial support, and
- Stellenbosch University's Rhasatsha high performance computer (HPC) for its computational power (http://www.sun.ac.za/hpc).

Stellenbosch University https://scholar.sun.ac.za

Dedications

This thesis is dedicated to my Lord and saviour, Jesus Christ. Only through His strength and guidance, was this possible.

Stellenbosch University https://scholar.sun.ac.za

Contents

Stellenbosch University https://scholar.sun.ac.za

Stellenbosch University https://scholar.sun.ac.za

List of Figures

Stellenbosch University https://scholar.sun.ac.za

Stellenbosch University https://scholar.sun.ac.za

List of Tables

Stellenbosch University https://scholar.sun.ac.za

Nomenclature

Constants

$\sigma =$ $5.6703 \times 10^{-8}\,\mathrm{W/(m^2\,K^4)}$

Abbreviations

BC	Boundary condition
BSL	Baseline
CC	Combined cycle
CFD	Computational fluid dynamics
CPU	Central processing unit
CR	Central receiver
CSP	Concentrating solar power
DNI	Direct normal irradiation
DNS	Direct numerical simulation
EWT	Enhanced wall treatment
HPC	High performance computer
HTF	Heat transfer fluid
LCOE	Levelised cost of electricity
LES	Large eddy simulation
OCGT	Open cycle gas turbine
PC	Personal computer
PV	Photovoltaic
RANS	Reynolds-averaged Navier-Stokes
RNG	Re-normalised group
RSM	Reynolds-stress model
SFC	Specific fuel consumption

Stellenbosch University https://scholar.sun.ac.za

SST Sheer-stress transport

SUNSPOT Stellenbosch University solar power thermodynamic cycle

TUI Text user interface

UDF User-defined function

Variables

A	Area	$[\mathrm{m}^2]$
arg_1	Blending function argument	$[-]$
C	Nu correlation constant	$[-]$
C_f	Skin friction coefficient	$[-]$
c_p	Specific heat capacity	$[\mathrm{kJ/(kg\,K)}]$
C_p	Pressure coefficient	$[-]$
d	Nozzle or pipe diameter	$[\mathrm{m}]$
D	Diameter of the hemispherical impingement surface	$[\mathrm{m}]$
d/D	Curvature intensity	$[-]$
f	Fuel to air ratio	$[-]$
F	View factor	$[-]$
F_1	Blending function	$[-]$
h	Heat transfer coefficient	$[\mathrm{W/(m^2\,K)}]$
I	Turbulent intensity	$[\%]$
k	Thermal conductivity, Turbulent kinetic energy	$[\mathrm{W/(m\,K)}\ ,\ \mathrm{m^2/s^2}]$
L	Nozzle/pipe-to-surface distance	$[\mathrm{m}]$
L_e	Entrance length	$[\mathrm{m}]$
L/d	Dimensionless nozzle/pipe-to-surface distance	$[-]$
$\dot{m}$	Mass flow rate	$[\mathrm{kg/s}]$
m	Pr exponent in Nu correlation	$[-]$
n	Re exponent in Nu correlation	$[-]$
Nu	Nusselt number	$[-]$
p	Pressure	$[\mathrm{Pa}]$
Pr	Prandtl number	$[-]$
$\dot{Q}$	Heat transfer rate	$[\mathrm{W}]$
$\dot{q}''$	Heat flux	$[\mathrm{W/m^2}]$

Stellenbosch University https://scholar.sun.ac.za

q	Thermal energy per unit mass flow	[kg/(kW h)]
Re	Reynolds number (dV/ν)	[−]
r	Radial distance from stagnation point	[m]
r_a	Radial arc length from stagnation point (curved surfaces)	[m]
SFC	Specific fuel consumption	[kg/(kW h)]
T	Temperature	[K]
U	Fluid velocity	[m/s]
V	Velocity	[m/s]
$\bar{V}$	Mean nozzle/pipe exit velocity	[m/s]
w	Work per unit mass flow	[kJ/kg]
y^+	Dimensionless distance from wall	[−]
Z	Jet pipe length	[m]
α	Slope angle of nozzle	[° or rad]
α_{opt}	Absorptivity of receiver surface	[−]
γ	Intermittency or Heat capacity ratio	[−]
ε	Emissivity or Turbulent dissipation rate	[− or m^2/s^3]
ε_{opt}	Emissivity of receiver surface	[−]
η	Efficiency	[−]
θ	End cap surface angle (0 at stagnation point)	[° or rad]
μ	Dynamic viscosity	[kg/(m s)]
ν	Kinematic viscosity	[m^2/s]
ν_t	Eddy-viscosity	[m^2/s]
ξ	Pressure loss coefficient	[−]
ρ	Density	[kg/m^3]
σ	Stefan-Boltzmann constant	[$W/(m^2 K^4)$]
ϕ	An array of constants	[−]
ω	Specific turbulent dissipation rate	[1/s]
Ω	Vorticity	[1/s]

Subscripts

0	Stagnation
a	Ambient

Stellenbosch University https://scholar.sun.ac.za

al	Allowable
avg	Average (area weighted)
b	Combustion
c	Compressor
e	Entrance
exp	Experimental
f	Air
g	Gas
in	Inlet
j	Nozzle/pipe exit
loss	Loss
m	Mechanical
max	Maximum
nat	Natural convection
net	Net
opt	Optical
out	Outlet
rad	Radiation
rec	Receiver
s	Surface
sim	Simulation
sky	Sky
sp	Spike
sol	Solar absorbed
t	Turbine
tc	Turbine to compressor
th	Thermal
tip	Tip
tot	Total
wall	Impingement surface

Stellenbosch University https://scholar.sun.ac.za

Stellenbosch University https://scholar.sun.ac.za

Chapter 1

Introduction

1.1 Background

Renewable energy has, in recent years, seen rapid development towards reducing costs and increasing efficiencies of existing technologies. New innovations in other technologies, such as concentrating solar power (CSP), are also experiencing significant recent growth.

Photovoltaic (PV) energy and wind energy are significant players in the necessary global sustainable energy transition and CSP, although not as widely adopted, has seen rapid growth since 2006. The lag behind other renewable technologies can be attributed to its relatively high levelised cost of electricity (LCOE). In recent years, CSP has become more economically feasible and has developed into a competitive technology in the renewables industry, which has stimulated growth. The global total CSP capacity was less than 500 MW in 2006 (most of it in the Unites States) and had grown to 4.8 GW worldwide by the end of 2016 (Sawin *et al.*, 2017).

CSP is a thermal power generation technology in which heat is obtained by concentrating sunlight. To do this, reflective surfaces (mirrors) are arranged and/or curved to concentrate solar irradiance onto a receiver. The receiver harnesses high temperature thermal energy which is transported via a heat transfer fluid (HTF) to a thermodynamic cycle such as a Rankine cycle. Typically, this thermal energy is captured in synthetic oils or molten salt and exchanged with water/steam to produce electricity through a Rankine cycle such as in a conventional coal-fired power station. CSP power plants conventionally make use of parabolic trough collectors. Developments in central receiver (CR) plants (which involve a field of controlled mirror facets called heliostats that have a point focus at the top of a tower) have further increased efficiencies and the economic feasibility of CSP. A simple flow schematic of a state-of-the-art Rankine cycle CR CSP plant with molten salt thermal storage is shown in Figure 1.1.

Managing an electric grid like South Africa's requires supplying the demand without too much curtailment. To achieve this, the grid should have several different technologies producing power. Some technologies (such as conventional coal-fired power plants) provide a base load, others (such

Stellenbosch University https://scholar.sun.ac.za

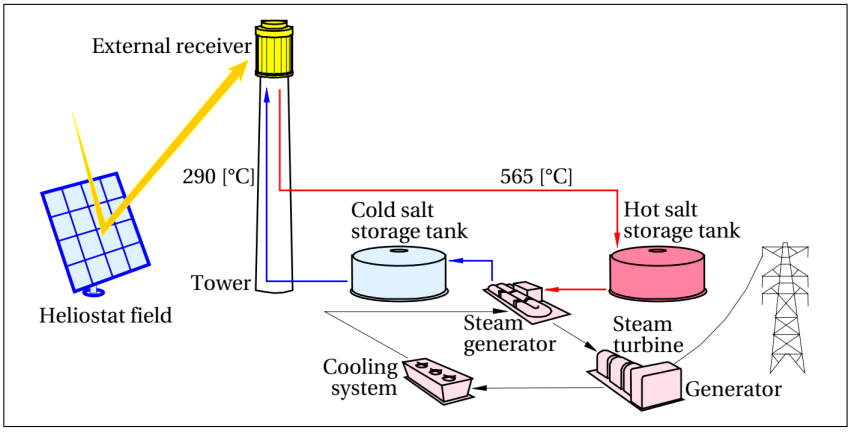

Figure 1.1: Diagram of a typical CSP central receiver Rankine cycle power plant (Augsburger, 2013)

as gas turbines) provide peak load. There are also technologies supplying intermediate load. In an electric grid, the utility operator must manage the suppliers to meet demand without excess curtailment. The grid must have sufficient (with a safety factor) production capacity to meet the highest peak demands.

Gas turbines have rapid response times and can therefore be rapidly commissioned by a utility operator during peak demand periods. A gas turbine typically pressurises ambient air via a compressor, after which fuel is added and the air-fuel mixture is combusted and expanded through a turbine that turns an electric generator. The combustion of fuel simply adds thermal energy to the system. This addition of thermal energy can also be achieved by harnessing concentrated solar energy via a CSP receiver as shown on the left of Figure 1.2. A hybrid solarised gas turbine cycle could provide day-time production with low emissions (solar energy replaces fossil fuel consumption to an extent) and be available for peaking production as a conventional gas turbine.

The Stellenbosch University Solar Power Thermodynamic (SUNSPOT) cycle is a combined cycle (CC) CSP plant concept that is being utilised for several research studies at Stellenbosch University and can be configured in several ways. A CC power plant typically has a conventional open cycle gas turbine (OCGT), also known as a Brayton cycle, and a conventional steam turbine cycle, also known as a Rankine cycle. The exhaust gas from the OCGT contains excess usable heat that is recovered in the boiler stage of the Rankine cycle. Thermal energy storage is a significantly less expensive method of storing energy than electrochemical storage (batteries). The use of thermal energy storage in the SUNSPOT cycle shows the potential for asynchronous production (gas turbine for day-time production and Rankine cycle with stored thermal energy for night-time production).

The configuration of the SUNSPOT cycle shown in Figure 1.2 proposes the use of a pressurised air receiver for the gas turbine (Brayton cycle) with rock bed thermal storage between the Brayton and Rankine cycles (Kröger, 2012).

Stellenbosch University https://scholar.sun.ac.za

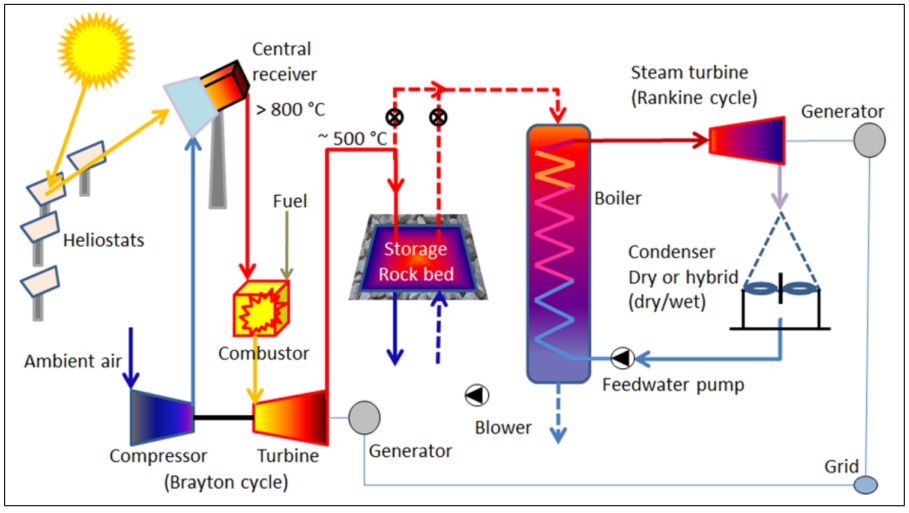

Figure 1.2: Schematic diagram of the SUNSPOT cycle (Kröger, 2012)

A pressurised air receiver could be placed between the compressor and turbine to be used as a pre-heater to offset (or even eliminate) fuel consumption in a hybrid CSP/fuel gas turbine. With the turbo machinery running at full load, the solarised hybrid gas turbine would obtain its thermal input from a combination of the CSP receiver (as a pre-heater) and the combustion of fuel (as a subsidy to obtain the required turbine inlet temperature). The resulting reduction in fuel consumption is desirable for two reasons, namely:

- A reduction in the combustion of natural gas results in a reduction of carbon-equivalent emissions, and
- Solar energy is a free source of energy that can offset fuel expenses.

The Spiky Central Receiver Air Pre-heater (SCRAP) was proposed by Kröger (2008). Lubkoll (2017) conducted an overall performance analysis of this innovative design. It is categorised as a closed volumetric pressurised air receiver. The receiver is proposed to be situated between the compressor and turbine of the Brayton cycle where the compressed air is heated in the multitude of "spikes" (see Figure 1.3) that point toward the heliostats. The performance analysis by Lubkoll (2017) included lab-based experimental work on a single spike and a numerical performance analysis. His research showed that the receiver has high potential, but further work is required to bring the concept to a commercialisable state.

Figure 1.4 shows the air flow in a single spike. The spike is made of two concentric pipes with a concave hemispherical dome (further referred to as the end cap or tip) at the end of it. The inner tube is, at its base, connected to the inner chamber at the top of the tower where the unheated compressed air is distributed into all the spikes. The air exits the inner tube at the spike tip as a jet and impinges against the end cap, cooling the end cap and heating the air. The end cap causes the flow to turn around and enter the finned channels where it continues to absorb heat in channel flow. Exiting the finned section into the outer chamber, the heated air then travels either to the combustion chamber for further heating or directly to the turbine.

Stellenbosch University https://scholar.sun.ac.za

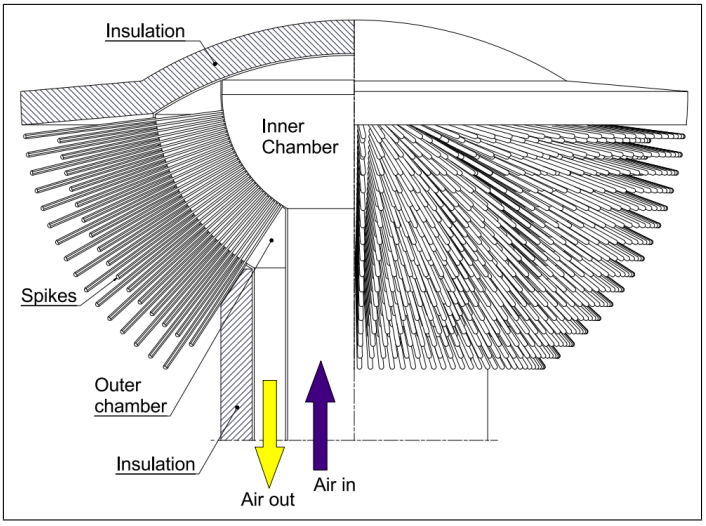

Figure 1.3: A drawing of SCRAP with the left side sectioned (Kröger, 2008)

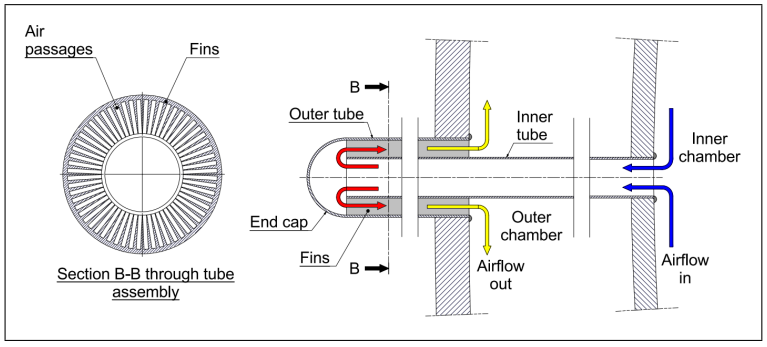

Figure 1.4: A sectioned drawing of the spike showing the air's flow path (Kröger, 2008)

Lubkoll (2017) recommended that further work should be done on the impinging jet cooling in the spike tip. The current study is based on this recommendation to obtain further insight into the local effects of the cooling mechanism, thereby exploring its effects on the performance of the receiver.

1.2 Problem statement

Lubkoll (2017) shows in his ray-tracing analysis that the end cap experiences a solar flux distribution that is at a maximum at its centre and a minimum where it connects to the rest of the spike. This is predominantly due to cosine losses caused by the curvature of the hemisphere, with the assumption of small heliostats for better penetration into the spiky structure. The area that experiences the highest flux requires the most cooling. Introducing a nozzle at the end of the inner tube of the spike causes the flow to accelerate, increasing the heat transfer capabilities of the jet, particularly in the centre where it impinges in the maximum flux region. The exploitation of the excellent heat transfer characteristics of jet impingement to cool the end cap (which

Stellenbosch University https://scholar.sun.ac.za

experiences the maximum solar flux) forms one of the bases of the concept of the SCRAP.

The SCRAP receiver is conceptualised to be a volumetric receiver whereby the maximum surface temperature occurs deep in the structure and surfaces exposed to the surroundings are at a lower temperature than the HTF outlet temperature. This results in a reduction in radiative and convective losses to the surroundings without compromising the outlet temperature of the receiver, and higher efficiencies are thus achievable.

Introducing a nozzle to increase heat transfer at the spike tip will increase the thermal efficiency of the receiver. However, it will induce an increased pressure drop over the receiver which would reduce the efficiency of the gas turbine cycle. The pressure drop caused by introducing a nozzle is due to the flow acceleration and sudden expansion where no venturi diffuser is used to recover the dynamic pressure. The dynamic energy in the jet (high velocity) is what causes the high heat transfer capabilities, so diffusing the jet to recover dynamic pressure reduces the heat transfer coefficient. This describes the fundamental coupling of pressure drop and heat transfer coefficients in thermo-fluid mechanics. They are, however, not coupled linearly and they each affect the gas turbine cycle efficiency to different extents.

Lubkoll (2017) predicted that the thermal efficiency, η_{th}, of the receiver can exceed 80 %. This thermal efficiency does not take pressure drop into account, so to quantify the performance of the receiver for the application to a Brayton cycle, the pressure drop must be considered.

Thermal losses include convection (natural and forced) and radiation losses. The receiver is highly sensitive to wind, even at low wind speeds, due to the large surface area that is exposed to passing wind (Lubkoll, 2017). The conductive losses to the tower are considered to be negligible. With higher material temperatures, radiation losses increase rapidly. Radiative losses (shown in equation 1.1) are proportional to the difference between the fourth powers of the material surface and the equivalent sky temperatures.

$$\dot{q}''_{\text{rad}} = F\varepsilon\sigma(T_{\text{s}}^4 - T_{\text{sky}}^4) \tag{1.1}$$

One way to reduce thermal losses to the surroundings is to reduce the surface temperature of the material that is most exposed to the surroundings. Figure 1.5 shows that the spike tip is the main contributor to radiative losses since its view factor F to ambient is assumed to be 1 (in reality it would be slightly less than 1) and the spike cylinder has a negligible view factor and therefore a negligible contribution to radiative losses.

Reducing the spike tip surface temperature could contribute to the desired volumetric effect, where the receiver surface temperatures are lower than the fluid outlet temperatures. This effect is desirable because of the reduction in radiation losses while still achieving high outlet air temperatures, resulting in high receiver thermal efficiencies (Avila-Marin, 2011). Due to its exposure to the surroundings, the spike tip is the area to focus on when attempting to reduce radiation losses. The material surface temperatures observed by this

Stellenbosch University https://scholar.sun.ac.za

receiver can exceed 1000 °C at the spike tip (Lubkoll, 2017). The performance analysis by Lubkoll (2017) considers 1000 °C as the upper limit so that steel can be a feasible material. Improving the jet impingement cooling at the spike tip reduces material surface temperatures and hence reduces the radiative losses and vulnerability to materials melting or deteriorating.

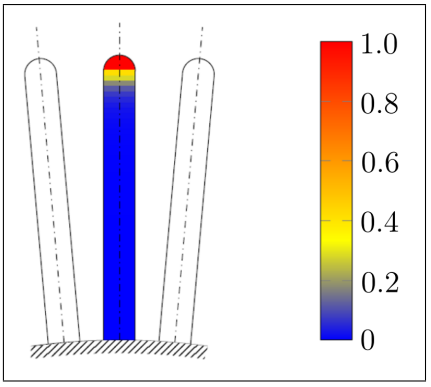

Figure 1.5: Spike view factor or level of exposure to the surroundings (Lubkoll *et al.*, 2015)

A high level computational fluid dynamics (CFD) model was developed by Lubkoll (2017) to determine the effects of adding different size nozzles to the end of the inner pipe. With a constant mass flow rate, a smaller nozzle means higher jet velocity which impinges on the inner surface of the end cap. Lubkoll (2017) observed that the smaller the nozzle diameter, the better the heat transfer and the lower the end cap material temperature, but a decreased nozzle diameter increases pressure drop.

The CFD model developed by Lubkoll (2017) was validated using flat plate experimental results and then extended to the spike tip geometry. The model was used to observe the impinging jet heat transfer characteristics and to understand the effect of the nozzle diameter for his further system modelling. The model validation performed by Lubkoll (2017) was sufficient for his initial performance analysis, but he recommended that a comprehensive validation study be done on developing a better understanding of the local effects in the impinging jet flow at the spike tip. The local effects are important because of the complexity of the flow characteristics causing the heat transfer, and due to the fact that the end cap experiences a flux distribution and requires local cooling.

In summary, the SCRAP receiver's spike tip produces radiation losses due to its high surface temperature. This temperature, and hence the losses, can be reduced by decreasing the nozzle diameter at the inner tube exit, but this comes at the cost of pressure drop. There are a number of geometric changes that can improve the heat transfer characteristics of the spike tip, but a more comprehensive validation study is required for the development of a CFD model. A validated model would allow for further improvements to be made to the spike tip through parametric observations or an optimisation study.

Stellenbosch University https://scholar.sun.ac.za

1.3 Motivation and objectives

This study is divided into two parts. The first part presents the development and validation of a CFD model, using published experimental data, with relevance to the application of the spike tip jet impingement. The second part applies the validated model to the SCRAP receiver with the intention of gaining insight into the geometric and fluid mechanical effects on the receiver's performance.

1.3.1 Numerical model development

The software being utilised is Fluent™ v17.2 from ANSYS Inc. and an effort will be made to best understand the capabilities of the commercial software. Impinging jet flow is a complicated flow field to model numerically. There has been little investigation into the behaviour of an impinging jet on a concave hemispherical surface. In recent publications, McDougall *et al.* (2018) and Craig *et al.* (2018) present some numerical results for jet impingement heat transfer on a concave hemisphere.

The objective of developing a numerical model is to observe the capability of Fluent™ to predict, with an acceptable level of accuracy, the local and average heat transfer characteristics of the highly turbulent jet impingement flow field, using the Reynolds-averaged Navier-Stokes (RANS) turbulence models.

Accurately predicting the turbulent flow using the RANS models will drastically save computational time in comparison to Large-eddy Simulations (LES) or Direct Numerical Simulations (DNS). A successfully validated RANS model would enable the author to perform an extensive parametric analysis on spike tip jet impingement at relatively low computational expense.

1.3.2 Application of model to SCRAP

Lubkoll (2017) introduces the trade-off between pressure drop and heat transfer in the spike tip jet impingement. The smaller the nozzle diameter, the higher the jet impingement heat transfer capability and the higher the pressure drop. Increased heat transfer is desirable for reduced surface temperature (therefore reduced thermal losses to ambient) and higher receiver efficiency, but increased pressure drop is unwanted because it decreases the pressure ratio of the turbine and therefore decreases the gas turbine cycle efficiency. This trade-off forms the basis of part two of the current work.

Given that a sufficiently validated CFD model is developed for concave hemispherical jet impingement, it could be used to study the effects of geometric alterations within the spike tip. A geometric sensitivity study will give insight into the important parameters to consider in a parametric analysis, which would permit the selection of a design that improves the efficiency of a selected gas turbine cycle and even permit an optimisation study to be performed in further work.

The objective of this part is to compare the validated CFD results to Lubkoll (2017), to gain a better understanding of the sensitivity of certain

Stellenbosch University https://scholar.sun.ac.za

nozzle geometric parameters, and to perform a parametric analysis with quantification of the gas turbine cycle efficiency. Within the parametric set, the design point with the maximum gas turbine cycle efficiency (affected by jet impingement heat transfer and pressure drop) is the preferred design. There are also pressure drop limitations in the turbo-machinery and maximum material temperature limitations that are taken into account here.

The insight gained from the parametric analysis as well as the tools presented (CFD model and gas turbine cycle efficiency calculation) will be a step closer to having an in depth understanding of the SCRAP receiver and can be used for further work.

1.4 Methodology

After gaining some insight from the extensive pool of jet impingement literature, a numerical RANS CFD model is developed and validated with relevance to being applied to the SCRAP receiver's spike tip jet impingement. The validation process involves numerically replicating (with the information available) the experimental setup of Lee *et al.* (1999) and determining the capability of Fluent™ RANS turbulence models to replicate the published experimental heat transfer profiles.

The correlation between the experimental and numerical results determines the validity of the model. It is also important to know the model's sensitivities to numerical inputs such as the mesh refinement, the size of the numerical domain and boundary conditions. A sensitivity analysis is therefore presented.

The validated numerical model is then used to determine the validity of the high level CFD model used by Lubkoll (2017). Thereafter the reference geometry and environmental parameters presented by Lubkoll (2017) are replicated with the introduction of a nozzle. This nozzle's geometry can have a significant effect on pressure drop and heat transfer. A sensitivity analysis on some geometric parameters is performed to determine the effect of these parameters. These results lead to a parametric analysis performed to obtain insight into the effect of certain parameters on the efficiency of a gas turbine cycle.

A gas turbine cycle efficiency calculation is presented as a tool with the inclusion of receiver thermal efficiency, pressure drop in the receiver and fuel consumption to get to the required turbine inlet temperature. Assumptions are used with a reference base case to present an example of the benefits of quantifying the performance of the receiver in terms of gas turbine cycle efficiency.

The purpose of the study is not to select improved design parameters for the spike tip, but rather to present a tool that can be used to simulate the complicated spike tip jet impingement. This tool can be used as part of a design improvement study that considers all parameters of the receiver's design and quantifies the receivers performance increase in terms of an improvement to the cycle efficiency of the gas turbine it is a part of.

Stellenbosch University https://scholar.sun.ac.za

Chapter 2

Review of impinging jet cooling

A literature review on the jet impingement cooling mechanism is conducted with the concave hemispherical impingement surface effects in mind. Other necessary literature is reviewed in subsequent chapters where necessary. This review serves to present the necessary background knowledge of jet impingement flow that is relevant to the practical application in question.

2.1 Introduction to jet impingement

Impinging jet cooling involves a confined stream of fluid exiting a nozzle or a pipe as a jet and impinging on a target surface to heat or cool the surface. The fluid either removes heat from or transfers heat to the surface, depending on a positive of negative temperature difference.

A heat transfer coefficient is, in general, affected by: local fluid and solid properties at the interface, a local temperature difference between the fluid and solid, local flow velocity, and local turbulent intensity. The reason that the jet impingement mechanism displays heat transfer coefficients that are superior to most other mechanisms is because of the fact that the fluid is forced against the impingement surface at a high velocity with relatively small boundary layer thickness and high levels of turbulence.

Impinging jet cooling is a commonly used cooling mechanism for engineering applications such as turbine blade cooling (Colucci and Viskanta, 1996), manufacturing processes and cooling of electronic equipment (Behnia *et al.*, 1998) where high heat transfer coefficients are required.

The flow field of an impinging jet consists of three major regions, shown in Figure 2.1. In the free jet region, the jet width increases as it gets further from the nozzle and the average jet velocity decreases. This is due to turbulence being introduced by the entrainment of surrounding fluid into the jet (a mixing region). The stagnation region is where the fluid is forced to change direction from orthogonal to the surface to parallel. The stagnation point is the point on the surface at the centreline of the jet, around which the fluid velocity approaches 0 m/s. The stagnation region ends where the parallel component of the fluid velocity reaches its maximum (where the orthogonal component is 0 m/s). A convective wall jet follows in the wall jet region, further transferring

Stellenbosch University https://scholar.sun.ac.za

heat to or from the surface. Jet energy is further dissipated to the surrounding fluid as the wall jet progresses.

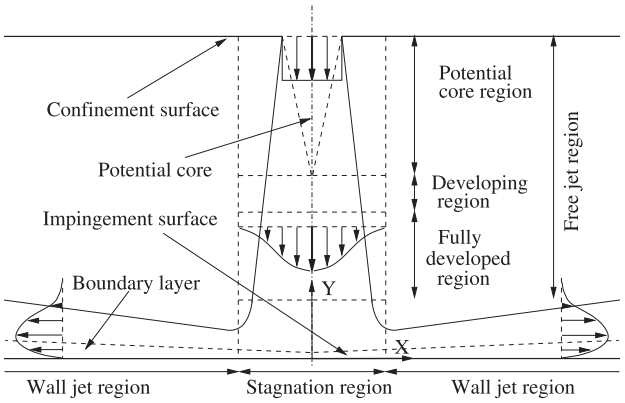

Figure 2.1: A cross section of uniform velocity profile jet impinging on a flat surface (Achari and Das, 2015)

The highly turbulent flow being forced upon the surface, in conjunction with a temperature difference between the fluid and the surface, results in elevated heat transfer coefficients in comparison to other forced convection heat transfer mechanisms.

In the case of the SCRAP receiver, the end cap is subjected to a high solar flux and the purpose of the receiver is that the air flow inside the spikes absorb as much of that heat as possible, while reducing the thermal losses to ambient as much as possible. The design is structured to have a large surface area for heat transfer, hence, the multitude of spikes. Much of the heat transfer occurs in the finned section of the spike, but a substantial air temperature rise is observed due to jet impingement in the spike tip, where heat is transferred from the end cap (the impingement surface) to the compressed air exiting the nozzle at the end of the inner pipe (Lubkoll, 2017).

This review is conducted to better understand the impinging jet cooling mechanism in the context of the SCRAP receiver and how different design parameters or flow conditions affect heat transfer. These design parameters and flow conditions include: Reynolds number, nozzle-to-surface distance, and concave impingement surface. Some geometric sensitivities, the second peak phenomenon, and numerical turbulence modelling of jet impingement are reviewed.

2.2 Reynolds numbers and typical Nusselt numbers

Reynolds numbers mentioned henceforth are based on the nozzle diameter, d, and mean nozzle exit velocity, $\bar{V}$, as $Re = \rho d\bar{V}/\mu$ where ρ is the density and μ is the dynamic viscosity of the fluid at the nozzle exit. Smooth pipe flow is considered turbulent at $Re \geq 2300$ (Faisst and Eckhardt, 2004; Kerswell,

Stellenbosch University https://scholar.sun.ac.za

2005) and free jets are considered turbulent flow for $Re \geq 100$ (Schabel and Martin, 2010).

To characterise the heat transfer between a solid and a fluid, the Nusselt number, Nu, shown in equation 2.1 is typically used. It is the heat transfer coefficient, h, between the solid and fluid, non-dimensionalised by a characteristic length, d, and the thermal conductivity of the fluid, k. The Nu is therefore a measure of the ratio of convective heat transfer, h [W/(m^2 K)], and the conductive heat transfer, k/d [W/(m^2 K)]. The characteristic length, d, in the case of this jet impingement study is the nozzle diameter or jet pipe exit diameter.

$$Nu = hd/k \tag{2.1}$$

The heat transfer coefficient is calculated as shown in equation 2.2 where $\dot{q}''$ is the local surface heat flux on the impingement surface. Notice that the temperature difference in question is between the impingement surface local temperature and the average fluid fluid temperature at the nozzle exit.

$$h = \dot{q}''/(T_\mathrm{s} - T_\mathrm{j}) \tag{2.2}$$

Average surface Nusselt numbers can range from 2 to 1700. Jets from laminar pipe flow with nozzles close to the surface can produce Nusselt numbers from 2 to 20 (Zuckerman and Lior, 2006) while Rahimi *et al.* (2003) observed local Nusselt numbers up to 1700 from a supersonic jet. These are extreme cases of low and high Nusselt numbers, but typically Reynolds numbers of 4000 to 80 000 are used in jet impingement cooling applications with Nusselt numbers ranging from 50 to 200 (Zuckerman and Lior, 2006).

There are several empirical relationships for jet impingement Nusselt numbers and they typically include the Prundtl number, Pr, Reynolds number, Re, and an empirical function, $f(L/d)$, of the ratio of the nozzle-to-surface distance, L, and the nozzle diameter, d. The form of such an empirical relationship is described by Zuckerman and Lior (2006) and shown in equation 2.3 where C, n and m are constants.

$$Nu = C\ Re^n Pr^m f(L/d) \tag{2.3}$$

For flat plate jet impingement, increasing average Nusselt numbers are typically observed when the nozzle-to-surface distance, L, is decreased or when the Reynolds number, Re, is increased. An increased Reynolds number is attributed to an increased mass flow rate, $\dot{m}$, and/or a decreased nozzle diameter, d, (see equation 2.7).

2.3 Second peak phenomenon

A surface Nusselt number plot along the radial direction of a round jet impinging on a flat surface typically has a global maximum at the stagnation point and decreases rapidly along the radial direction. Figure 2.2 shows the typical expected Nu radial distribution from the stagnation point of flat plate

Stellenbosch University https://scholar.sun.ac.za

jet impingement heat transfer. It is common to observe a second peak on such a distribution in certain flow condition ranges. This is observed in Figure 2.2 with a nozzle distance ratio, L/d, of 2.

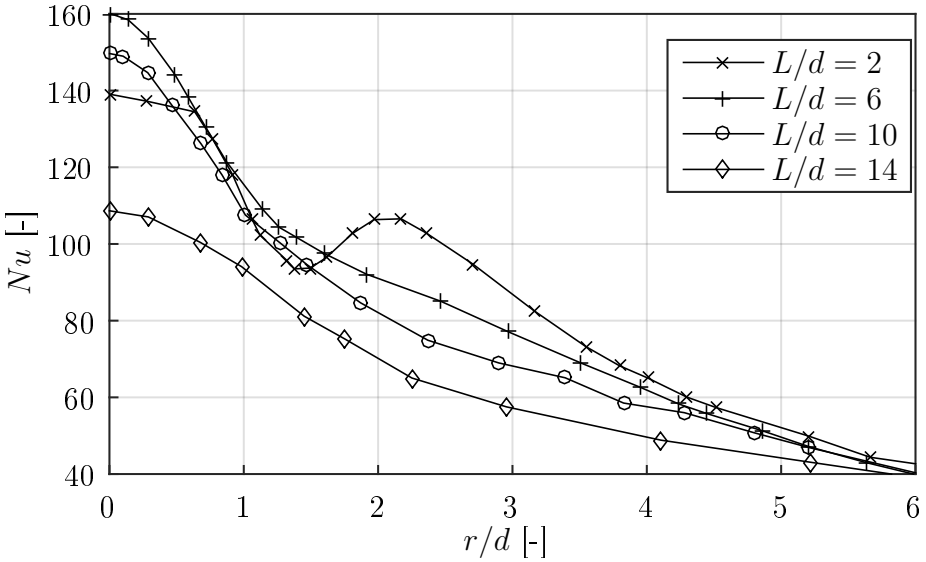

Figure 2.2: Typical flat plate jet impingement Nu distribution from the stagnation point at different nozzle distances from the surface, L, with $Re = 23\,000$ (experimental results by Baughn and Shimizu (1989))

There have been several propositions made by researchers as to the reason for this phenomenon known as the secondary peak. Some early observations before the 21st century led to a number of conclusions. Gardon and Akfirat (1965) state that the secondary peak is due to the thinning of the boundary layer due to the speeding up of the flow as it changes direction, which is accentuated as the nozzle-to-surface distance is decreased. Lytle and Webb (1994), similarly, concludes that the phenomenon is due to a peak in turbulence in the boundary layer because of accelerated flow, but also attributes it to the entrainment of ambient or free-stream fluid into the jet. This changes the fluid temperature and increases heat transfer when the entrainment region impinges the surface. Fox *et al.* (1993) claim that the large eddies generated by the interaction between the jet and the surrounding air introduce vortices to the wall jet, changing the local temperatures and thus causing a secondary peak. Kataoka *et al.* (1987) also determined that the increase in heat transfer is due to the large vortices that affect the flow structure.

With further developments in CFD turbulence models and Large Eddy Simulations (LES) the complexity of jet impingement flow can be observed in more detail for a better understanding. Hadziabdic and Hanjalic (2008) performed LES on jet impingement to better understand the two peaks. They conclude that there is a recirculation of fluid in the region between the two peaks, which is heated, reducing its cooling capability and thus reducing the local Nusselt number. The local minima accentuates the second peak, which is not only due to the recirculation, but also the elevated advection caused

Stellenbosch University https://scholar.sun.ac.za

by accelerated flow in the wall jet. Uddin *et al.* (2013) also performed LES simulations with a particular interest in understanding the secondary peak phenomenon. It was found that there is a region on the impingement surface that experiences "hot" and "cold" spots caused by the surrounding large eddies. This, in conjunction with the accelerated flow that changes the development of the thermal boundary layer, is concluded by Uddin *et al.* (2013) to be the cause of the secondary peak. They further observe that the local second maxima typically occur at $1.4 \leq r/d \leq 2.8$, where r is the local radial distance from the stagnation point.

2.4 Nozzle-to-surface distance and nozzle diameter

The nozzle-to-surface distance, L, does not affect Reynolds number, but the nozzle diameter, d, does. It is seen in equation 2.7 that the Reynolds number is directly proportional to mass flow rate and inversely proportional to the nozzle diameter, d.

$$\dot{m} = \rho A \bar{V} \tag{2.4}$$

$$A = \frac{\pi d^2}{4} \tag{2.5}$$

$$\nu = \frac{\mu}{\rho} \tag{2.6}$$

$$\begin{aligned} Re &= \frac{\bar{V} d}{\nu} \\ &= \frac{\rho \bar{V} d A}{\mu A} \\ &= \frac{\dot{m} d}{\mu \frac{\pi d^2}{4}} \\ &= \frac{\dot{m}}{\mu \frac{\pi d}{4}} \end{aligned} \tag{2.7}$$

The results shown in Figure 2.3 from a study conducted by Lee *et al.* (2004) show the effect of changing nozzle diameters for flat plate impinging jet flow. They conclude that an increasing nozzle diameter produces higher heat transfer at and around the stagnation point, with negligible differences observed down-stream at radius-to-diameter ratios $r/d > 0.5$. It is noted that for practical applications, this does not mean that a larger nozzle is better, because increasing the nozzle diameter means the mass flow rate must increase to achieve a constant Reynolds number.

Lee *et al.* (1997, 2004) and Kataoka *et al.* (1987) found that the maximum stagnation point Nusselt number is achieved at a nozzle-to-surface distance of $L/d \approx 7$ on a flat plate.

Stellenbosch University https://scholar.sun.ac.za

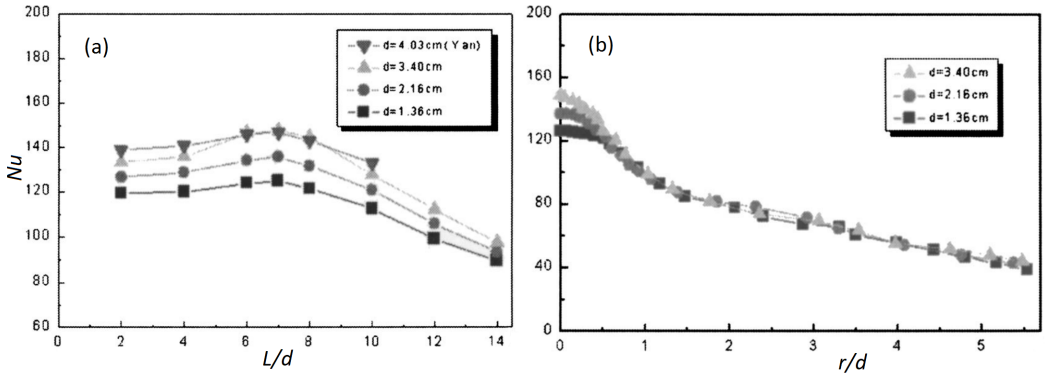

Figure 2.3: Impinging jet Nusselt numbers at $Re = 23\,000$ (a) Stagnation point Nusselt numbers for different nozzle diameters and nozzle-to-surface distances (b) Radial Nusselt number distribution for different nozzle diameters at $L/d = 6$ (Lee *et al.*, 2004; Yan, 1993)

2.5 Concave surface effects

Most of the available literature on jet impingement heat transfer refers to flat plate impingement. The geometry of the SCRAP receiver end cap is a hemisphere and the curvature of the surface affects the flow structure and heat transfer. It is assumed that the surface curvature acts against the fluid's inertia and helps prevent separation.

Sharif and Mothe (2010) states that surface curvature is able to increase average heat transfer rates by up to 20 % in comparison to flat plates. The curvature intensity, d/D (the ratio of nozzle diameter, d, and curved surface diameter, D), has a significant effect on the average heat transfer rate. Öztekin *et al.* (2013) studied this effect with a slot jet impinging on a concave trough. Different curvature intensities were tested and it was found that there is an optimal curvature intensity that results in a maximum Nu_{avg}. The average Nusselt numbers produced by the flat plate (curvature intensity of $d/D = 0$) were significantly less than the curved plates. The curvature effect (forced change of flow inertia due to the curvature) is also said to be accentuated with increasing Reynolds numbers (Yang *et al.*, 1999).

The increased heat transfer capabilities are attributed to the effect that the curvature has on the development of the turbulent boundary layer. The boundary layer is destabilised by Taylor-Görtler vortices, caused by centrifugal forces, which increases turbulent intensity and, hence, heat transfer characteristics (Thomann, 1968).

Gau and Chung (1991) developed two empirical formulae for the average Nusselt number of a 2D slot jet on a concave semi-circular trough surface shown in equations 2.8 and 2.9. The formulae are similar to the form of equation 2.3 with the addition of the curvature intensity.

$$Nu_{\text{avg}} = 0.251 Re^{0.68} (D/d)^{-0.38} (L/d)^{0.15} \quad \text{for} \begin{cases} 6000 \leq Re \leq 35\,000 \\ 8 \leq D/d \leq 45.7 \\ 2 \leq L/d \leq 8 \end{cases} \tag{2.8}$$

Stellenbosch University https://scholar.sun.ac.za

$$Nu_{\text{avg}} = 0.394 Re^{0.68} (D/d)^{-0.38} (L/d)^{-0.32} \quad \text{for} \begin{cases} 6000 \leq Re \leq 35\,000 \\ 8 \leq D/d \leq 45.7 \\ 8 \leq L/d \leq 16 \end{cases} \tag{2.9}$$

An experimental study on concave hemispherical jet impingement heat transfer was conducted by Lee *et al.* (1999). This is, to the author's knowledge, the only study done on an axisymmetric concave geometry (other research involving concave surfaces are typically on 2-d slot jets on troughs).

In order to understand the parametric sensitivity, Lee *et al.* (1999) studied 45 different cases. Some of the geometries and flow conditions are similar to that of the SCRAP receiver tip. It is because of these similarities that these experimental results have been selected as the validation case for developing a numerical model. Their experimental setup and results are further introduced in section 3.1.

2.6 Numerical turbulence models

The flow field of an impinging jet is known to have complex structures with a high level of turbulence and large scale eddies. The vast range of complexities from stagnant flow to large eddies to wall boundary layers brings uncertainties and difficulties when utilising RANS turbulence models, but there are several cases in literature where RANS models produce adequate predictions of flow and heat transfer characterisation.

The RANS models of interest for jet impingement include the standard $k-\varepsilon$, re-normalised group (RNG) k-ε, realisable k-ε, standard k-ω, sheer-stress transport (SST) k-ω, Reynolds-stress (RSM) and v^2f models. The intricacies of the numerical models are not studied in detail in the scope of this report, but previous researchers have reviewed the advantages and disadvantages of these models in the context of jet impingement flow.

Using a variation of the standard k-ε model, Cooper *et al.* (1993) found that the turbulent kinetic energy, k, around the stagnation point, is over-predicted by an order of magnitude. This results in too much entrainment of the free-stream fluid, reducing the jet's momentum and causing the flow acceleration into the wall jet to be reduced. As a result, the wall jet boundary layer is thicker and hence less heat transfer occurs in the wall jet region.

RNG k-ε has additional terms in its transport equations for k and ε that the standard k-ε does not have (Yakhot and Orszag, 1987). Behnia *et al.* (1998) compared the standard and RNG k-ε models with the v^2f model. The v^2f is similar to the standard k-ε, but it does not require any wall functions as it is valid in the boundary layer (Behnia *et al.*, 1998). It was found that the RNG and standard k-ε models produce similar results, with the re-normalised coefficients not improving the over-predicted turbulence. A significant improvement in flow and heat transfer prediction with the v^2f model in comparison to the k-ε model is found, with v^2f results in good agreement with experimental results. The v^2f model is unfortunately not used in this research because it is no longer available on the student license or university

Stellenbosch University https://scholar.sun.ac.za

academic license server. Special permission is required for the activation of the model.

A study on several variations of the k-ε and k-ω models (excluding SST hybrids) was done by Jarmillo *et al.* (2012). They conclude that the k-ω, in general, is better at predicting jet impingement flow than the k-ε. They also performed Direct Normal Simulations (DNSs) which, understandably, produced better results that the RANS turbulence models. It was, however, found that the variation of the k-ω model that Yap (1987) proposed, has good agreement with the DNS and experimental results.

RANS turbulence models are pursued and developed because of the computational time that is saved in comparison to LES or DNS. Later, in 2005, Angioletti *et al.* (2005) compares three of the better impinging jet models, namely, RNG k-ε, SST k-ω and RSM, using version 6.0 of the Fluent™ commercial software. This study was done on Re in the transition regime from 1000 to 4000 and found that SST k-ω is better for the lower end of the range of Re while RNG k-ε and RSM are better for the higher Re.

Zuckerman and Lior (2006) reviewed the accuracy and computational costs of the k-ε, k-ω, algebraic stress, RSM, SST, v^2f, DNS and LES models of predicting flat plate impinging jet heat transfer. LES and DNS models are the most accurate, but the transient nature of the solution method makes the computational time one to two orders of magnitude more than that of the RANS models. The best compromise between accuracy and speed is concluded by Zuckerman and Lior (2006) to be the SST or v^2f models.

Rama Kumar and Prasad (2008) used the SST k-ω model in FLUENT™ v6.2.16 for jet impingement of a row of jets on a concave semi-cylinder. This flow field entails interference between the jets in the axial direction of the semi-cylinder, but is expected to exhibit similar characteristics to the axisymmetric flow seen in the SCRAP spike-tip. Of the jet impingement CFD work published up to the date of this report, the work by Rama Kumar and Prasad (2008) has, to the author's knowledge, the closest resemblance to the geometry and flow characteristics of the SCRAP's jet impingement flow. They find that the results produced by the SST k-ω model are in good agreement with the empirical correlations.

Furthermore, Caggese *et al.* (2013) follow the recommendation of Zuckerman and Lior (2006) and use the SST k-ω model. Their results show good experimental agreement[1], with the exception of poor agreement when $L/d = 0.5$, which is out of the parametric scope of the validation and application of the present study.

There are several published works on LES and DNS transient simulation of jet impingement that often, as expected, outperform the RANS turbulence models. One such example is the LES simulations conducted by Uddin *et al.* (2013) who, as mentioned in section 2.3, study the phenomenon of the secondary Nu peak. While these transient simulations produce excellent

[1] Agreement is within 10 % for area-weighted average Nu (Nu_{avg}) and 7 % to 8 % for stagnation point Nu (Nu_0)

Stellenbosch University https://scholar.sun.ac.za

results, they require immense computational time relative to RANS turbulence modelling. The purpose of this study is to determine the adequacy of the RANS models in predicting concave hemispherical jet impingement with relatively little computational time. The transient models are therefore not further reviewed.

Commercial software developers such as ANSYS Inc. who develop FLUENT™ have customer support that offers technical assistance with their software packages. They are often challenged by problems that customers present that the software isn't capable of solving. In such a case, the company will often use it as an opportunity to improve the numerical models or make other appropriate improvements. These commercial packages are therefore constantly improving and releasing new versions. In 2016, ANSYS reported on the results of the newly-implemented mechanism in the SST k-ω model. The model produced good correlation with experimental data, including excellent secondary Nu peak prediction (ANSYS, 2016).

2.7 Conclusion

The study of impinging jet flow is a significantly large field of study with a vast collection of literature. The heat transfer mechanism's flow field entails a number of complex characteristics that are evidently difficult to model numerically.

In summary, a higher Reynolds number yields better heat transfer (whether a higher mass flow rate is selected or a smaller nozzle). The optimal dimensionless nozzle-to-surface distance is $L/d \approx 7$ for a flat plate (Lee *et al.*, 1997, 2004; Kataoka *et al.*, 1987) and is found by Lee *et al.* (1999) to be $6 \leq L/d \leq 8$ on a concave hemisphere. If the concave hemisphere diameter D is constant, as is the case in this study, the optimal curvature intensity d/D is only achievable by varying the nozzle diameter d.

It is observed that the SST k-ω model seems to be the preferred numerical model for jet impingement flow predictions, but no literature seems to exist that demonstrates this model's suitability for jet impingement on a concave hemispherical surface.

This review of some of the literature, in the context of the SCRAP's spike tip jet impingement cooling presents a background knowledge of some of the flow complexities, parametric sensitivities and numerical models that will be utilised and further referred to in this analysis.

Stellenbosch University https://scholar.sun.ac.za

Chapter 3

Setup of numerical model validation[1]

CFD RANS modelling is typically used to model turbulent flow with Reynolds decomposition, first proposed by Reynolds (1895), which separates the time-averaged and time-fluctuating components of the fluid flow. The resulting equations, based on the Navier-Stokes equations, form the numerical RANS turbulence models that are used to approximate time-averaged solutions to turbulent fluid flow. The numerical predictions of flow fields and heat transfer with CFD is done by discretising the flow domain, applying boundary conditions to that domain and solving a set of equations within the specified discretised numerical environment.

The usability of a CFD model increased by validating it against analytical solutions, experimental data or empirical correlations. This chapter presents the setup of a RANS numerical environment (further referred to as the model) in which a suitable experimental case study by Lee *et al.* (1999) will be numerically replicated. In the following chapter, the numerical prediction results will be compared to the published experimental results to determine the model's sensitivities and its accuracy[2].

Some of the experimental parameters are outside of the scope of the characteristics of SCRAP, nonetheless all of the parameters are analysed to determine the limitations of the model over a wider range of flow characteristics.

3.1 Experimental validation case study

The end cap of the SCRAP receiver is exposed to a non-uniform solar flux distribution. The flux distribution in combination with the expectation of a secondary peak in heat transfer and other localised heat transfer effects of impinging jets can lead to substantial temperature differentials over the end

[1] Parts of this chapter have been published in McDougall *et al.* (2018)

[2] A number of uncertainties with regard to the experimental environment will be reported in this chapter. The author has attempted to establish contact with Lee *et al.* (1999), but was not successful. The uncertainties are reported for completeness sake, but are not deemed to impact on the results reported herein.

Stellenbosch University https://scholar.sun.ac.za

cap surface. Local effects are vital in determining localised radiation losses and material limitations. It is therefore imperative to validate the local effects.

The experimental setup developed by Lubkoll *et al.* (2016) was designed to be modular for further alternative experimentation on a single spike and it is available for use by the author. The dome (end cap) at the tip of the spike can be placed in the steam chamber in order to determine average heat transfer coefficients and pressure drops of the impinging jet flow with varying pipe diameters. However, an average heat transfer coefficient is considered insufficient for the current validation process because it does not capture the necessary localised effects. For this reason, it was decided that for the scope of this study, no experiments would be conducted and the results from Lee *et al.* (1999) are to be used as a case study to develop and validate a CFD model that can be applied to spike tip jet impingement predictions. The details of the experimental case study (Lee *et al.*, 1999) are henceforth introduced.

While plenty of experimental and numerical publications have been made on jet impingement, they are typically confined to applying a jet to a standard flat plate or curved trough impingement surface. Lee *et al.* (1999) conducted experiments on an impinging jet on a concave hemispherical surface to determine the effect of several parameters on heat transfer. Their methodology is sound and their non-dimensional geometric and flow parameters are similar to that of the SCRAP spike tip characteristics. This experimental case study is therefore chosen as the validation case study for the present work.

As seen in Figure 3.1, the impingement surface had a thermochromic liquid crystal layer that changed colour locally according to its temperature. A layer of resistive metal was used to induce a uniform heat flux to the concave hemisphere, with the back side insulated. A camera captured images that were analysed by a computer to produce isotherm maps of the surface. These were used to calculate local Nusselt number distributions from the stagnation point. This remote temperature measurement technique was described by Lee *et al.* (1994) and Lee *et al.* (1995). They estimated that the Nusselt numbers presented have a maximum uncertainty of 4.5 %.

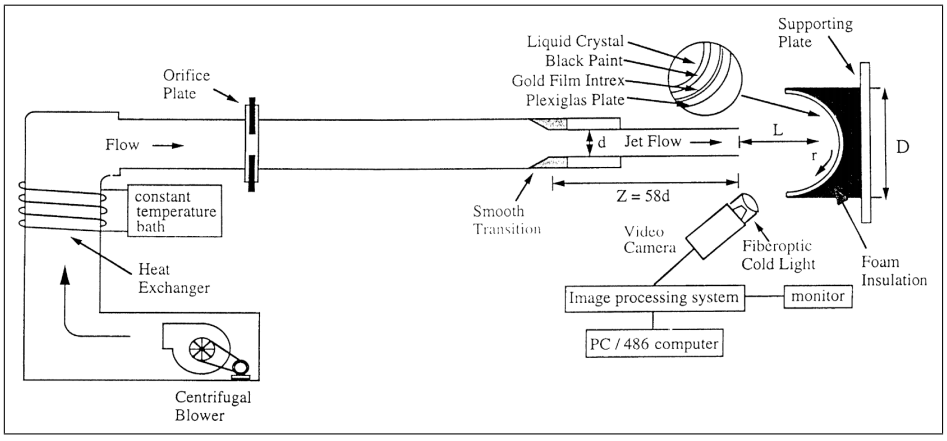

Figure 3.1: A schematic diagram of the concave surface jet impingement experimental setup (Lee *et al.*, 1999)

Stellenbosch University https://scholar.sun.ac.za

The heat transfer coefficient, h, can be expressed as

$$h = \dot{q}''/\Delta T \tag{3.1}$$

where $\dot{q}''$ is the local surface heat flux and ΔT is the difference between the local wall surface temperature and the jet pipe exit temperature $(T_\mathrm{s} - T_\mathrm{j})$. The Nusselt number, $Nu = hd/k$, can therefore be expressed as

$$Nu = \frac{\dot{q}''\, d}{(T_\mathrm{s} - T_\mathrm{j})k_\mathrm{j}} \tag{3.2}$$

with k_e being the thermal conductivity of the fluid exiting at the pipe exit.

It was not specified by Lee *et al.* (1999) which thermal conductivity, k_e, was used (pipe exit or local film temperature), but it is assumed, by the analysis of the results in chapter 4, that they evaluated k_e at the pipe exit temperature, T_e.

The heat flux, $\dot{q}''$, and jet pipe diameter, d, were known input parameters while pipe exit temperature, T_e, was kept within 0.2 °C of ambient temperature, and thermal conductivity, k_e, was determined by T_e. Local surface temperature distributions were measured and therefore local Nusselt numbers were calculated using equation 3.2. It was also noted that the nature of the thermochromic liquid crystal layer was such that the isotherm maps attained were essentially time-averaged (at steady state) because the liquid crystal surface took some time to change colour.

3.2 Parametrisation of geometry and mesh

The CFD analysis is carried out with the commercial software, ANSYS Fluent™ v17.2. The software offers an option to solve the cylindrical coordinate form of the equations for a 2-d geometry. This results in the assumption of axisymmetry about the specified axis. Half of a cross section of the axisymmetric flow field is modelled as shown in Figure 3.2. The 2-d simplification drastically reduces the computational time in comparison to a 3-d model. It is noted that the 2-d cylindrical coordinate forms of the governing equations do not model turbulence in the azimuthal direction (about the axis). It is assumed that the azimuthal turbulence has a negligible effect on the jet's cooling effect because the momentum in the axial and radial directions outweigh the momentum in the azimuthal direction significantly. This assumption will be conservatively reviewed in the analysis of results.

The following three parameters were altered in the experiments by Lee *et al.* (1999):

- Jet pipe diameter, d (three variations)
- Dimensionless pipe-to-surface distance, L/d (five variations)
- Reynolds number, Re (three variations)

A single hemispherical surface was used with a diameter $D = 381\,\mathrm{mm}$ in conjunction with jet pipe diameters, d, of 13 mm, 21.5 mm and 34 mm to simulate varying curvature intensities, d/D. Three jet pipes were used, each

Stellenbosch University https://scholar.sun.ac.za

long enough ($Z = 58d$) to allow the flow to fully develop before exiting. For each jet diameter, five different dimensionless pipe-to-surface distances were studied ($L/d = \{2; 4; 6; 8; 10\}$). These 15 combinations were studied at three Reynolds numbers ($Re = \{11\,000; 23\,000; 50\,000\}$) bringing the total number of configurations to 45. For referring to the different configurations, the naming convention shown in Table 3.1 is henceforth used.

Table 3.1: Naming convention for the 45 experimental cases

$Re = 11\,000$					
d [mm]	$L/d = 2$	$L/d = 4$	$L/d = 6$	$L/d = 8$	$L/d = 10$
13	L2_d1_11	L4_d1_11	L6_d1_11	L8_d1_11	L10_d1_11
21.5	L2_d2_11	L4_d2_11	L6_d2_11	L8_d2_11	L10_d2_11
34	L2_d3_11	L4_d3_11	L6_d3_11	L8_d3_11	L10_d3_11
$Re = 23\,000$					
d [mm]	$L/d = 2$	$L/d = 4$	$L/d = 6$	$L/d = 8$	$L/d = 10$
13	L2_d1_23	L4_d1_23	L6_d1_23	L8_d1_23	L10_d1_23
21.5	L2_d2_23	L4_d2_23	L6_d2_23	L8_d2_23	L10_d2_23
34	L2_d3_23	L4_d3_23	L6_d3_23	L8_d3_23	L10_d3_23
$Re = 50\,000$					
d [mm]	$L/d = 2$	$L/d = 4$	$L/d = 6$	$L/d = 8$	$L/d = 10$
13	L2_d1_50	L4_d1_50	L6_d1_50	L8_d1_50	L10_d1_50
21.5	L2_d2_50	L4_d2_50	L6_d2_50	L8_d2_50	L10_d2_50
34	L2_d3_50	L4_d3_50	L6_d3_50	L8_d3_50	L10_d3_50

Lee *et al.* (1999) published the following results that are useful for validation of a numerical model:

- The stagnation point Nusselt numbers, Nu_0, for all 45 configurations
- The radial distribution of the pressure coefficient for all five pipe-to-surface distances where $Re = 23\,000$ and $d = 34\,\text{mm}$
- Radial Nusselt number distributions for 27 of the 45 configurations (combinations of all three Reynolds numbers, all three jet pipe diameters, and three of the five pipe-to-surface distances, $L/d = \{2; 4; 10\}$)

The geometry and flow conditions are replicated in a CFD model in an attempt to simulate the flow field numerically. The validity of the CFD model is quantified by the correlation between numerical and experimental results, ignoring experimental uncertainties.

There are nine different geometries (combinations of the three jet pipe diameters and the three dimensionless pipe-to-surface distances). Meshes are generated for all nine geometries. To be able to automatically generate these nine geometries and meshes, the geometry and mesh settings are parametrised and interpolated to result in the required cell sizes for each case. These geometries are simulated for all three Reynolds numbers, resulting in a parametric set of 27 simulations.

Stellenbosch University https://scholar.sun.ac.za

Several iterations of different meshes and geometric setups were developed in an attempt to reduce cell counts while retaining a good quality mesh (i.e. mesh refinement in areas with higher flow gradients). The iterative process was part of the mesh independence study described in section 3.8.

Figure 3.2 shows the final iteration, some geometric dimensions, the division of the computational domain into five segments, and the boundary conditions applied (which are further discussed in section 3.3). The parametrised geometric variables are: the jet pipe radius ($d/2$), the entrance length (L_e), and the pipe-to-surface distances (L). The hemisphere diameter D, the exit domain length of 100 mm, and the segment angle of 10° are constants[3]. The dimension along the curved surface starting at the stagnation point is defined as the stream-wise distance from the stagnation point, or arc length, and it is symbolised as r_a.

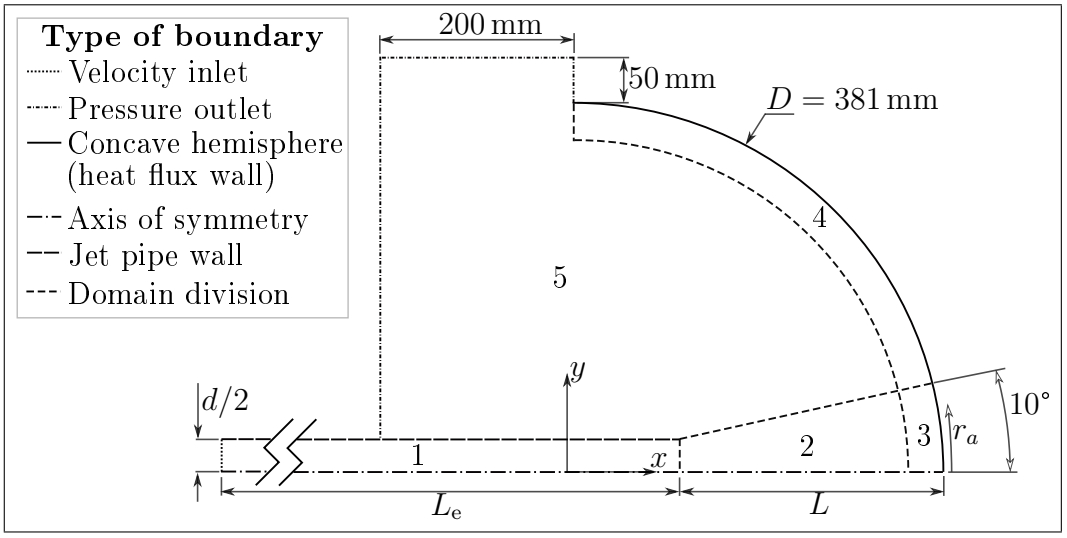

Figure 3.2: Geometric parameters and mesh segmentation of the computational domain

The fluid domain is segmented for meshing purposes. Segments 1, 2, 3 and 4 are mapped quadrilateral mesh segments. Segment 5 is an unmapped quadrilateral mesh segment. For each mapped segment, a number of divisions is specified for the opposing edges. The number of divisions for each edge pair is parametrised as an input parameter in the ANSYS Workbench environment. Segments 1, 3 and 4 are given biases that grow from the walls out and their bias factors (50 and 100 respectively) are constant across all configurations. Figure 3.3 shows a coarse mesh (relative to the final refined mesh in section 3.8) to visually represent the segmented mesh.

Segments 2, 3 and 4 are chosen as refined areas of the domain because of the jet's flow path and the gradients observed in velocity, pressure, and turbulence contour plots (see Figure 2.1). The dimensions of these sections

[3]The angle of 10° for the segment divider is selected based on the observed growth rate of typical free jet widths from literature and other simulations so as to avoid gradients across segments and to maintain orthogonality

Stellenbosch University https://scholar.sun.ac.za

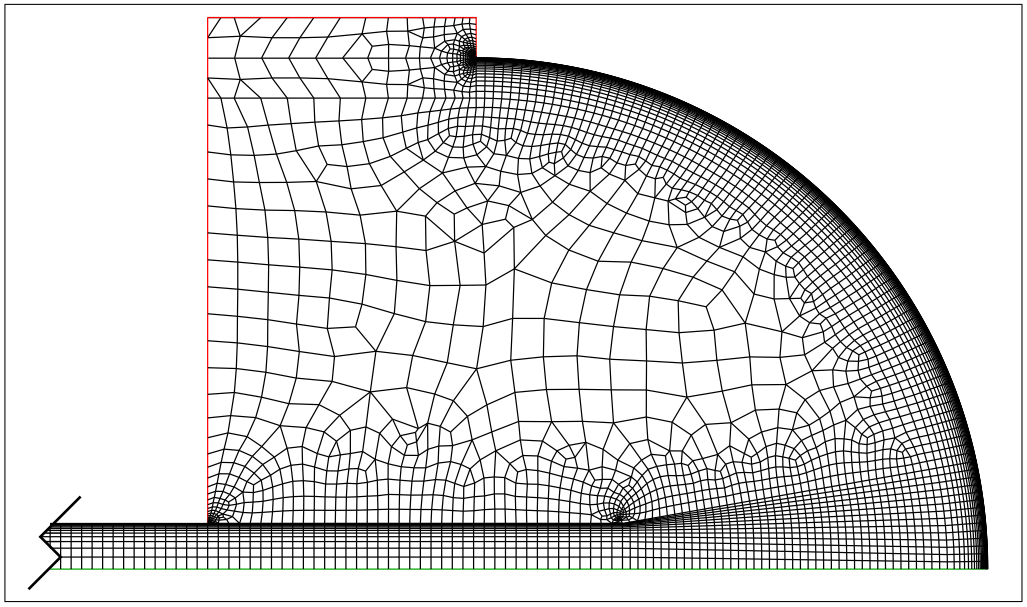

Figure 3.3: A coarse mesh of 5176 cells where $d = 34\,\text{mm}$ and $L/d = 4$

are determined in the iterative process according to the areas observed to have elevated gradients in early simulations. The 10° angle in segments 2 and 3 expands the refined area from the pipe exit to ensure that the turbulence and fluid entrainment at the jet's edge are captured. The cell growth from both walls is used to increase the cell count near the walls to capture the high gradients experienced in the boundary layers.

ANSYS offers the capability to generate all nine meshes according to the user-specified input parameters assigned to a single geometry and mesh generator. The number of divisions for each edge of different geometries were determined by iteratively obtaining the same maximum dimensionless first layer thickness, y^+_{max}, for the high Re cases across different pipe diameters (i.e. for different maximum near-wall flow velocities)[4]. Therefore, the objective of the input parameters for mesh generation is to generate all 15 meshes that meet the y^+_{max} criteria and to produce results that are independent of the mesh. The developed automated mesh generation system allows uniformity and consistency across all geometric configurations.

3.3 Boundary conditions

Figure 3.2 in section 3.2 also shows the type of boundary condition (BC) for each boundary. The fluid enters the domain via a velocity inlet BC and exits via a pressure outlet BC. The outlet domain is extended 200 mm out of the hemisphere with a 50 mm step in the radial direction to model the unconfined outflow region. A discussion on the model's sensitivity to the pipe exit flow

[4]The dimensionless first layer thickness, y^+ is based on the both the fluid behaviour and the thickness of the first wall mesh cell. It is used to quantify the first cell center in comparison to the boundary layer thickness

Stellenbosch University https://scholar.sun.ac.za

conditions is presented in section 4.3.1 and a discussion on the sensitivity to the position of the outlet BC is presented in section 4.3.3.

Lee *et al.* (1999) applied insulation behind the PLEXIGLAS® impingement surface to isolate heat transfer almost entirely from the gold film to the jet of air. It is assumed that there are negligible losses to the insulation and no heat loss is applied to the numerical environment. A uniform heat flux is, therefore, applied directly to the impingement surface boundary and no solid is included in the model.

The thermochromic liquid crystal layer has a small temperature range in which it displays colour gradients (Lee and Lee, 1999), therefore, the current that was applied to the gold film heat flux layer was tuned for each case depending on the heat transfer coefficient. Lee *et al.* (1997) published the electric gold film heater information showing a certain case where a $45.86\,\mathrm{W/m^2}$ heat flux is applied. At such low heat fluxes, the fluid temperatures, and hence fluid properties, are negligibly affected. The h and Nu show negligible sensitivity to flux alterations at low temperature, but when film temperatures get too high, the fluid properties start to affect heat transfer.

Since wall temperatures are kept near 35 °C (meaning negligible Nu sensitivity to heat flux), the heat flux of $45.86\,\mathrm{W/m^2}$ published by Lee *et al.* (1997) is applied to the wall for all cases simulated in the current validation study. This assumption is confirmed by a heat flux sensitivity analysis. The applied heat flux $\dot{q}''$ does not affect the Nu results, because at the observed temperature ranges, fluid property differences at different heat fluxes are assumed to be negligible.

Since the pipe flow Reynolds number, pipe diameter and the fluid properties are known, the mean inlet velocity, $\bar{V}$, can be calculated with equation 3.3. As discussed in section 4.3.2, velocity, turbulent kinetic energy, k, and specific dissipation rate, ω, profiles are specified at the velocity inlet boundary condition. The pipe entrance length, L_e, sensitivity is also shown in section 4.3.1.

$$\bar{V} = \frac{Re\ \mu}{\rho\ d} \tag{3.3}$$

3.4 Fluid properties

Ambient air enters the experimental setup and the jet temperature T_j is reported to be within 0.2 °C of ambient using a constant temperature bath Lee *et al.* (1997). Lee *et al.* (1999) do not report the temperature or air properties used, but 13 °C (or 286.15 K) is chosen because Lee *et al.* (1997), using the same test setup, report the jet temperature to be 13 °C. They would have had to adjust the heat flux at other ambient temperatures, but the dimensionless Nu results are not affected by ambient temperature for both experimental and numerical CFD work.

The properties of air at 1 atm, obtained from Mills and Ganesan (1999), are input as piecewise-linear air properties. Fluent™ interpolates the fluid

Stellenbosch University https://scholar.sun.ac.za

properties from the specified piecewise-linear input locally across the fluid domain. The interpolated jet inlet properties are shown in Table 3.2.

Table 3.2: Air properties at 286.15 K and 1 bar (Mills and Ganesan, 1999)

Description	Value	Unit
Density, ρ	1.234	kg/m^3
Dynamic viscosity, μ	1.786×10^{-5}	kg/(m s)
Specific heat capacity, c_p	1007.4	kJ/(kg K)
Thermal conductivity, k	25.87×10^{-3}	W/(m K)

3.5 Solution method and convergence

With different flow phenomena, certain solution methods are more stable and attain convergence faster than others. For optimal stability and performance, ANSYS (2016) suggests using the coupled velocity-pressure scheme for jet impingement flow in combination with the Green-Gauss cell-based scheme for gradient spatial discretisation, the standard scheme for pressure spatial discretisation and the second order upwind scheme for the remaining spacial discretisation parameters.

To determine the convergence to a solution, the scaled residuals for each equation are monitored. A scaled residual is determined by calculating the ration of the equation's residual at the current iteration and the largest residual observed in the first 5 iterations. The stopping criterion for the scaled residuals of all equations is specified as 1×10^{-6} with the exception of the energy equation which is set at 1×10^{-12} (Shuja *et al.*, 2003).

3.6 Automation, high-performance computing and solution analysis

The computational time for simulating a single configuration on an 8-core i7 personal computer (PC) is about 2 hours. Solving all 27 configurations, published by Lee *et al.* (1999), would take more than 2 days on the author's PC. To reduce this computational time, more CPUs are required that can run simulations in parallel. Stellenbosch University operates a high performance computer (HPC) that researchers can use. It has about 1272 CPUs and the architecture allows simulations to run in parallel. The HPC is utilised in this analysis to save time and to allow the author to perform multiple iterations of extensive parametric sets of simulation. It is seen in chapter 4 that the 27 configurations are run several times with different boundary conditions and model settings. To save time, significant computational resources and an automated system are required. Instead of taking over 2 days on a PC, 27 simulation can be completed within 2 hours on the HPC.

Fluent™ is installed on the HPC with more than 300 parallel licenses (1 parallel license per CPU) available to it. These licenses are shared by Fluent™ users on the HPC while all of the CPUs are shared by users for any software.

Stellenbosch University https://scholar.sun.ac.za

The HPC availability for Fluent™ simulations is dependent on the availability of the licenses and the CPUs. The HPC runs on Linux and is accessed remotely for job submission. There is no interaction with a job when it is running. A job is submitted as a set of commands and a solution is returned. See Appendix A.1 for an example of a job submission file.

Fluent™ can be entirely controlled via text commands through its text user interface (TUI). As an example of the necessity of the HPC, when the inlet boundary condition sensitivity is being analysed for all 27 cases, these 27 simulations are run for each of the 6 different inlet boundary conditions which results in 162 simulations.

To automate the generation of such a multitude of jobs for the HPC, the author has used MATLAB to generate the job submission file (Appendix A.1) and the Fluent™ journal TUI file (Appendix A.2). MATLAB allows the automation of the generation of the command files as well as the copying of the appropriate mesh, profile and user-defined function (UDF) files to the appropriate location. Not only is the file generation automated, but the HPC commands to read and run the files are also automated using MATLAB. This automation allows the author to generate the files, file structure and commands in a few minutes to run, for example, 162 simulations on the HPC. This saves notable time because the changes do not need to be made manually for each configuration individually.

The interaction with Fluent™ via the TUI also permits the author to generate dedicated output files for whatever output information is required. Such output files may include single value solution reports like area-weighted averages, facet maximums etc., or x-y plot information like Nu distribution on the impingement surface. This makes accessing, analysing, and plotting the solutions easier. The analysis and plotting of the output solution files is performed in the MATLAB environment.

3.7 RANS turbulence model selection

It has been found in the literature study that the k-ω SST turbulence model has proven to be the most accurate RANS model at predicting jet impingement flow characteristics and heat transfer[5]. The v^2f model is also considered by Behnia *et al.* (1998), Zuckerman and Lior (2006) as a good RANS model for jet impingement flow prediction, however, the v^2f model has been discontinued on Fluent™ commercial and academic licenses due to its apparent lack of relevance. The v^2f model can therefore not be a part of this analysis.

To confirm whether the k-ω SST model is the best RANS model for jet impingement on a concave hemispherical surface, a comparative study is done on 13 model configurations. The resulting Nusselt number distributions for all 13 models in the case of L4_d3_50 discussed in detail in section 4.1 with comments on the validity of each.

[5]The results shown in this chapter using the k-ω SST include the use of the production of k limitation and the intermittency transition model

Stellenbosch University https://scholar.sun.ac.za

3.8 Mesh independence

Since the model validation process is iterative (going back and forth with mesh independence, model selection and other numerical inputs), the following mesh independence study shows results of the k-ω SST with production limitation and the intermittency transition model active. Similar mesh independence is also achieved with the four equation Transition SST model with production limitation.

It is important to determine the model's sensitivity to mesh refinement. Mesh independence is defined here as a mesh that is refined to a point where more refinement alters the results negligibly. When a value of interest such as the maximum or area-weighted average Nusselt number converges to a stable solution with refinement of the mesh, then mesh independence is achieved (or the solution is independent of cell count).

Heyerichs and Pollard (1996) states that it is important to have a high level of refinement near a wall with jet impingement. They conclude that the first mesh layer from the impingement surface should be a non-dimensional distance from the wall of $y^+_{\max} \leq 1$ in order to capture the low Reynolds number effects. This is necessary for models that are not using wall functions, so that the boundary layer effects can be captured.

The mesh independence study presented here is performed on L4_d3_50 with an entry pipe length of $L_e = 20d$. The parametric method of generating the meshes for all geometries, as described in section 3.2, produces a mesh for L2_d1_50 with significantly smaller cells to capture gradients in the smaller boundary layer thickness (high velocity and small pipe) and hence resulting in similar $y^+_{\max}$ values at similar cell counts.

A mesh independence study is only conducted on L4_d3_50 and L2_d1_50 to observe the effectiveness of the parametric mesh generation. The below shown results are for the mesh independence study of L4_d3_50.

The maximum $y^+_{\max}$ on the hemisphere is monitored as the mesh is refined (see Figure 3.4). Mesh refinement to 35 000 cells or more results in $y^+_{\max} \leq 1$.

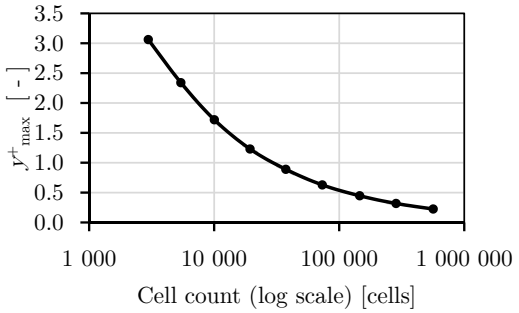

Figure 3.4: Convergence of $y^+_{\max}$ with increasing mesh cell count

The parametrised mesh variables are used to refine or coarsen the mesh. A starting mesh of 19 362 cells is used. Since the mesh is made up mostly of quadrilateral cells, the number of cells can roughly be doubled or halved by

Stellenbosch University https://scholar.sun.ac.za

respectively multiplying or dividing the number of edge divisions by $\sqrt{2}$. Cell count is halved sequentially to observe its sensitivity to coarsening. Cell count is doubled sequentially five times to obtain about 32 times the cell count of the staring mesh. Figure 3.5 shows the convergence of the maximum Nusselt number and the maximum pressure in the domain with increasing cell count. Figure 3.6 shows the convergence of Nu distribution along the dimensionless arc length r_a/d for some of the coarsened and refined meshes for L4_d3_50.

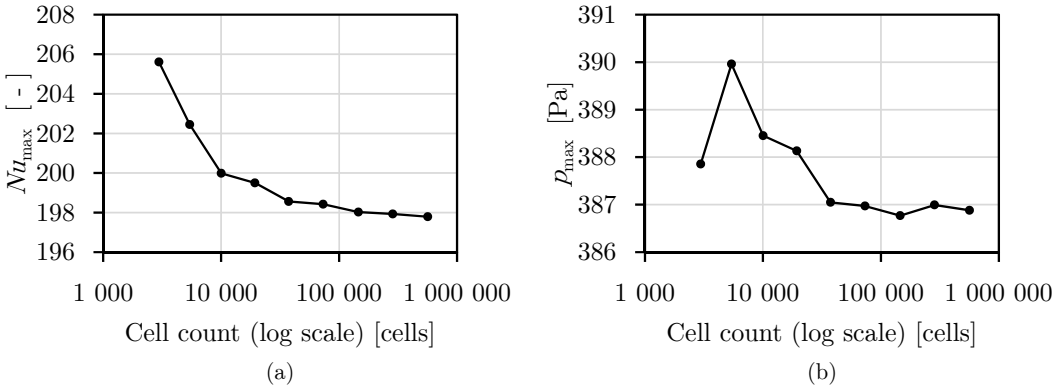

Figure 3.5: Convergence of two values of interest with increasing mesh cell count: (a) Maximum Nusselt number, (b) Maximum pressure in the domain

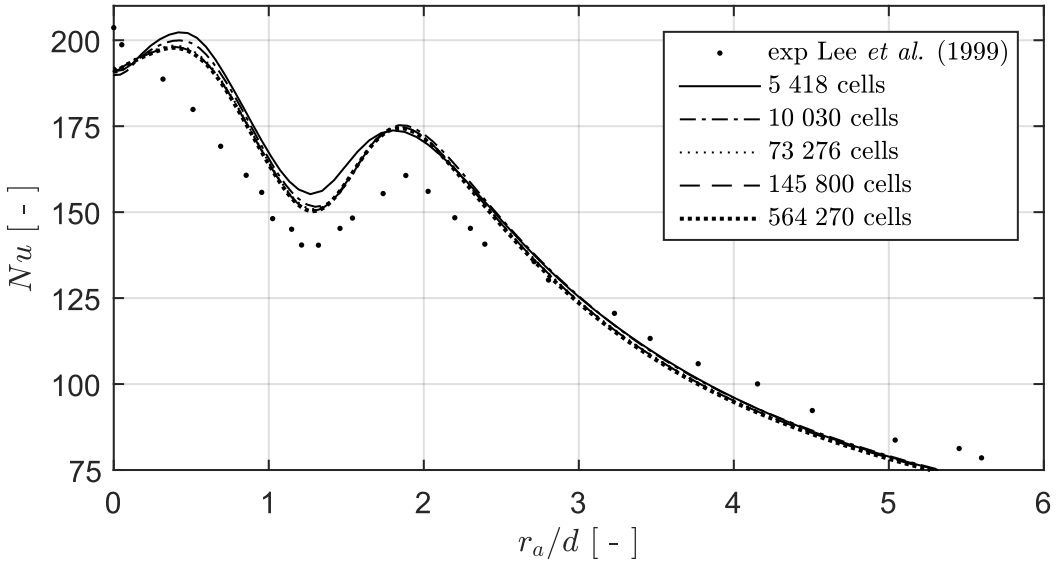

Figure 3.6: Nusselt number distributions for increasing cell count

The Nu_{max} and p_{max} start to stabilise with a mesh cell count of 37 434 at about 198 Pa and 387 Pa respectively. As a measure of redundancy, the mesh with 145 800 cells is selected as the mesh on which the other 14 meshes are based (i.e. the number of divisions are altered according to the geometric changes in order to maintain relative cell sizes and aspect ratios). This mesh refinement achieves the required $y^+_{max} \leq 1$ for all cases.

Stellenbosch University https://scholar.sun.ac.za

3.9 Conclusion

Developing a numerical model is always an iterative process with new model sensitivities and input alterations being discovered throughout the development process. This chapter has presented some of the processes involved in the development as well as the general numerical environment setup information.

The results and validity of the model are discussed in detail in chapter 4. It will be shown that the model is sensitive to some flow characteristics such as flow re-circulation, inlet velocity and turbulence profiles. For this reason, some of the above-mentioned numerical environment characteristics such as BC profiles and BC positions are changed where mentioned.

Stellenbosch University https://scholar.sun.ac.za

Chapter 4

Results and discussion of numerical model validation[1]

To determine the accuracy of the developed model, the results are compared to the experimental results of Lee *et al.* (1999). Their confidence level calculation resulted is 4.5 % maximum uncertainty for the Nusselt number.

This chapter presents how the results of the developed model correlate with the experimental results across all 27 cases to establish the validity of the model, and if there is poor correlation, to try to understand reasons for a poor match. Several sensitivity studies are conducted to quantify the impact of several assumptions.

4.1 Comparison of turbulence models

As mentioned in section 3.7, the results from 13 different turbulence models[2] and turbulence model option combinations are to be compared to the experimental results to determine which is the most valid model selection[3]. The 13 RANS turbulence model variations are listed and numbered below with the numbers subsequently being used for referencing:

1. k-ε standard with enhanced wall treatment (EWT)
2. k-ε standard with EWT with production of k limitation
3. k-ε standard with standard wall function
4. k-ω standard
5. k-ω SST with the low Re correction option
6. k-ω SST with production of k limitation
7. k-ω SST with production of k limitation and the intermittency transition model
8. k-ω SST with production of k limitation, intermittency transition model and the low Re correction option

[1] Parts of this chapter have been published in McDougall *et al.* (2018)

[2] The word "model" is henceforth used with reference to the RANS turbulence models as well as the CFD model as a whole

[3] Note that the results presented in this model selection process are obtained using an inlet length of $L_e = 58d$, as done by Lee *et al.* (1999), unless otherwise stated

Stellenbosch University https://scholar.sun.ac.za

9. Transition SST (4 equation) without production of k limitation
10. Transition SST (4 equation) with production of k limitation
11. Transition k-kl-ω (3 equation)
12. Reynolds-stress (5 equation) with EWT
13. Spalart-Allmaras

In Figure 4.1 and Figure 4.2, 11 of the 13 models are plotted because the k-ε standard with standard wall functions (3) and k-ω standard (4) models severely over-predict the Nusselt number throughout the arc-length, but particularly around the stagnation point, with $Nu_0 \approx 300$ and $Nu_0 \approx 400$ respectively. For this reason, these two models have been omitted from the plots.

The 2-equation models such as the k-ω and k-ε models typically generate excessive amounts of turbulent energy, particularly in stagnation regions (Menter, 1993). For this reason, Menter (1993) developed a method of limiting the production of turbulent energy in such regions. This is what is meant by the above-mentioned model option of "with production of k limitation".

The success of this production limiter is evident by the excessive Nu in the stagnation region for models (3) and (4), which is caused by the excessive kinetic energy production that is not limited.

Figure 4.1 plots the Nu distributions for 8 of the remaining 11 models. These 8 results show poor correlation with the experimental results, which narrows the model selection down to the three models presented in 4.2.

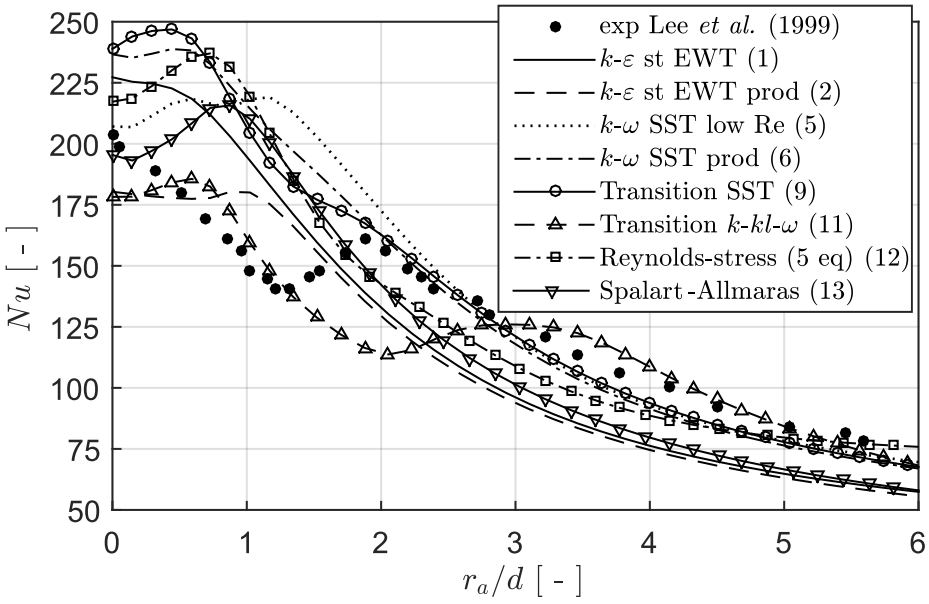

Figure 4.1: Nusselt number distributions for the less accurate numerical models on L4_d3_50

Taking a closer look at the poorly correlated models, it is seen that the Transition SST model without production limitation (9) over-predicts the stagnation region while having adequate correlation in the wall jet region. The same comment applies to models (5) and (6), with model (5) showing

Stellenbosch University https://scholar.sun.ac.za

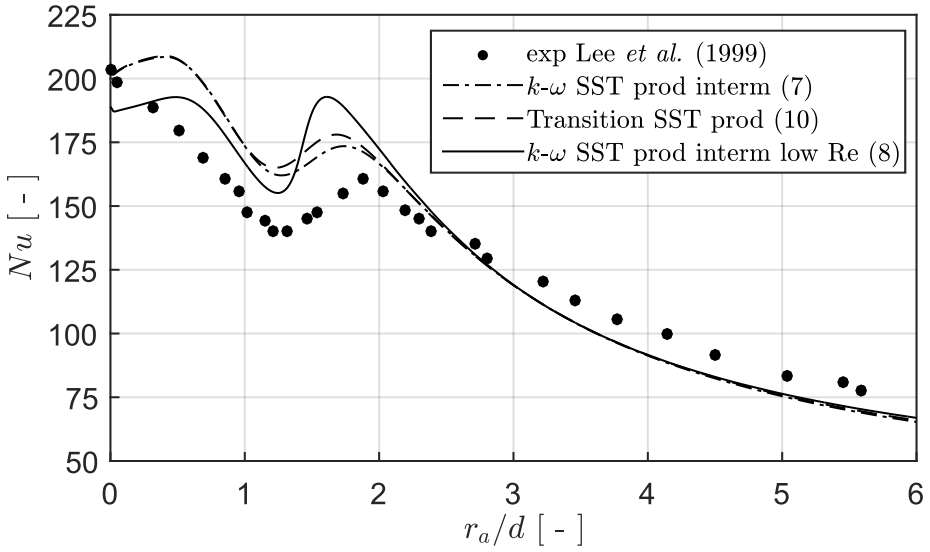

Figure 4.2: Nusselt number distributions for the more accurate numerical models on L4_d3_50

a slight secondary peak phenomenon. Models (1), (2), (12) and (13) under-predict the jet wall region without adequate stagnation region correlation. The stagnation region as well as the shape of the distribution from model (11) appears promising with the second peak being modelled, but the correlation with Lee *et al.* (1999) is poor.

Analysing the remaining three models shown in Figure 4.2, it is evident that models (7) and (10) produce similar results while model (8) shows better correlation in the stagnation region and worse correlation around the secondary peak region. Models (7) and (10) prove to be highly sensitive to the turbulence and velocity profiles at the pipe exit (i.e. fully-developed pipe flow conditions). This sensitivity to pipe exit flow conditions is discussed in detail in section 4.3.2 and may be the cause for the over-prediction in the stagnation region of these two models.

Section 4.2 presents information about the theory of the three best correlating models discussed and the invalidity of model (8) is reasoned.

Of the remaining two models, the k-ω SST model shows the best agreement with the experimental data, performing slightly better than the Transition SST model between the local minimum and local maximum of the secondary peak. The k-ω SST model is preliminarily the model of choice for this analysis, but since the results are so similar, further investigation is deemed necessary. Refer to section 4.4 for this further investigation as well as Appendix B for the results of an additional flat plate validation study.

Stellenbosch University https://scholar.sun.ac.za

4.2 Review of the k-ω SST and Transition SST turbulence models

The literature review of jet impingement in chapter 2 suggests that the k-ω SST model is seemingly the preferred model for jet impingement. It is also apparent that the Transition SST and k-ω SST with the intermittency transition extension active are the models that produce the best results for the current problem. To obtain a better understanding as to why these models are producing acceptable results for jet impingement, a more in-depth review on the models is conducted.

4.2.1 Development of the k-ω SST turbulence model

Menter (1992) developed two improvements to the k-ω RANS model, both of which are based on the k-ε (transformed into the k-ω formulation) with the inclusion of the original k-ω model for resolving near wall (boundary layer) flow. The two models are known as zonal models, which means the models can distinguish between zones such as the near wall zone and free stream flow.

The Baseline (BSL) model uses the original k-ω model with the set of constants by Wilcox (1988) in the near wall zone, and the transformed k-ε model with constants by Jones and Launder (1973) in the free stream zone. The sets of constants are further referred to as ϕ_1 and ϕ_2.

To switch between the two models, a switching/blending function is used to calculate where each model should be active (near wall or free stream) or a blending of the two. The switching/blending function is described in equation 4.1 where $F_1 = 1$ in the near wall zone and $F_1 = 0$ in the free stream zone or in the blending region $0 < F_1 < 1$ (Menter, 1992).

$$\phi = F_1\phi_1 + (1 - F_1)\phi_2 \tag{4.1}$$

where

$$F_1 = \tan h(\arg_1^4) \tag{4.2}$$

with

$$\arg_1 = \max\left(\min\left(\frac{\sqrt{k}}{0.09\ \omega\ y}; 0.45\frac{\omega}{\Omega}\right); \frac{400\nu_t}{y^2\ \omega}\right) \tag{4.3}$$

The blending argument is based on the ratio of the turbulent length scale and the distance to the next surface ($\sqrt{k}/(0.09\omega\ y)$) which is equal to 2.5 in the logarithmic layer of the boundary layer and reduced to zero at the edge of the boundary layer. The BSL model therefore uses the original k-ω model in the logarithmic part of the boundary layer and blends into the transformed k-ε model towards the start of the free stream region or the edge of the boundary layer (Menter, 1992).

This BSL model, however, is using ϕ_1 from the original k-ω model as its set of constants. Menter (1992) also proposed and developed the SST model which is formulated in exactly the same way as the BSL model discussed above, but

Stellenbosch University https://scholar.sun.ac.za

the set of constants ϕ_2 is different, and the eddy-viscosity, ν_t, is formulated differently, with slight differences in the blending function arguments (Menter, 1992).

Before the SST model was developed, flow fields with adverse pressure gradients and laminar-transitional-turbulent boundary layer formation were difficult to model due to the complex boundary layer characteristics. For such flow fields, the k-ε turbulence model does not capture the boundary layer conditions accurately (particularly near the wall) because wall functions are not calibrated for adverse pressure gradients or laminar-transitional-turbulent boundary layer formation (Menter, 1992).

The importance of modelling boundary layer information accurately is prominently apparent in the field of aerodynamics where the interaction between the viscous and inviscid flow is required. It is necessary because the viscous-inviscid interaction significantly affects the free stream and far-field pressure distribution, which has an effect on the performance of, for example, an airfoil (Menter, 1992).

The SST model proves to be useful for modelling flow fields with adverse pressure gradients, by accurately determining the position of flow separation or re-attachment, such as airfoil and backward-facing step flow fields (Menter, 1992).

The applicability of this to jet impingement is that when the jet impinges, the fluid dissipates and flows radially outwards as a flat plate boundary layer problem with an increasingly adverse pressure gradient would. The flow slows down due to the pressure gradient without necessarily separating as the kinetic energy is dissipated. This flat plate boundary layer development flow field is described in detail by Samuel and Joubert (1974), and Menter (1992) confirms that his SST model simulates this type of flow well.

The regular k-ω SST model does not, however, perform well with laminar or transitional boundary layers. This is where the Transition SST or the activation of the intermittency transition model becomes useful.

4.2.2 Relevance of the Transition SST turbulence model and the intermittency transition extension

The stagnation point is the impact point where flow velocity is zero. The formation of the boundary layer from the stagnation point is therefore laminar flow. Flow velocities increase in the radial direction and the boundary layer goes through a transition from laminar flow to turbulent flow. This is accentuated by the acceleration of the entrainment region fluid as it is forced out radially by the pressure caused by stagnation.

The 4-equation Transition SST model offers two additional transport equations on top of the k-ω SST. These two equations essentially resolve the intermittency γ ($\gamma = 0$ if laminar flow and $\gamma = 1$ if turbulent flow and $0 < \gamma < 1$ if transitional flow) and the transition onset criterion.

Stellenbosch University https://scholar.sun.ac.za

Menter *et al.* (2004) describes the formulation of the Transition SST model available in Fluent™. They use empirical correlations to formulate the constants and functions. Multiple blending functions are implemented where relevant in this zonal model.

Fluent (2016) explain in their theory guide that they offer an option to activate the intermittency transition model, which is a newer version of the Transition SST model that combines the two additional equations into one. The reduction of the number of equations is assumed to reduce computational expense.

The theory guide recommends that the low Reynolds number correction option is not used because the empirical correlations that govern the use of the additional option are not calibrated for a wide range of flow conditions (Fluent, 2016). For this reason, the use of the low Reynolds correction extension is eliminated from the final model selection. The results are in any case, not as good as the transition models.

It is evident in section 4.1 that, apart from producing the best correlation with the experimental results, the two aforementioned transition models produce similar results with slight discrepancies only in the region between the local minimum and the local maximum of the secondary peak. Although the reduced computational expense of the k-ω SST intermittency model is desirable, the two models are further compared in subsequent sections where it is shown that there is a negligible difference.

In summary, the blending functions that are designed to capture the laminar boundary layer in the stagnation region, together with the transition correlations and SST adverse pressure gradient formulation of both the Transition SST and k-ω SST intermittency models, make these two models appear to be well suited for the simulation of jet impingement.

4.3 Model sensitivities

It is important to study what a model is sensitive to in terms of the setting up of the numerical environment. A model may be sensitive to the grid refinement, in which case further investigation into mesh independence would be required. In the extensive model development process, some sensitivities were noted which are discussed in this section.

4.3.1 Position of inlet boundary condition

Lee *et al.* (1999) use a pipe of length 58 times the pipe diameter ($L_e = 58d$) in order to achieve fully developed flow. The effect of the pipe exit conditions on the results is shown in section 4.3.2 to be significant. It is common practice to model the pipe flow separately and to use the separately-modelled fully developed flow profiles (velocity and turbulence) as the inlet boundary condition for the rest of the flow field.

A sensitivity observation is performed for the inlet boundary condition position. Using a fully developed profile as the BC, two meshes are generated.

Stellenbosch University https://scholar.sun.ac.za

One has 10 diameters of pipe being modelled ($L_e = 10d$) and the other has no pipe being modelled, with the BC specified at the pipe exit ($L_e = 0$). This comparison is done using the k-ω SST model with production of k limitation with the intermittency transition model enabled.

It is observed that the Nu distribution results of the two inlet lengths are almost identical, with negligible sensitivity to the inlet length or position of the inlet BC. Closer observation shows that, when the small section of pipe is included in the model, the flow conditions in the pipe are only slightly affected in the final 0.01 diameters of the pipe, which is considered to be negligible.

The pressure drop from pipe exit to the pressure outlet BC is relatively small. The negligible back-pressure means a negligible effect on the pipe flow. Because of the insensitivity to L_e, it is concluded that specifying the inlet BC flow profiles at the pipe exit (i.e. $L_e = 0$) is sufficient.

4.3.2 Fully developed pipe flow

(Lee *et al.*, 1997) performed jet impingement experiments on a convex hemisphere with the same experimental apparatus as Lee *et al.* (1999). (Lee *et al.*, 1997) published additional information about the experimental setup such as the velocity profile at the jet pipe exit. Comparisons are shown for the pipe exit velocity profiles in Figure 4.3.

The author observed a significant sensitivity to the fully developed pipe flow conditions specified at the pipe exit. Pipe flow being modelled separately allows the author to observe the pipe flow conditions at different lengths. The three pipe diameters are modelled with $L_e = 100d$ and flow profiles (velocity V, turbulent kinetic energy k, intermittency γ and specific dissipation rate ω) are exported at $L_e = \{5d; 7.5d; 10d; 12.5d; 15d; 20d; 30d; 40d; 58d\}$ for use as inlet conditions to the rest of the flow domain.

If the modelled pipe's inlet turbulent intensity is set to be 5 %, the pipe flow becomes fully developed somewhere between $L_e = 40d$ and $L_e = 58d$ where the centreline velocity and turbulence stabilise. Turbulent intensity is said to be about 4 % for $Re = 50\,000$ and 5 % for $Re = 11\,000$, according to the correlation, $I = 0.16Re^{-1/8}$, published by Fluent (2016). If 1 % turbulent intensity is stipulated at the pipe inlet, the flow is not fully developed in $L_e = 100d$. The pipe's inlet conditions, therefore, significantly affect the development length, and hence pipe exit flow conditions.

All three pipe diameters for each of the three Re are modelled and flow condition profiles exported at the aforementioned development lengths. This set of pipe flow profiles is used as inlet BCs in the jet impingement environment to determine the model's sensitivity to fully developed flow. To validate the modelled fully developed smooth pipe flow profiles, a modelled pipe flow at $Re = 42\,000$ is compared to two sets of experimental results, Lee *et al.* (1997) and Laufer (1954), as well as the 7th power (Schobeiri, 2010) and the logarithmic overlap law (White, 2009)[4].

[4]Note that the 7th power law, logarithmic overlap layer and modelled profiles are based on the same $Re = 42000$ just as the experimental results were produces

Stellenbosch University https://scholar.sun.ac.za

This comparison is shown in Figure 4.3 where the dimensionless radius is portrayed logarithmically and linearly. The linear distribution indicates that the centreline velocities, $U_{\max}$, correlate well. It is also noticeable that the modelled and logarithmic overlap layer results are higher in the overlap layer. The near wall region is noticeably different where the k-ω SST model appears to be modelling the inner layer of the boundary layer, as White (2009) shows it should be expected. Good overall velocity profile correlation is achieved.

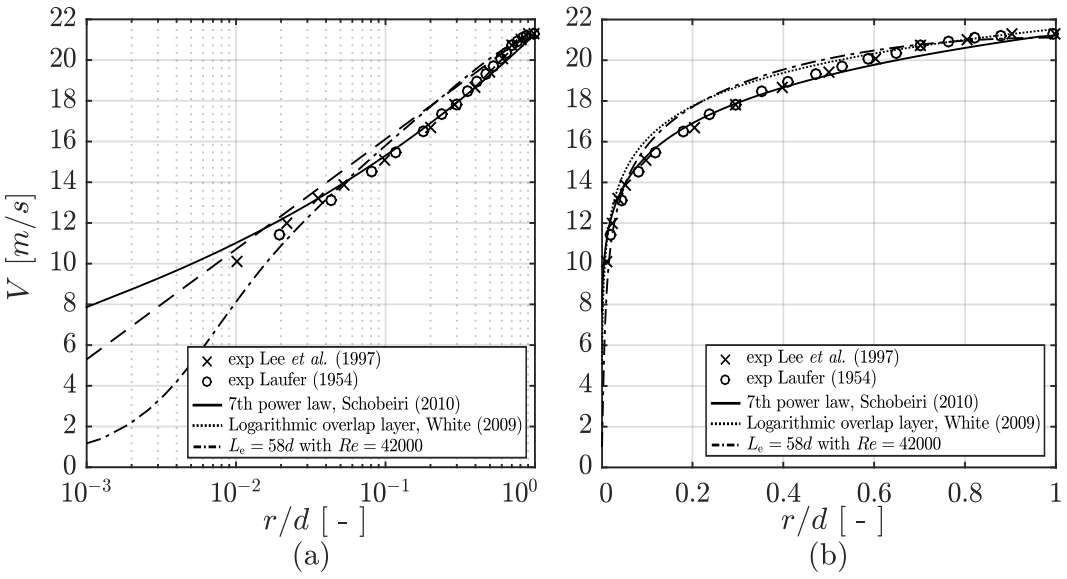

Figure 4.3: Fully developed pipe flow velocity profiles along the (a) logarithmic dimensionless radius and (b) linear dimensionless radius

The turbulence information at the experimental pipe exit is, however, unavailable. Figure 4.4 shows the model's sensitivity to the development length and hence pipe exit turbulence. The infinite development length, $L_e = \infty$, is achieved by modelling a section of pipe with a periodic boundary condition, so as to solve fully developed flow, which results in almost exactly the same Nu distribution as $L_e = 58d$. The turbulence model employed here is model (7) as described in section 4.1.

Note that, although Figure 4.4 shows significant sensitivity to pipe exit conditions, the different pipe exit profiles are still presenting the same mass flow into the domain, and the wall jet region is seen to not be at all sensitive to the inlet conditions. It is only the stagnation and secondary peak regions that are affected.

The flow conditions entering the pipe in the experimental setup (depicted in Figure 3.1 to have a smooth transition nozzle) are not published, and limited information is available regarding the experimental pipe exit conditions. This presents some uncertainty in the accuracy of the replication of experimental conditions. Since the pipe exit turbulence exhibits a significant effect on the stagnation region and this information is not published, the validity of the condition replication is somewhat uncertain.

Stellenbosch University https://scholar.sun.ac.za

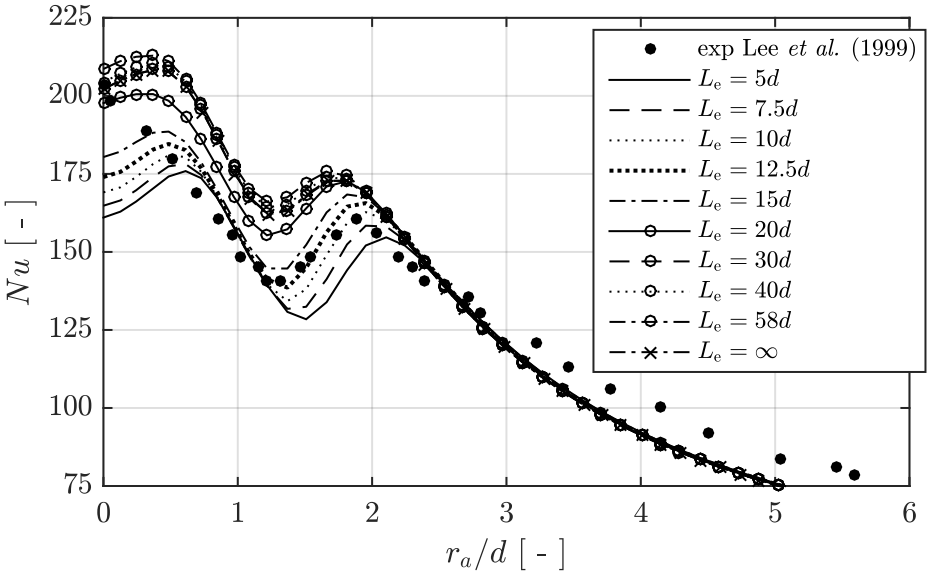

Figure 4.4: Nu distributions resulting from varying pipe flow development lengths L_e for L4_d3_50

4.3.3 Outlet boundary condition

Lee *et al.* (1999) published 27 Nu distributions. The current validation study is done to develop a CFD model that is valid across all 27 different flow fields. During the development process, the author noticed that with a decrease in diameter ratios, a decrease in experimental correlation occurred. The development process started with modelling only the large pipe diameters, where good correlation was being achieved. When the smaller pipe diameter was modelled, the results did not feature a second peak.

The model captures the stagnation region heat transfer well, but seems not to capture the flow acceleration causing the secondary peak, and the wall jet heat transfer is subsequently significantly under-predicted.

Since the geometric setup of the experiments is non-dimensionalised, a change in pipe diameter (with the same Re and dimensionless pipe-to-surface distance, L/d) simply changes the relative impingement surface curvature intensity, d/D. The experimental results show that the Nu distribution is not significantly affected by curvature intensity (or pipe diameter ratios), but the simulation results are poor for the small $d/D = 0.034$.

It was later discovered that the reason for the secondary peak not appearing and wall jet heat transfer being under-predicted is that near the edge of the hemisphere, the heated flow is separating from the wall and recirculating in a large vortex. This causes the mixing of heated air in the entrainment region of the developing jet. The mixed-temperature air (made up of the warm, re-circulated air and the cool jet air) is the the air that accelerates in the wall jet region, but with re-circulation, the high temperature air causes a drastic reduction in heat transfer and affects the downstream wall jet region.

Stellenbosch University https://scholar.sun.ac.za

The model sensitivity is confirmed by moving the outlet boundary condition into the dome region, essentially reducing the size of the flow domain, to force the heated fluid to exit the domain and allow back-flow fluid, coming from the outlet BC at a user-specified temperature, to enter the flow domain. Geometrically, with the axisymmetric assumption, this results in a cone-like shaped domain (see Figure 4.5). The back-flow fluid temperature (for both domains) is specified at the same temperature as the pipe exit temperature. Note that the temperature scales and velocity scales for both domain types in Figure 4.5 are identical.

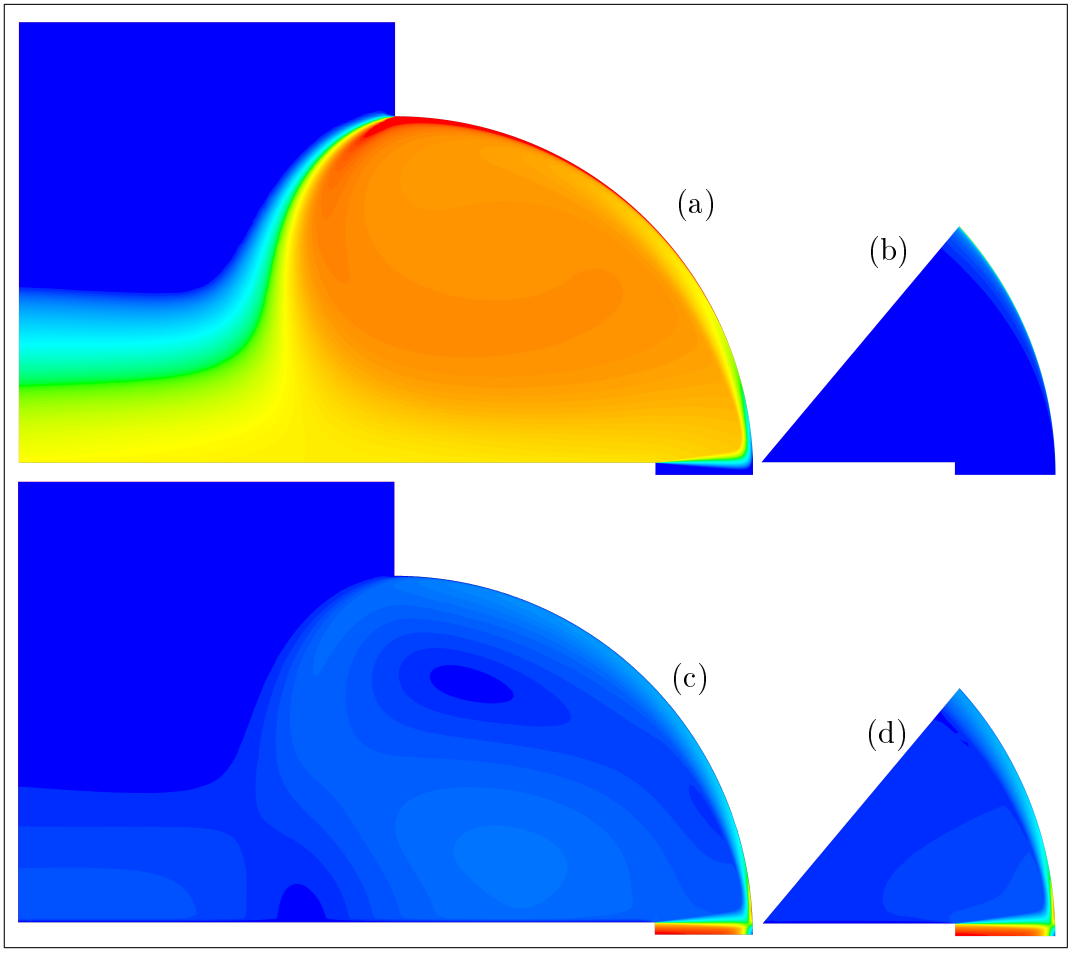

Figure 4.5: Contour maps for L4_d1_50 of (a) Temperature (large outlet), (b) Temperature (small outlet), (c) Velocity magnitude (large outlet) and (d) Velocity magnitude (small outlet)

Analysing Figure 4.5, it is observed that the velocity magnitudes in the different domains are very similar (it is also noted that the skin friction coefficients, C_f, are almost identical). What is significant about these contour plots is that, due to re-circulation of the heated fluid, the temperature of the air in the entrainment region is that of mixed hot and cold air, which significantly reduces jet impingement heat transfer. Figure 4.6 illustrates the effect on heat

Stellenbosch University https://scholar.sun.ac.za

transfer using both outlet BCs described above (re-circulation and "cone") and comparing the large $d/D = 0.089$ with the small $d/D = 0.034$.

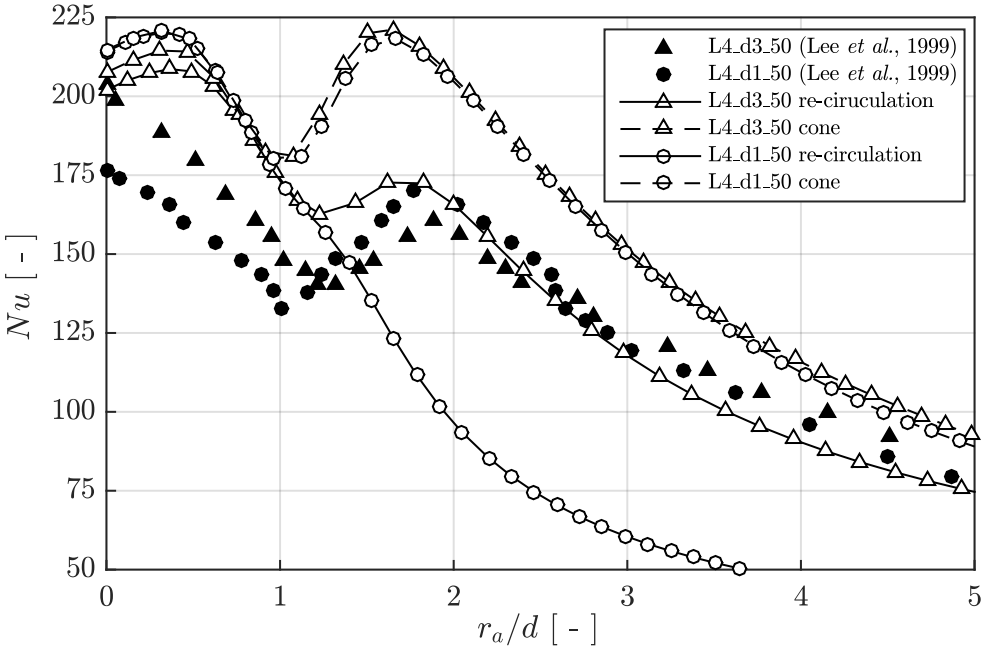

Figure 4.6: Nusselt number distributions for two different diameter ratios

The "cone" domain causes the entrainment of cool air at the same temperature as the jet (instead of hot re-circulated air) which allows the second peak of heat transfer to be present, and the wall jet heat transfer is noticeably higher. The difference between the Nu distributions is particularly noticeable for smaller diameters such as $d/D = 0.034$.

The backward step that makes the outlet domain larger is an attempt at modelling a more realistic representation of the experimental setup. The results, however show a significant re-circulation occurring, which may not be seen in experiments. The small outlet domain that is cone-like is undoubtedly unrealistic. The larger diameter $d/D = 0.089$ does not result in as much re-circulation as $d/D = 0.034$, which means that the re-circulated air is at a lower temperature and a secondary peak is therefore observed.

Figure 4.6 shows the effect of re-circulation. The results from the large domain show evidence of re-circulation which increases the temperature of the jet entrainment region, causing a reduction in heat transfer where the secondary peak is expected. The lower heat transfer translates into the wall jet region and significantly reduces the average heat transfer capability of the mechanism.

The cone-like domain causes an over-prediction of the secondary peak which again translates to the wall jet region, causing a significant over-prediction of the average heat transfer capability. The re-circulation in L4_d3_50 is somewhat less due to the larger diameter ratio $d/D = 0.089$. The prediction

Stellenbosch University https://scholar.sun.ac.za

of the secondary peak is seen to be in between the extremes observed in $d/D = 0.034$.

It is therefore concluded that the model's sensitivity to the outlet region, where re-circulation and back-flow occurs, is significant. The inaccuracies in the prediction of re-circulation are assumed to be caused by one or both of the following:

1. The outlet boundary condition is too small and does not resolve the flow surrounding the experimental apparatus. It would be difficult to replicate this environment since the relevant geometric information is not published.
2. The separation point from the wall near the edge of the dome may be inaccurate and there may not even be separation. This is likely to be influenced by the physical environment of the outlet region of the experimental setup, which would alter the outlet flow characteristics.

The use of the cone-like domain is, of course, unrepresentative of the experiments, but it displays the sensitivity of the heat transfer mechanism to the re-circulation of heated fluid. The discovery that re-circulation affects heat transfer so significantly is an important consideration when applying jet impingement to something like the SCRAP receiver's spike tip.

4.4 Numerical correlation with experiments

The author has used the developed automation system together with the HPC (see section 3.6) to run several thousand simulations. Given the above-mentioned sensitivities, the parametric set of 27 published cases has been simulated with the large outlet domain (with k-ω SST intermittency and Transition SST models) and the cone-like domain using six different inlet lengths ($L_e = \{5d; 10d; 12.5d; 15d; 58d; \infty d\}$), totalling 486 simulations. This allows for a full quantification of the experimental correlation for the different models and inputs.

Figure 4.7, Figure 4.8 and Figure 4.9 show all 27 experimental cases with the results of the cone-like and large outlet domains for an inlet length of $L_e = 58d$ using the k-ω SST intermittency model.

The trend of over-predicting the wall jet region with the cone-like domain and under-predicting it with the large domain is almost unanimous. This over- and under-prediction, particularly the under-prediction, increases with decreasing dimensionless pipe diameter d/D. The small pipe diameter flow displays excessive re-circulation, which is assumed to be due to: the larger space left for large eddy formation, the increased level of separation from the hemispherical surface, or a combination of the two. The elevated re-circulation of heated fluid results in less heat transfer in the secondary peak and wall jet regions because of the smaller temperature difference between the fluid and wall at the interface.

Stellenbosch University https://scholar.sun.ac.za

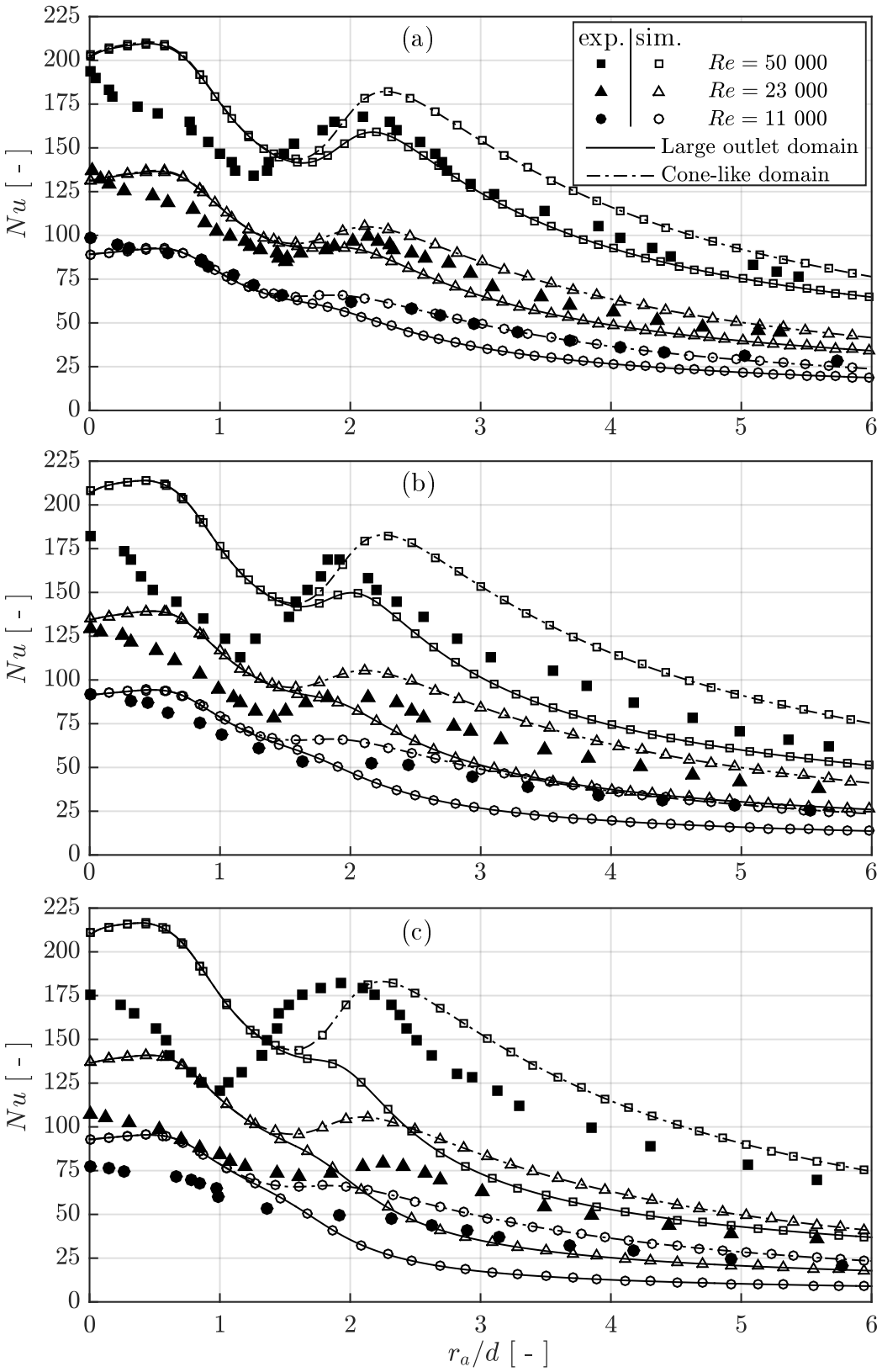

Figure 4.7: Nusselt number distributions at $L/d = 2$ for exp. (experimental) and sim. (simulation) results in both numerical domain types using the k-ω SST intermittency model where (a) shows $d/D = 0.089$, (b) shows $d/D = 0.056$, and (c) shows $d/D = 0.034$

Stellenbosch University https://scholar.sun.ac.za

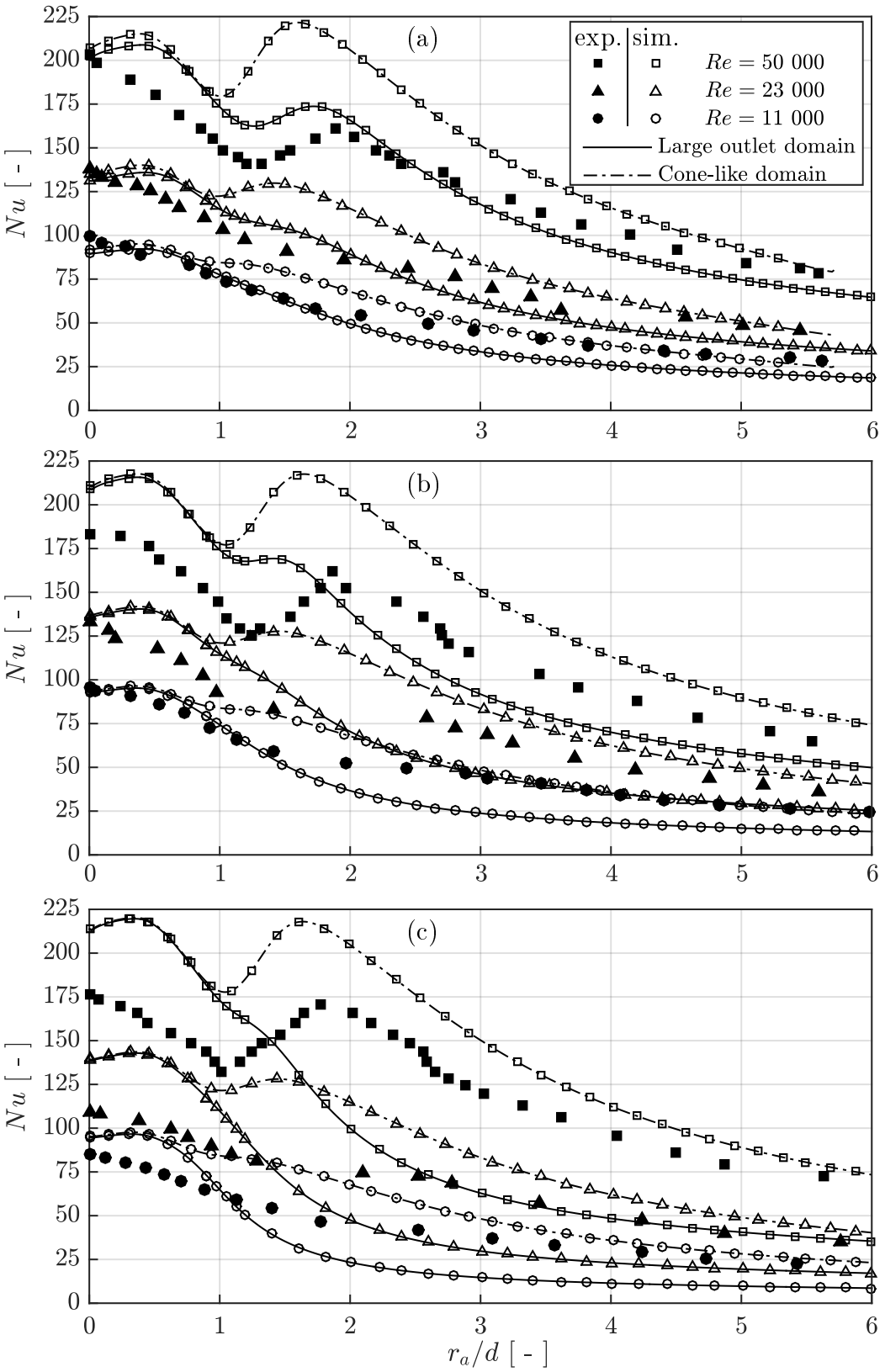

Figure 4.8: Nusselt number distributions at $L/d = 4$ for exp. (experimental) and sim. (simulation) results in both numerical domain types using the k-ω SST intermittency model where (a) shows $d/D = 0.089$, (b) shows $d/D = 0.056$, and (c) shows $d/D = 0.034$

Stellenbosch University https://scholar.sun.ac.za

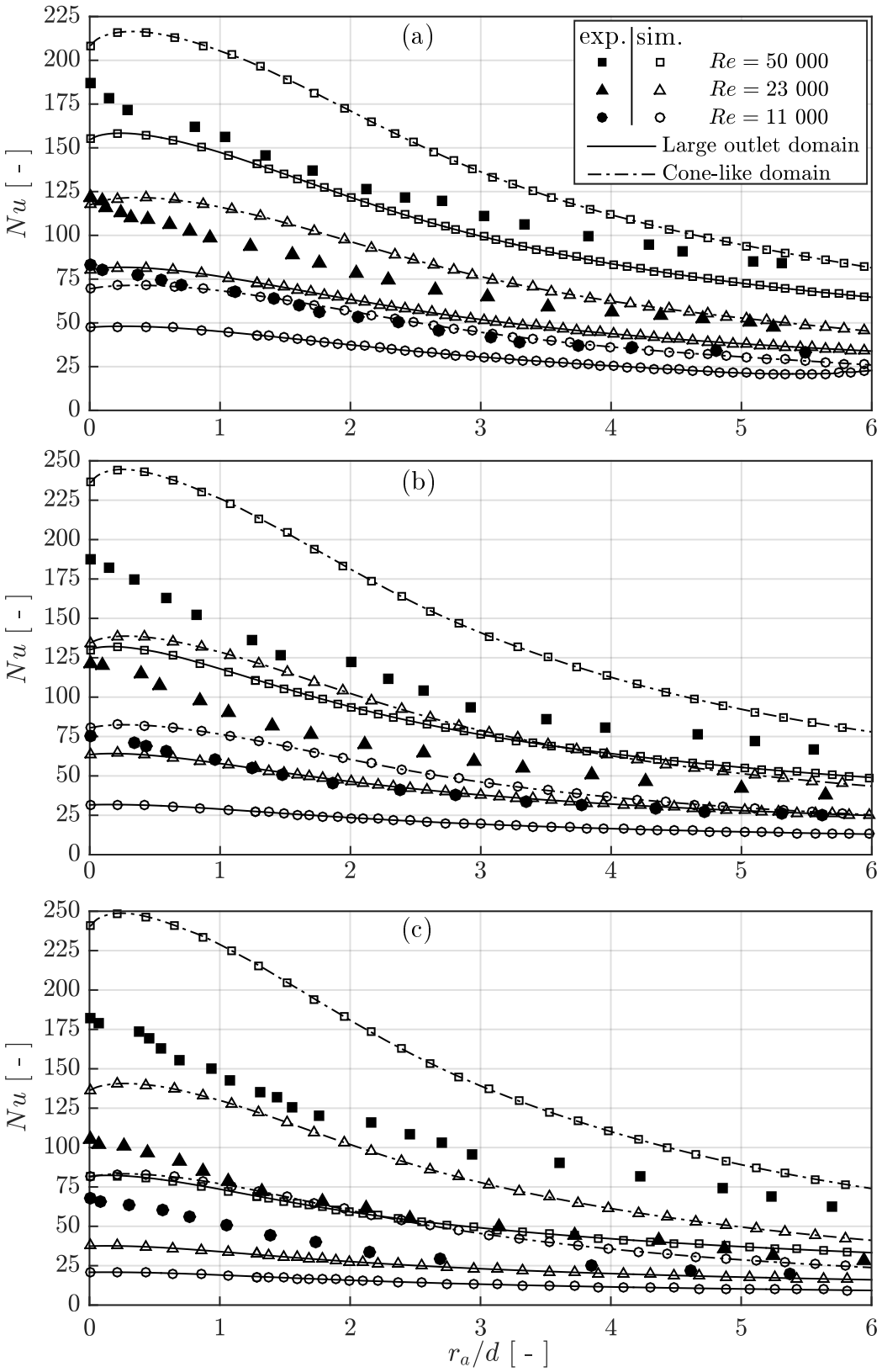

Figure 4.9: Nusselt number distributions at $L/d = 10$ for exp. (experimental) and sim. (simulation) results in both numerical domain types using the k-ω SST intermittency model where (a) shows $d/D = 0.089$, (b) shows $d/D = 0.056$, and (c) shows $d/D = 0.034$

Stellenbosch University https://scholar.sun.ac.za

Both domains, with the exception[5] of $L/d = 10$, produce almost identical results in the stagnation region, after which the results split at the local minimum where the entrainment region fluid reaches the surface. There is not much information about the geometric and flow characteristics in the outlet region of the experimental setup. The amount of re-circulation and the surrounding geometries are therefore unknown. Knowing this information would help the author to better replicate the flow domain numerically. This may have resulted in an improved prediction of the re-circulation, and better correlation with the experimental results.

Area-weighted average (further referred to as average) Nu_{avg} is weighted more with increasing arc-length, r, from the stagnation point. For example, the Nu in the wall jet region weighs significantly more for Nu_{avg} than in the stagnation region because of the increasing circumference. A distribution with an over-predicted stagnation region and an under-predicted wall jet region will likely result in an under-predicted Nu_{avg}.

Nu_{avg} is calculated using equation 4.4 where $r_{\max}$ is the maximum arc-length of the published data by Lee *et al.* (1999). The local Nu is evaluated using the midpoint rule and the discretised area A is evaluated as a slice of the hemisphere using the arc-length as the width. To make the experimental and simulation Nu_{avg} comparable, they are evaluated from the stagnation point until the same arc-length $r_{\max}$ limited by the published data.

$$Nu_{\text{avg}} = \frac{\sum_0^{r_{\max}} Nu\ A}{\sum_0^{r_{\max}} A} \tag{4.4}$$

Table 4.1 shows the correlation percentage $\left(\frac{Nu_{\text{avg,sim}} - Nu_{\text{avg,exp}}}{Nu_{\text{avg,exp}}}\right)$ of the Nu_{avg} results. An over-prediction of the experimental results is shown by a positive correlation percentage, and a negative correlation percentage shows an under-prediction. The table presents results of 3 different models, namely: the cone-like domain using k-ω SST with intermittency transition blending, the large outlet domain using k-ω SST with intermittency transition blending, and the large outlet domain using the Transition SST model.

The average of the absolute value of the correlation percentages across all of the above mentioned 486 simulations is 25.45 %. Observing the results from $L_{\text{e}} = 58d$ in Table 4.1, it is seen that the Transition SST model has better experimental correlation than than the k-ω SST intermittency transition model. The difference is merely 1 % between the average percentages of -27.60 % and -28.60 % respectively.

The k-ω SST intermittency transition model is concluded to be the model of choice between the two similar models because of its reduced computation expense facilitated by the combining of the two additional equations into one. The author has also found the model to be more stable than the Transition SST model.

[5] The position of the outlet BC in the cone-like domain affects the jet's flow characteristics for $L/d = 10$ significantly, whereas these effects are negligible with $L/d = 2$ and $L/d = 4$

Stellenbosch University https://scholar.sun.ac.za

Table 4.1: Table of percentage differences between simulation and experimental Nu_{avg} for three different models with $L_e = 58d$ and where d1 is $d/D = 0.034$, d2 is $d/D = 0.056$, and d3 is $d/D = 0.089$

Model	Cone-like, k-ω SST int.			Large outlet, k-ω SST int.			Large outlet, Transition		
				$L/d = 2$					
Re	d1	d2	d3	d1	d2	d3	d1	d2	d3
50 000	15.3 %	24.3 %	13.2 %	−34.2 %	−9.5 %	−4.0 %	−33.4 %	−8.8 %	−3.3 %
23 000	31.6 %	19.1 %	11.3 %	−30.7 %	−18.1 %	−7.9 %	−30.7 %	−17.2 %	−7.3 %
11 000	23.2 %	10.4 %	−1.8 %	−41.2 %	−29.1 %	−21.9 %	−41.8 %	−29.1 %	−21.8 %
				$L/d = 4$					
Re	d1	d2	d3	d1	d2	d3	d1	d2	d3
50 000	20.0 %	28.6 %	19.5 %	−41.9 %	−13.8 %	−4.2 %	−39.4 %	−13.2 %	−3.7 %
23 000	30.9 %	25.5 %	17.3 %	−42.0 %	−21.8 %	−9.1 %	−40.6 %	−20.7 %	−8.5 %
11 000	27.9 %	10.6 %	6.2 %	−50.0 %	−37.0 %	−21.4 %	−50.5 %	−37.1 %	−21.5 %
				$L/d = 10$					
Re	d1	d2	d3	d1	d2	d3	d1	d2	d3
50 000	37.4 %	42.0 %	20.1 %	−49.4 %	−21.2 %	−11.5 %	−48.4 %	−20.6 %	−11.5 %
23 000	50.7 %	31.0 %	13.9 %	−54.1 %	−35.1 %	−22.0 %	−52.0 %	−33.6 %	−21.7 %
11 000	51.2 %	23.2 %	−0.7 %	−52.9 %	−47.3 %	−32.1 %	−48.2 %	−42.6 %	−22.2 %

The cone-like model correlation percentages show an almost unanimous over-prediction while the large outlet model shows unanimous under-prediction. This is assumed to be because of the difference that the heated re-circulated fluid makes in the wall jet region.

The more realistic model with the large outlet domain shows increased accuracy with increased Reynolds numbers, Re, increased diameter ratios, d/D, and decreased dimensionless surface distances, L/d (most prominently with increased d/D). These trends support the motivation to apply the model to the spike tip of the SCRAP receiver since the geometric and flow characteristics applicable to SCRAP are larger diameter ratios $d/D \geq 0.089$, larger $Re \geq 45\,000$ and $1 \leq L/d \leq 6$. Similar trends are observable for the cone-like domain correlation, but as seen in the Nu distributions, the severe over-prediction of the second peak with no re-circulated fluid affects the high Re correlation most significantly.

4.5 Conclusion

The author set out to determine the capabilities of ANSYS Fluent™ at predicting published experimental results for all 27 cases by Lee *et al.* (1999). The process of validation has led to several discoveries in the sensitivities of the developed model. An attempt has been made to understand level of validity of the model and the correlation trends for different parameters.

The two most noticeable model sensitivities are the pipe exit conditions and the outlet region flow causing re-circulation. These two aspects of the model affect two different regions of the Nu distribution. The pipe exit conditions

Stellenbosch University https://scholar.sun.ac.za

(fully developed flow velocity and turbulence) affect the stagnation region and secondary peak region without affecting the wall jet region, while the re-circulation of heated fluid quite significantly affects the wall jet region and the secondary peak region without affecting the stagnation region. These two sensitivities are almost mutually exclusive, with an overlap observed between the local minimum and local maximum of the secondary peak region.

The shapes of the simulated Nu distributions correlate well with the experimental results, where the local minimum and maximum positions have good agreement. Some uncertainty with regard to the experimental environment and geometry reduces the certainty of numerical replication. Since the model is shown to be highly sensitive to the outlet flow conditions, these uncertainties are significant. Given more outlet region characteristics, the numerical replication would be more accurate, possibly leading to better wall jet correlation.

Had Lee *et al.* (1999) published more information on the fully developed pipe flow velocity and turbulence conditions, the inlet characteristics could have been validated and the stagnation region predictions may have been better correlated. The trends of poor correlation with the experimental results could be attributed to the incapabilities of the numerical model, or to the unknown experimental conditions, or to a combination of the two.

It is clear that, although the model shows excellent correlation in some cases, there is more work required to develop a robust model that performs well across all cases. Since this validation case study of Lee *et al.* (1999) only covers part of the parametric set analysed in chapter 5 and chapter 6, it is recommended that further work is done to increase the robustness and validity of the developed model. This could be achieved by doing a new experimental test campaign that is sensitive to the influencing parameters identified in this numerical analysis.

However, the trends show an increasing level of numerical agreement with experimental results in the direction towards the geometric and flow characteristics of the SCRAP receiver's design point. Thus, it is asserted that, for the purposes of the parametric analysis performed to improve the spike tip design, the developed model shows acceptable performance with $< 10\,\%$ error in the region of applicable parameters, and an increased level of agreement in the direction of parametric extrapolation. The turbulence model of choice for the application is the k-ω SST turbulence model with the intermittency transition extension.

Stellenbosch University https://scholar.sun.ac.za

Chapter 5

Setup of numerical model application[1]

The CFD validation process of jet impingement on a concave hemisphere has shown that confidence can be placed in the capabilities of the k-ω SST intermittency transition RANS turbulence model to predict heat transfer of the cooling mechanism where a $y^+_{\max} < 1$ is used in 2-d axisymmetry. This CFD setup is therefore further used to perform a parametric analysis on the nozzle design of the reference spike of SCRAP presented by Lubkoll (2017).

The geometry of the intended nozzle design in the spike tip of SCRAP is presented in Figure 5.3 in section 5.2.2. The nozzle diameter, d, as will be later revealed, is the most significant design parameter of those being analysed in the current work.

The reduction of the nozzle diameter with a constant mass flow rate, causes an increase in nozzle exit velocity, which increases the jet's heat transfer characteristics. The heat transfer coefficients of jet impingement are known to be high (Colucci and Viskanta, 1996). Increased heat transfer results in lower receiver surface temperatures and therefore less losses and better receiver efficiencies. However, the disadvantage of decreasing the nozzle diameter is that the resultant velocity increase leads to a higher dynamic pressure which is not recovered by a diffuser, and the rapid expansion results in a higher pressure drop. Diffusing the jet to recover the dynamic pressure would decrease the jet's velocity and hence heat transfer characteristics.

This trade-off between heat transfer and pressure drop does not present an obvious solution to the design problem. This is because it is typically observed that, with a reduced nozzle diameter, external thermal losses decrease (caused by increased heat transfer and hence decreased material temperature), and pressure drop increases. To be able to identify a balance between the two for better performance, both heat transfer and pressure drop should be considered in a quantification of the receiver's performance in something like the efficiency of the entire gas turbine cycle.

[1]Parts of this chapter have been published in McDougall *et al.* (2018)

Stellenbosch University https://scholar.sun.ac.za

There are nozzle design parameters to consider other than just the nozzle diameter. Some of the other design parameters are explored in this chapter in order to determine their sensitivities. The results of the sensitivity study determine the scope of the parametric analysis.

This chapter includes a replication and comparison of the jet impingement CFD work by Lubkoll (2017) using the current developed model settings. It also reports on the numerical environment setup used to perform the analysis on SCRAP, going further into design parameter considerations and setting up a parametric set. The results of the parametric analysis are discussed in chapter 6 with a method of quantifying the performance of a design.

5.1 Comparison with previous work

The current study is based on a recommendation by Lubkoll (2017) for further work to be done where a detailed CFD study gives more insight into the jet impingement cooling mechanism. His recommendation was that such an analysis could identify a spike tip geometry that improves heat transfer and/or decreases the pressure drop.

Lubkoll (2017) performed a basic CFD analysis to determine the jet impingement heat transfer characteristics using a few different nozzle diameters with the standard k-ε turbulence model, which he validated against a flat plate case. These results were implemented as a single spike-tip node in his heat transfer model.

Here, the author replicates the geometry and boundary conditions of the CFD model by Lubkoll (2017)[2], changing the model settings to those that were selected to be validated in chapter 4.

Comparing the local Nusselt number distributions of Lubkoll (2017) to the results of the current study results, significant differences are observed in Figure 5.1. Considering the previously mentioned differences between the k-ε and k-ω SST, it is seen specifically with $d = 7\,\text{mm}$ that the laminar boundary layer and transition to turbulent boundary layer flow is captured by k-ω SST and not by k-ε.

These local characteristics of the distribution were not considered in the heat transfer model of Lubkoll (2017). He applied an area-weighted average heat transfer coefficient to the model as a single node. His h_{avg} results are compared to the current study h_{avg} results in Figure 5.2.

It is observed that the k-ε based model by Lubkoll (2017) predicts higher h_{avg} than the current k-ω SST based model. A percentage difference less than $4\,\%$ is seen for the small diameter nozzles, $d \leq 10\,\text{mm}$. A larger difference is observed for the larger nozzles ($23\,\%$ for $d = 18\,\text{mm}$ and $59\,\%$ for $d = 26\,\text{mm}$).

Since Lubkoll (2017) considered area-weighted averages in the spike tip node of his heat transfer model and only considered nozzle diameters of

[2]The details of this analysis can be found in appendix G and appendix H of Lubkoll (2017), with the final results presented in section 2.3.8 of Lubkoll (2017)

Stellenbosch University https://scholar.sun.ac.za

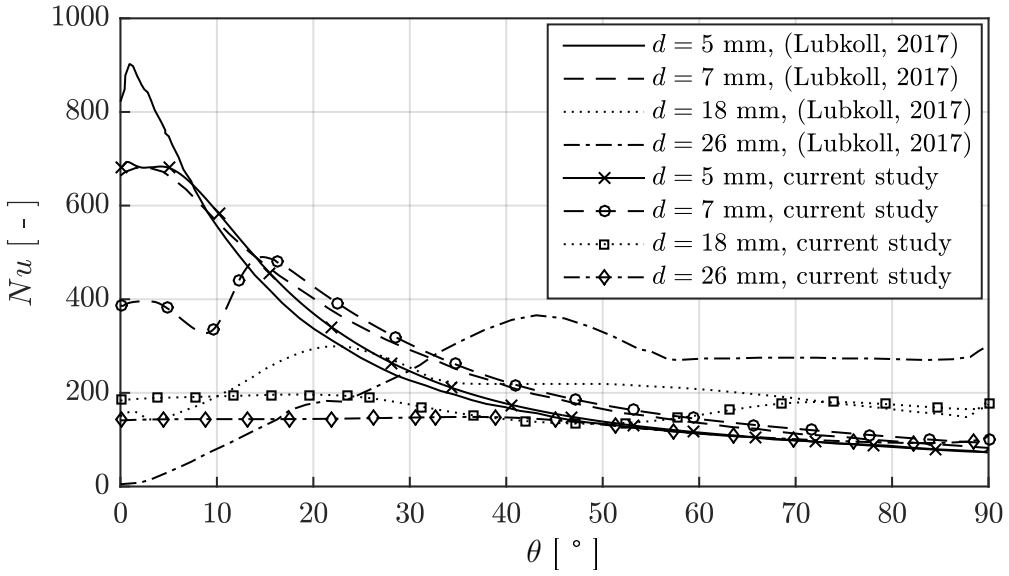

Figure 5.1: Nusselt number distribution comparison for different nozzle diameters, d

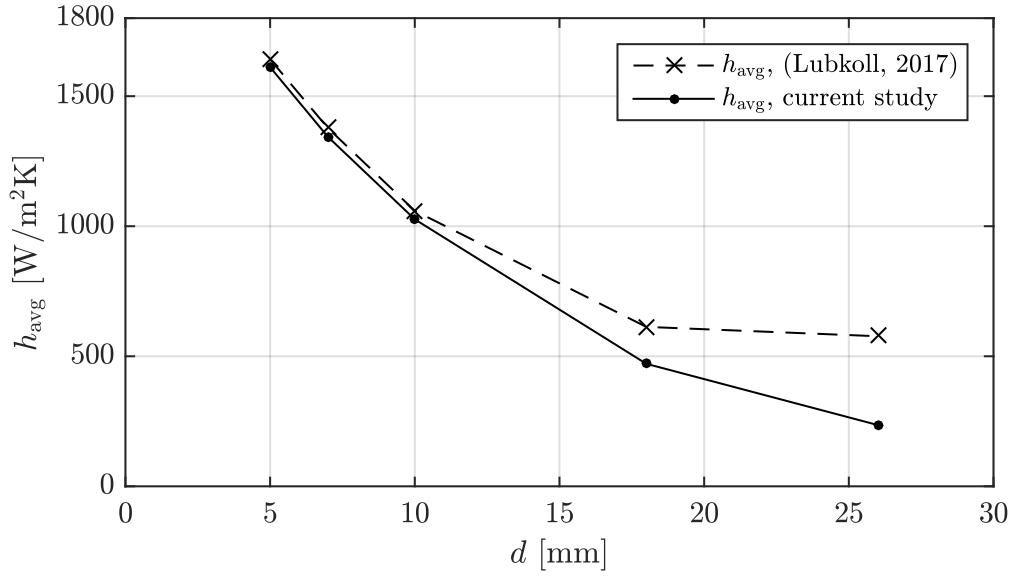

Figure 5.2: Comparison of h_{avg} by Lubkoll (2017) and current study for different nozzle diameters

Stellenbosch University https://scholar.sun.ac.za

$d \leq 10\,\text{mm}$, his heat transfer coefficients obtained using the k-ε based model are further validated here.

Note that the weighting of the local heat transfer characteristics in the distribution increases along the arc length from the stagnation point because the discretised surface area increases. The results of the small nozzle diameters in Figure 5.1 display similar behaviour in the two models far from the stagnation region. This is the area that weighs the most and which gives testament to the good correlation between the two models. Larger differences are observed in the wall jet region for $d = 18\,\text{mm}$ and $d = 26\,\text{mm}$.

This simulation was performed with a constant temperature boundary condition on the hemisphere. Considering the local heat transfer effects of jet impingement is important when the boundary condition is not constant, but rather a distribution. This is further discussed in section 5.2.

5.2 Spike tip model setup

The CFD simulation environment is introduced in this section with details about the base case design, the geometry and boundary conditions, the mesh generation, the material and fluid properties, and the utilised numerical method.

5.2.1 Reference design by Lubkoll (2017)

The analysis performed in the current study aims at developing an understanding of the sensitivity of certain nozzle geometric parameters on the performance of the SCRAP receiver. This increases the available content usable in developing a business case for commercialising the receiver. It also presents insight into the usefulness of jet impingement for solar applications.

Lubkoll (2017) analysed the performance of the receiver with some assumptions to simplify the problem (see the reference design of Lubkoll (2017)). The geometric and environmental assumptions made in the current study are based on the reference design of Lubkoll (2017) and are tabulated as the input parameters in Table 5.1.

5.2.2 Geometry and boundary conditions

The scope of this study is to model the spike tip jet impingement. Therefore, the numerical domain includes regions upstream and downstream such that a prediction of the jet impingement flow characteristics in the spike tip can be made.

Upstream of the spike tip, a 20 mm tube segment is included in the domain before the nozzle. However, fully developed pipe flow is modelled separately and the resulting turbulence and velocity profiles are applied as the inlet

Stellenbosch University https://scholar.sun.ac.za

Table 5.1: Assumptions and input parameters of the gas turbine cycle and spike tip flow conditions

Description	Value
Spike outer diameter, D_{out}	70 mm
Inner tube outer diameter, d_{out}	30 mm
Inner tube and end cap wall thickness	2 mm
Compressor compression ratio	10
Wind velocity	0 m/s
Spike mass flow rate, $\dot{m}$	0.0326 kg/s
Heliostat facet size	1 m × 1 m
Solar flux on spike outer tube, $\dot{q}''_{spike}$	60 kW/m^2
Maximum solar flux on spike tip, $\dot{q}''_{max}$	1.265 MW/m^2
Spike tip inlet temperature, $T_{in,tip}$	426 °C

boundary conditions. Therefore, the inner pipe is essentially included in the numerical domain[3].

Downstream of the spike tip is a 150 mm annulus, starting at the connection of the end cap. The fins in this section of the concept are not modelled in this study. Assuming that the fins start at the end of the nozzle slope (about 30 mm into the annulus for a nozzle of $d = 10$ mm), the fins are assumed to have a negligible effect on the et impingement heat transfer. There is a lot of potential for being creative with the starting point of the fins that can potentially favour the thermal performance of the receiver. The fins' effect on the jet impingement heat transfer is, however, ignored for the purposes of this study so that the simplification of the 2-d axisymmetry can be assumed.

Figure 5.3 shows the geometry of the 2-d axisymmetric numerical domain which includes the fluid domain and the solid domains of the end cap and 150 mm of outer tubing. The solid of the inner pipe and nozzle are not modelled as part of the computational domain and are 2 mm thick.

Dimensions shown as variables, such as the nozzle diameter, d, nozzle-to-surface distance, L, and nozzle slope, α, are elaborated on in section 5.4.

Similar to the validation model in chapter 3, the model is axisymmetric with boundary conditions that include: an axis of symmetry; a velocity inlet; a pressure outlet; smooth walls and a wall with a heat flux applied to it. There is a fluid and solid domain.

5.2.3 Mesh generation

Generating a mesh for a geometry with curved surfaces makes structured meshes difficult to achieve. The domain dividers seen in Figure 5.3 as the thin, black lines divide the computational domain into pieces for meshing purposes. Three sections of the domain are unmapped meshes while the rest

[3]The inlet temperature is specified as 426 °C and no heat transfer between the upstream and downstream domains in the radial direction through the inner tube is modelled.

Stellenbosch University https://scholar.sun.ac.za

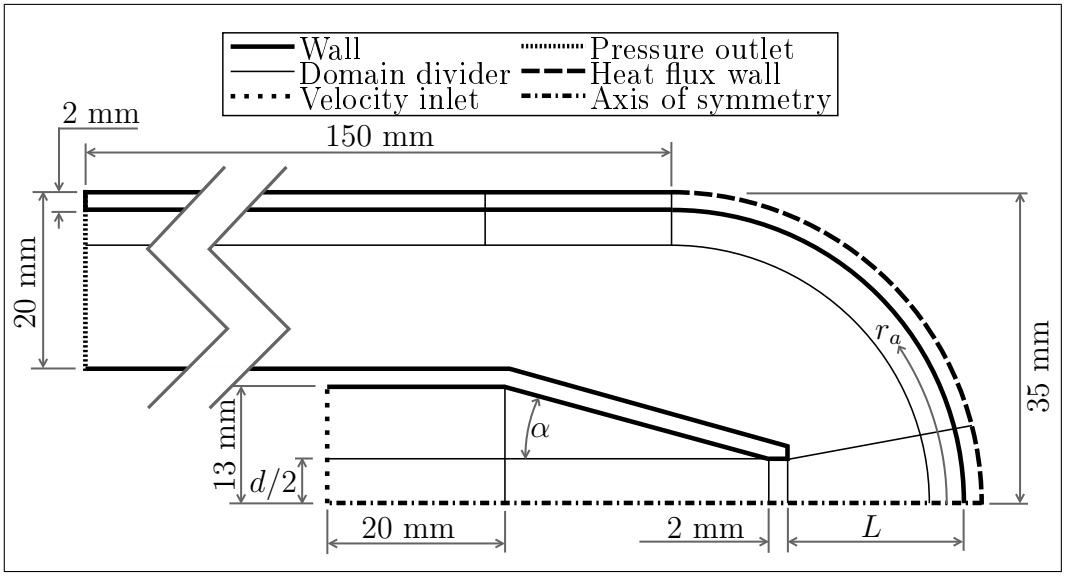

Figure 5.3: Geometry and boundary conditions of the computational domain with domain dividers for meshing purposes and dimensions

of the domain is mapped. This is done to decouple the 90° bend in the mesh to allow for continuous mapping.

Figure 5.4 displays a mesh where $d = 10\,\text{mm}$, $L = 22\,\text{mm}$ and $\alpha = 15°$, with 311 258 cells. The mesh is designed to have refined area where gradients are expected, specifically in near wall regions where $y^+_{\text{max}} < 1$ is achieved.

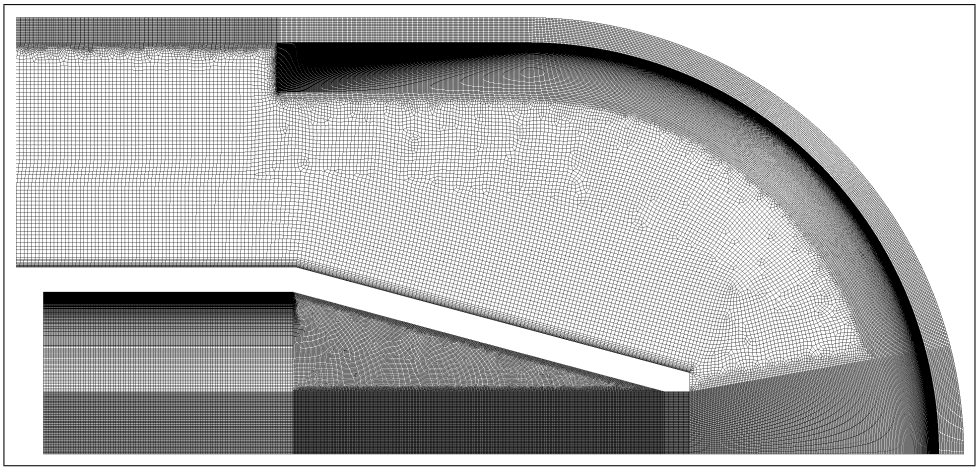

Figure 5.4: Geometric depiction of SCRAP spike tip with a nozzle showing boundary conditions and dimensions

Further discussions on the generation of multiple meshes for the parametric analysis can be found in subsequent sections.

5.2.4 Material and fluid properties

The fluid and solid domains are given air and Inconel alloy 718 properties respectively.

Stellenbosch University https://scholar.sun.ac.za

Large temperature differences are experienced in the spike tip, therefore constant fluid properties would not be a valid assumption and the ideal gas assumption is used. The density is calculated in the simulations using the ideal gas law. Since the inlet temperature of the nozzle is 426 °C and subsequently rises, the following polynomials for other air properties are valid as functions of only temperature (developed with data from Span (2010)):

$$c_\mathrm{p}\ [\mathrm{J/(kg\,K)}] = -8.256 \times 10^{-5}\ T^2 + 0.350\ T + 873.829 \tag{5.1}$$

$$k\ [\mathrm{W/(m\,K)}] = -7.930 \times 10^{-9}\ T^2 + 6.676 \times 10^{-5}\ T + 891.095 \times 10^{-5} \tag{5.2}$$

$$\mu\ [\mathrm{kg/(m\,s)}] = -6.898 \times 10^{-12}\ T^2 + 4.229 \times 10^{-8}\ T + 7.974 \times 10^{-6} \tag{5.3}$$

The properties of air in these equations: the specific heat, c_p, the thermal conductivity, k, the dynamic viscosity, μ, and the temperature, T, in Kelvin.

For the purposes of this study, Inconel alloy 718 is selected as the solid material of choice due to its relatively high melting point, strength and oxidation properties. Typically, alloys with high melting points possess low thermal conductive ability. This is the case with Inconel. It will be seen later that a material with a high melting point is necessary for a receiver that is being exposed to elevated solar fluxes.

The properties for Inconel alloy 718 are obtained from SMC (2007). Constant density and specific heat are assumed at $\rho = 8193.252\,\mathrm{kg/m^3}$ and $c_\mathrm{p} = 435\,\mathrm{J/(kg\,K)}$ respectively. A polynomial described in equation 5.4 is used to calculate the temperature-dependant thermal conductivity, k, of Inconel alloy 718, where T is the temperature in °C.

$$k\ [\mathrm{W/(m\,K)}] = 160.31 \times 10^{-4}\ T + 11.032 \tag{5.4}$$

All of the above-mentioned property polynomials are utilised in Fluent™ to specify the fluid or solid properties.

5.2.5 Numerical method

The computational methods used in Fluent™ resulting from the validation study performed in chapter 3 and chapter 4 are listed as follows[4]:

- 2-d axisymmetry
- Steady state RANS simulation
- Turbulence model (7) from section 4.1 (k-ω SST with production of k limitation and the intermittency transition model)
- Air and Inconel alloy properties for fluid and solid domains respectively as described in section 5.2.4
- Fully developed velocity and turbulence profiles specified at velocity inlet BC (modelled separately with properties at $T = 426\,°\mathrm{C}$ and a mass flow rate of $\dot{m} = 0.0325\,\mathrm{kg/s}$)

[4]Flow conditions are based on the reference design by Lubkoll (2017)

Stellenbosch University https://scholar.sun.ac.za

- Pressure outlet BC with specified pressure that is determined iteratively with each geometry's resultant pressure, such that the inlet absolute pressure is 10 bar (9 bar gauge).
- Heat flux BC specified using a UDF that is further described in section 5.5
- Convergence criterion of 1×10^{-6} for all equations except for the energy equation of which the convergence criteria is 1×10^{-12}
- Coupled pressure-velocity solution method
- Standard pressure discretisation scheme
- Least squares cell based gradient discretisation scheme
- Second order upwind scheme for all other discretisation
- Pseudo-transient method with higher-order term relaxation

5.3 Spike tip pressure drop

To verify the validity of the pressure drop being simulated, some empirical correlations are used together with Bernoulli's equation to estimate the spike tip pressure drop. Some of the correlations are referred to by Lubkoll (2017) who performed this analysis, but the results of the current study show a drastic difference to the results of Lubkoll (2017). It seems that Lubkoll (2017) used Bernoulli's equation for the entrance into the ducts, but not for the exiting of the nozzle.

The pressure drop considerations in the calculated value for comparison to the simulation results include: a pressure drop due to the slope of the nozzle, a pressure drop due to the rapid change in cross-sectional area as the fluid exits the nozzle, and a pressure drop due to the fluid turning around after impinging on the end cap. The ducts are not simulated in this study, therefore the expected pressure drop for entering the ducts is omitted from this calculation. These three pressure drop terms are summarised in Table 5.2.

Table 5.2: Pressure drop calculation contributions

Description	Equation	Comment	Reference
Nozzle slope	$\xi\rho V^2/2$	$\xi = 0.04$ and V at nozzle exit	(Kast, 2010)
Nozzle exit	$\rho(V_1^2 - V_2^2)/2$	V_1 at nozzle exit and V_2 at annulus	Bernoulli
Impingement	$\xi\rho V^2/2$	$\xi = 0.1$ and V at annulus	(Idelchik, 1986)

The calculated and simulated results are compared in Table 5.3 where good correlation is observed. The results from Lubkoll (2017) are included for comparison[5]. The loss coefficient of the nozzle slope is $\xi = 0.04$ from Kast (2010) assuming a slope angle of $\alpha \leq 20°$. The simulations performed include a nozzle with $\alpha = 15°$. A more detailed analysis on the slope angle is shown in section 5.4.

[5]Similar results to those found by Lubkoll (2017) are obtained when replicating his calculations

Stellenbosch University https://scholar.sun.ac.za

Table 5.3: Pressure drop at different nozzle diameters comparing calculated and simulated results

	Δp [Pa]					
d [mm]	Nozzle slope	Nozzle exit	Impingement	Total	Simulation	Lubkoll (2017)
7	2870	71 738	7175	81 784	79 361	10 000
10	689	17 213	1723	19 625	17 370	2500
15	136	3389	340	3865	3321	800
20	43	1062	108	1213	1011	160
26	0	427	44	471	380	113

The Bernoulli nozzle exit term plays a significant role in the pressure drop since it contains the square of the nozzle exit velocity. The nozzle exit velocity is inversely proportional to the square of the nozzle diameter. The pressure drop can therefore be assumed to be inversely proportional to d^4. This relationship is evident in Figure 5.5 which plots the calculated and simulated pressure drops against nozzle diameter.

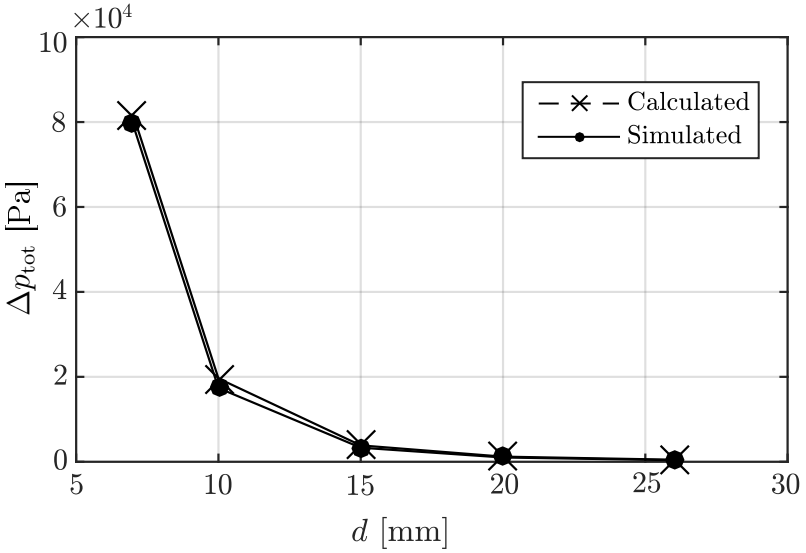

Figure 5.5: Comparison of Δp_{tot} by calculation and simulation for different nozzle diameters

5.4 Geometric sensitivities

This study includes the analysis of three geometric parameters of the nozzle design, namely:

- nozzle diameter, d,
- nozzle-to-surface distance, L, and
- nozzle slope angle, α

Altering the nozzle diameter (assuming a constant mass flow rate) increases the Reynolds number, Re, and quadratically increases the average nozzle exit fluid velocity. An increase in fluid velocity is desirable for increased jet impingement heat transfer, but it comes at the cost of increased pressure drop.

Stellenbosch University https://scholar.sun.ac.za

Here, the sensitivity to heat transfer and pressure drop of the three mentioned parameters are investigated to determine the significance of each parameter for consideration in a further parametric analysis. For this sensitivity study only, an arbitrary uniform heat flux of $\dot{q}'' = 463\,000\,\mathrm{W/m^2}$ is applied to the end cap.

5.4.1 Nozzle slope angle

Kast (2010) determined that a nozzle with a continuously reducing diameter at an angle of $\alpha \leq 20°$ does not exhibit flow separation and therefore results in a low pressure drop in comparison to angles greater than 20°.

To test this, a sensitivity study is done on α. Simulations are run using eight different slope angles, a constant nozzle diameter of $d = 5\,\mathrm{mm}$ and a constant nozzle-to-surface distance ratio of $L/d = 2$. Figure 5.6 shows the results of the pressure drops of these simulations. It is observed that the pressure drop increases significantly with slope angles of $\alpha > 30°$.

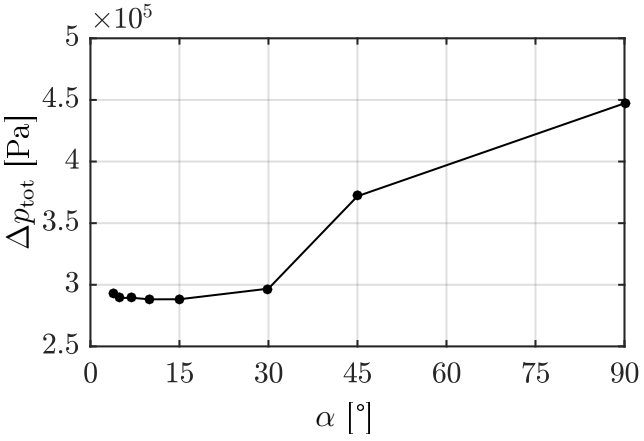

Figure 5.6: Pressure drop over spike tip region using different nozzle slope angles α for a nozzle diameter of $d = 5\,\mathrm{mm}$

A slope angle of $\alpha = 15°$ is selected as practically reasonable and is henceforth used in all simulations.

5.4.2 Nozzle-to-surface distance

The nozzle-to-surface distance parameter, L, is less sensitive than the slope angle α and nozzle diameter, d, for pressure drop and heat transfer. Figure 5.7 shows that the lower the distance ratio, L/d, the better the heat transfer. The pressure drop, however, spikes at $L/d = 1$ likely due to the throttling of the flow against the impingement surface. At $2 \leq L/d \leq 4$, lower pressure drops are observed.

Stellenbosch University https://scholar.sun.ac.za

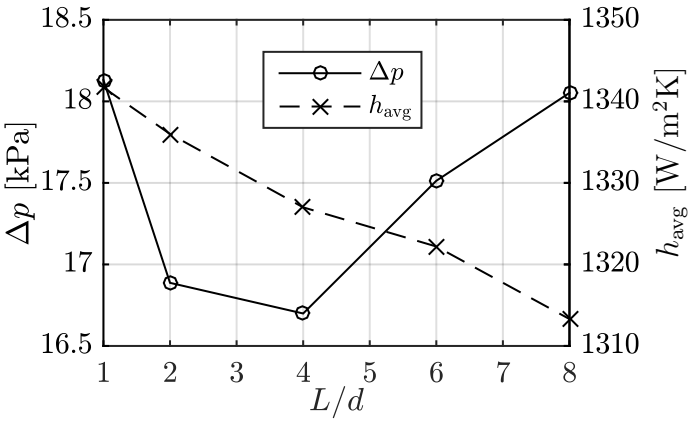

Figure 5.7: Pressure drop and heat transfer coefficient over spike tip region using different nozzle-to-surface distances, L, for a nozzle diameter of $d = 8\,\text{mm}$

5.4.3 Nozzle diameter

With a constant mass flow rate, $\dot{m}$, the Re is inversely proportional to d and the average nozzle outlet velocity, $\bar{V}$, increases quadratically with a decreasing d.

As seen in section 5.3 with Bernoulli's equation, the rapid expansion of the jet contributes to about 85 % of the calculated pressure drop. This is illustrated in Figure 5.8 with the total pressure contour map of a 10 mm nozzle simulation. A venturi would help to recover much of the pressure, but that would diffuse the jet and reduce the heat transfer capability of the jet.

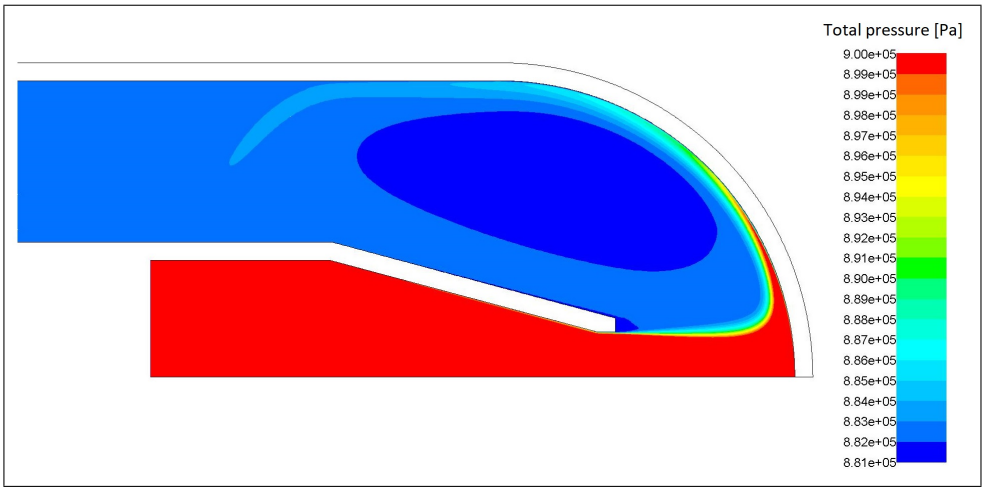

Figure 5.8: A contour map of total gauge pressure with $d = 10\,\text{mm}$ and $L = 22\,\text{mm}$

Figure 5.9 illustrates the excessive sensitivity of the nozzle diameter parameter to pressure drop and heat transfer. This parameter is the most sensitive parameter of the nozzle design.

Stellenbosch University https://scholar.sun.ac.za

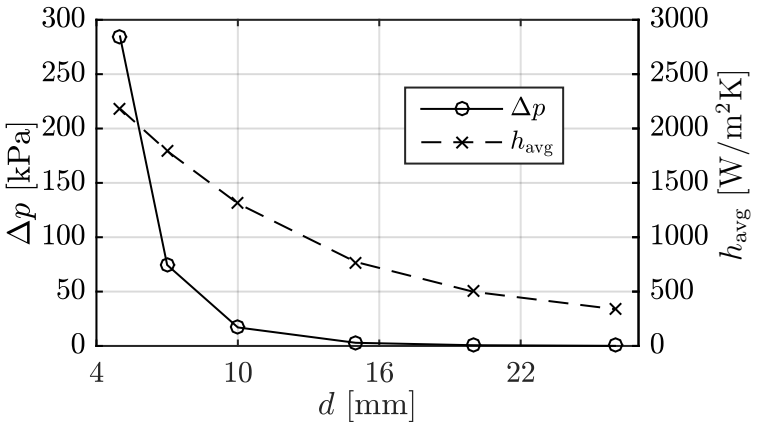

Figure 5.9: Pressure drop and heat transfer coefficient over spike tip region using different nozzle diameters, d, for a distance ratio of $L/d = 2$

5.5 Parametric set

It is established in the sensitivity study of the slope angle that at $\alpha \leq 30°$ there is a negligible difference in pressure drop. This parameter is therefore not considered in the parametric analysis and a constant of $\alpha = 15°$ is used.

To study the effects of several parameters and how they interact with each other, a parametric set must be developed and simulations run for each design point in that parametric set. The two parameters identified in the sensitivity study are nozzle diameter, d, and nozzle-to-surface distance, L. These are used in the parametric analysis, as well as a third parameter that is the input solar flux profile, $\dot{q}''$, on the outer surface of the dome as a BC.

Nozzle diameters of $d = \{6\,\text{mm}$ to $25\,\text{mm}\}$ in increments of 1 mm result in 20 different nozzle diameters. Three different nozzle-to-surface distances, $L = 12\,\text{mm}$, $L = 22\,\text{mm}$, and $L = 32\,\text{mm}$, are analysed. The geometric set resulting from just these two geometric parameters adds up to 60 design points.

This geometric parametric set is simulated using eight different flux variations assuming ideal gas (variable fluid properties), and with one flux profile assuming constant fluid properties. These nine variations are described in Table 5.4.

The various absorbed solar flux terms are described in the following equations:

$$\dot{q}''_{\text{sol}(1)} = 632\,513\ \alpha_{\text{opt}} \tag{5.5}$$

$$\dot{q}''_{\text{sol}(2)} = \alpha_{\text{opt}}(1\,265\,000 - 60\,000)\cos\theta + 60\,000\ \alpha_{\text{opt}} \tag{5.6}$$

$$\dot{q}''_{\text{sol}(3)} = \alpha_{\text{opt}}(-370\,979\,174\ r^2 + 1\,121\,309) + 60\,000\ \alpha_{\text{opt}} \tag{5.7}$$

$$\dot{q}''_{\text{sol}(4)} = \alpha_{\text{opt}}(-100\,823\,678\ r^{1.5} + 1\,299\,704) + 60\,000\ \alpha_{\text{opt}} \tag{5.8}$$

$$\dot{q}''_{\text{sol}(5)} = \alpha_{\text{opt}}(1\,000\,000 - 47\,430)\cos\theta + 47\,430\ \alpha_{\text{opt}} \tag{5.9}$$

$$\dot{q}''_{\text{sol}(6)} = \alpha_{\text{opt}}(750\,000 - 35\,573)\cos\theta + 35\,573\ \alpha_{\text{opt}} \tag{5.10}$$

$$\dot{q}''_{\text{rad}} = \varepsilon_{\text{opt}}\sigma(T_s^4 - T_{\text{sky}}^4) \tag{5.11}$$

Stellenbosch University https://scholar.sun.ac.za

Table 5.4: Variations of flux inputs to model

#	Flux input	Description
1	$\dot{q}''_{\text{sol}(2)}$	Cosine profile solar flux (constant fluid properties)
2	$\dot{q}''_{\text{sol}(1)}$	Uniform solar flux
3	$\dot{q}''_{\text{sol}(1)} - \dot{q}''_{\text{rad}}$	Uniform solar flux with radiation losses
4	$\dot{q}''_{\text{sol}(2)}$	Cosine profile solar flux
5	$\dot{q}''_{\text{sol}(2)} - \dot{q}''_{\text{rad}}$	Cosine profile solar flux with radiation losses (a)
6	$\dot{q}''_{\text{sol}(3)} - \dot{q}''_{\text{rad}}$	Quadratic profile solar flux with radiation losses
7	$\dot{q}''_{\text{sol}(4)} - \dot{q}''_{\text{rad}}$	Power function profile solar flux with radiation losses
8	$\dot{q}''_{\text{sol}(5)} - \dot{q}''_{\text{rad}}$	Cosine profile solar flux with radiation losses (b)
9	$\dot{q}''_{\text{sol}(6)} - \dot{q}''_{\text{rad}}$	Cosine profile solar flux with radiation losses (c)

where α_{opt} is the absorptivity of 0.9 assumed to be a result of using Pyromark 2500 as a selective coating on the receiver (Ho *et al.*, 2013), θ is the end cap curvature angle starting at zero at the stagnation point, ε_{opt} is the emissivity of the receiver surface of 0.9 assumed to be a result of using Pyromark 2500 as a selective coating on the receiver (Ho *et al.*, 2013), and σ is the Stefan-Boltzmann constant. For an example of the code used to define the UDF, see Appendix A.4.

Lubkoll (2017) performed a ray-tracing analysis on the SCRAP receiver using Tonatiuh with various sizes of heliostats, assuming a direct normal irradiation (DNI) of 1000 W/m^2. The smaller heliostats achieved higher flux penetration into the receiver to the base of the spikes, with a lower maximum flux at the spike tips than the larger heliostats. Smaller heliostats are therefore more desirable to achieve the volumetric effect and minimise radiation and external convective losses.

The result published by Lubkoll (2017) is 1.265 MW/m^2 on a disc perpendicular to the incoming radiation and an average of about 4.7 % of the disc value (60 kW/m^2) on the the cylinder. Following these results, it is assumed that the distribution from the stagnation point (experiencing the 1.265 MW/m^2) to the interface between the end cap and the spike (experiencing 60 kW/m^2) is a cosine function, due to the cosine losses.

The solar input function, $\dot{q}''_{\text{sol}(2)}$, is a cosine function assumption for the absorbed solar radiation using the above-mentioned maximum and minimum values. The solar input function, $\dot{q}''_{\text{sol}(1)}$, is the area-weighted average of the cosine function. The quadratic function, $\dot{q}''_{\text{sol}(3)}$, and power function, $\dot{q}''_{\text{sol}(4)}$, are determined by numerically solving for the coefficients, which results in an equation giving the same area-weighted average as the cosine function, $\dot{q}''_{\text{sol}(2)}$. These two extra flux profiles are developed to apply a different shape function with the same energy input to the spike tip so that the profile shape sensitivity can be analysed[6].

[6]Note that the cosine function assumes that no radiation is spilling from a wider range of heliostats. If this occurs, the energy input could potentially increase significantly

Stellenbosch University https://scholar.sun.ac.za

Two additional functions are included to study the effects of reduced DNI which would occur in the morning or afternoon. For $\dot{q}''_{\text{sol}(5)}$, a maximum flux from the solar field at the impingement point is assumed to be $1\,\text{MW/m}^2$ and $47.43\,\text{kW/m}^2$ on the the cylinder. Similarly, but with less DNI, $\dot{q}''_{\text{sol}(6)}$ assumes a maximum flux from the solar field at the impingement point of $0.75\,\text{MW/m}^2$ and $35.57\,\text{kW/m}^2$ on the cylinder. These additional two flux profiles apply reduced energy inputs into the receiver due to their area-weighted averages being smaller than $\dot{q}''_{\text{sol}(2)}$. This reduced solar input could be due to a reduction in DNI or a reduction in the concentration ratio. Figure 5.10 shows the different absorbed solar radiation ($\dot{q}''_{\text{sol}}$) profiles.

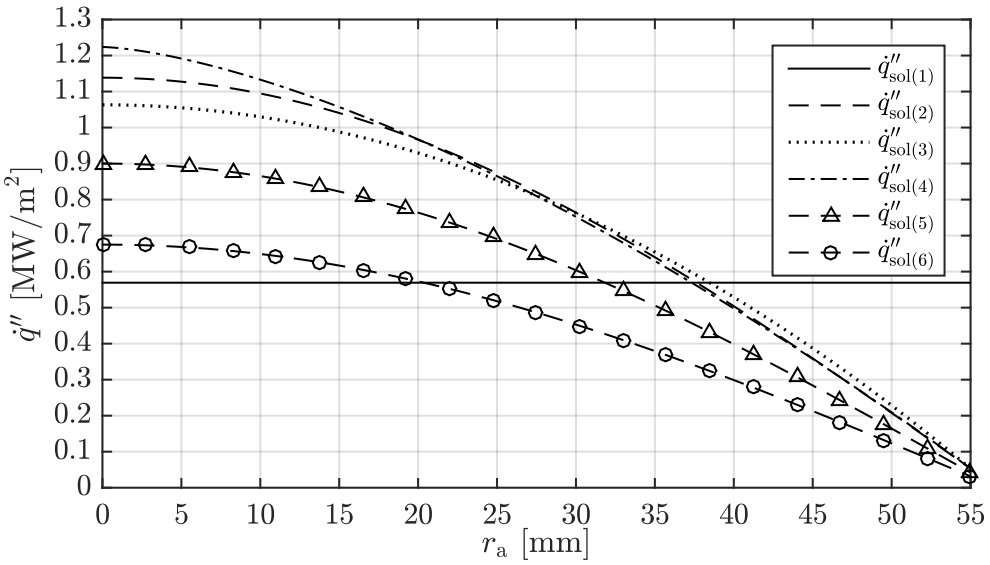

Figure 5.10: Graph of the four different absorbed solar flux $\dot{q}''_{\text{sol}}$ profiles used in the parametric analysis

The nine flux profiles, shown in Table 5.4, are applied as a BC to the outer surface of the end cap using a user-defined function (UDF). Appendix A.4 shows an example of the UDF of $\dot{q}''_{\text{sol}(2)} - \dot{q}''_{\text{rad}}$, where the flux input to the simulation as a BC is temperature-dependent and calculated locally at each node.

To perform the parametric analysis, simulations are run for all combinations of the varying parameters. For the geometric parametric set, 60 meshes are generated using ANSYS Workbench and its built-in parametrisation functionality. All meshes are refined enough to result in $y^+_{\text{max}} \leq 1$. Using MATLAB, the mesh, UDF and Fluent™ TUI files (see Appendix A.3 and Appendix A.4) are automatically duplicated and filed in their relevant combinations to be sent to the HPC. A total of 540 simulations make up the parametric set. Each simulation runs for two or three hours, but since they can be run in parallel, the set takes three to six days to complete, depending on license availability.

Stellenbosch University https://scholar.sun.ac.za

5.6 Conclusion

Following the developed and validated CFD model from chapter 4, the numerical setup is introduced in this chapter for the purpose of analysing the performance enhancement capability and sensitivity of the SCRAP receiver's spike tip jet impingement cooling mechanism.

From the initial sensitivity study, it is concluded that the slope angle is to be a fixed at $\alpha = 15°$. Further, nine flux profiles, 20 nozzle diameters, and three nozzle-to-surface distances form a parametric set of 540 design points. The results of the 540 simulations are analysed in chapter 6 with the objective of studying the sensitivity of the combination of geometric parameters, as well as various flux profiles, and the effects of radiation losses.

Using this extensive data set, the performance of the receiver and cycle will be estimated for each design point, to determine, with certain constraints, the parameters' effects on cycle performance. The design point with the best performance will be selected.

Stellenbosch University https://scholar.sun.ac.za

Chapter 6

Results and discussion of model application[1]

In analysing the results of the large parametric set, observations are made for various parameters included in the set. The purpose of analysing the effect of certain parameters is to gain a better understanding of the sensitivity of the design and operational parameters of the jet impingement spike tip, so that more informed decisions can be made when further analysis is done in the future and the possibility of commercialisation emerges. Understanding more about the little known flow phenomenon of jet impingement on a concave hemisphere is also an objective of this study.

Some of the parameter comparisons presented in the chapter from the set of 540 design points include: nozzle diameters, nozzle-to-surface distances, constant vs. ideal gas fluid properties, uniform vs. cosine flux profiles, with and without radiation losses, different shape flux profiles, and different magnitude flux profiles. Further, a method of quantifying the receiver efficiency and ultimately the efficiency of the gas turbine cycle is presented as a tool that can be used to quantify the effectiveness of the receiver design.

6.1 Geometric parameters

The sensitivity to pressure drop and heat transfer of the nozzle diameter, d, and nozzle-to-surface distance ratio, L/d, parameters is introduced in section 5.4.3. For this parametric set, the three nozzle-to-surface distances are fixed at $L = \{12\,\text{mm};\ 22\,\text{mm};\ \text{and}\ 32\,\text{mm}\}$ as opposed to fixed ratios of L/d. This is done for the practical reason that the nozzle should not be too far from the end cap, so as to reduce the length of the channels in the outer annulus. The L/d ratios therefore range from $L/d = 0.48$ to $L/d = 5.3$.

Figure 6.1 shows the average heat transfer coefficient h_{avg} and pressure drop Δp for the case with the uniform flux ($\dot{q}''_{\text{sol}(1)}$) applied and the constant fluid property assumption (1) from Table 5.4. The nozzle diameter range of

[1] Parts of this chapter have been published in McDougall *et al.* (2018)

Stellenbosch University https://scholar.sun.ac.za

$d = \{10\,\text{mm to } 25\,\text{mm}\}$ is used because the excessive range of the pressure drop for smaller d makes it difficult to observe differences for different L values.

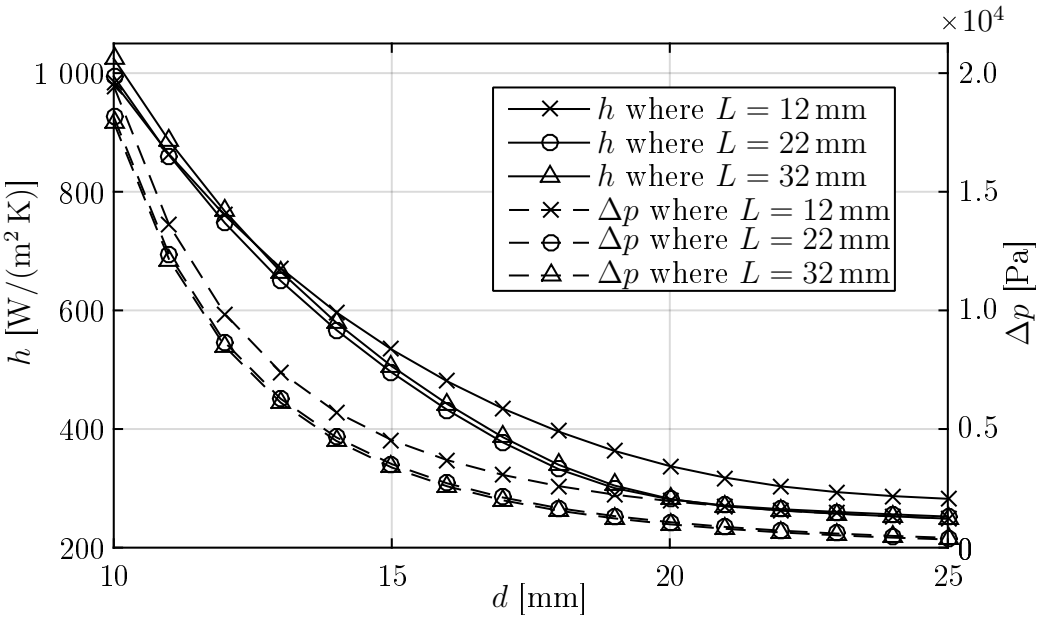

Figure 6.1: Average heat transfer coefficient, h_{avg}, and pressure drop, Δp, for different nozzle diameters, d, and nozzle-to-surface distances, L

The expected increasing heat transfer and pressure drop are observed with decreasing nozzle diameters. The small nozzle-to-surface distance, $L = 12\,\text{mm}$, appears to result in higher pressure drops for all nozzles. This is assumed to be because of flow throttling as discussed in section 5.4. The same observation can be made for the average heat transfer coefficient, h_{avg}, and in both cases, the effect is less evident for smaller d. This is because, as d increases, the edge of the nozzle gets closer to the end cap, further throttling the flow, which increases both Δp and h in comparison to larger L.

6.2 Fluid property assumption

Number (1) from Table 5.4 utilised the same flux BC as number (4), but (1) assumes constant fluid properties calculated at the inlet (426 °C and 10 bar) as opposed to the ideal gas assumption of (4). The results of these two parametric sets are compared in Figure 6.2 with $L = 12\,\text{mm}$.

Often the assumption of constant fluid properties is valid, even for compressible fluids, but in the case where large temperature and pressure differences are observed, the fluid properties can vary significantly. This behaviour is apparent in the comparison between the two fluid property assumptions.

With the ideal gas assumption, the fluid properties are a function of pressure and temperature. In the comparison shown in Figure 6.2, the simulation assuming constant properties results in higher heat transfer and

Stellenbosch University https://scholar.sun.ac.za

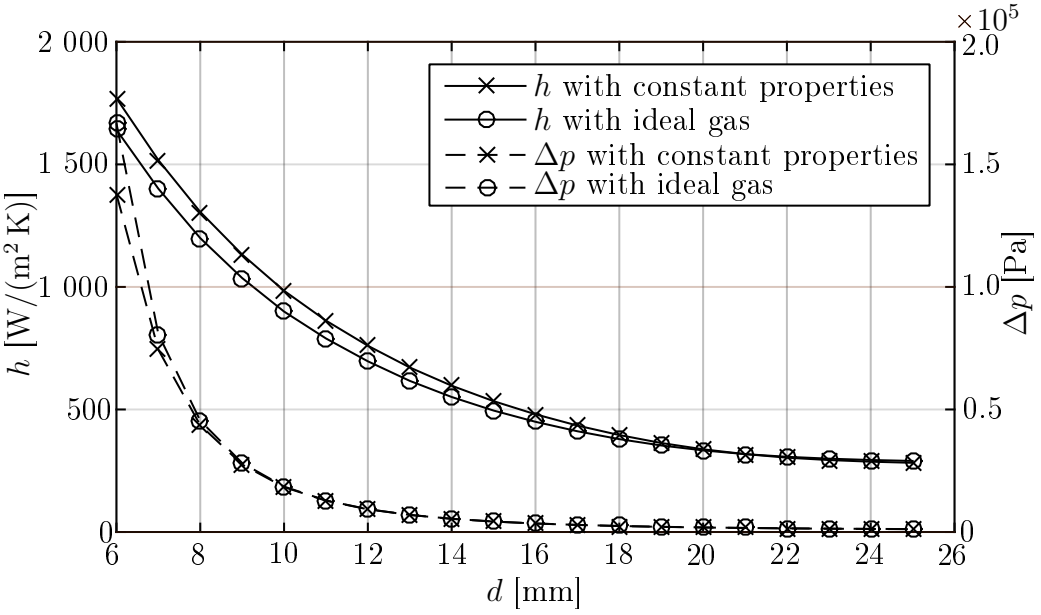

Figure 6.2: Heat transfer coefficient, h, and pressure drop, Δp, for different nozzle diameters, d, comparing fluid property assumptions

lower pressure drop (both favourable), while the ideal gas simulation is the other way around.

Consider the ideal gas assumption. The sudden drop in pressure at the nozzle exit (accentuated with small nozzles) causes the density to drop. In the extreme case of $d = 6\,\text{mm}$, the average densities at the inlet and outlet of the spike tip are approximately $\rho = 5\,\text{kg/m}^3$ and $\rho = 3.5\,\text{kg/m}^3$ respectively. The volume expansion causes flow acceleration which can contribute to a higher pressure drop than the case with constant fluid properties, including density.

The comparison clearly shows the sensitivity of the model to the fluid property assumption, as well as indicating the importance of using the correct fluid property assumption. Since the assumption of constant fluid properties is less realistic than the ideal gas assumption, and gives more favourable results, it is concluded that the ideal gas variable fluid properties be used, since they are more appropriate than assuming incompressibility.

6.3 Receiver thermal efficiency

Lubkoll (2017) found that the radiation losses (which are mostly attributed to the end cap) cause about a 5 % reduction in receiver efficiency for $d = 10\,\text{mm}$. The efficiency of the receiver is calculated as in equation 6.6, making a number of assumptions.

Since natural and forced external convective losses are out of the scope of this study, a 10 % receiver thermal efficiency drop is assumed for natural convection. This assumption is made following the reference design of Lubkoll (2017) and is applied to all design points for the entire length of the spike.

Stellenbosch University https://scholar.sun.ac.za

Some of the assumptions and variables of the receiver efficiency calculation are: A_{sp} and A_{tip} are the outer surface areas of the cylindrical part of the spike and the end cap respectively, $\dot{Q}_{in,sp}$ and $\dot{Q}_{in,tip}$ are the resultant inputs for the cylindrical part of the spike and the end cap respectively, $\eta_{nat} = 10\,\%$ is the loss due to natural convection, $\dot{Q}_{rad}$ is the temperature-dependant radiation loss assuming a view factor of 1 only on the end cap area, $\dot{q}''_{sol,sp}$ and $\dot{q}''_{sol,tip}$ are the absorbed solar flux inputs for the cylindrical part of the spike and the end cap respectively, $T_{out,tip}$ is the simulated outlet fluid temperature of the spike tip, $\Delta T_{out,tip(nat)}$ is the expected reduction in tip outlet temperature, $T_{in,tip} = 700\,\mathrm{K}$, due to natural convection, and $c_{p,avg}$ is the heat capacity of air at the average temperature between the inlet and outlet.

$$\dot{Q}_{sol,sp} = \dot{q}''_{sol,sp} A_{sp} \tag{6.1}$$

$$\dot{Q}_{sol,tip} = \dot{q}''_{sol,tip} A_{tip} \tag{6.2}$$

$$\Delta T_{out,tip(nat)} = \eta_{nat} \dot{Q}_{sol,tip} / (\dot{m} c_{p,avg}) \approx 13\,\mathrm{K} \tag{6.3}$$

$$\dot{Q}_{in,sp} = \dot{Q}_{sol,sp}(1 - \eta_{nat}) \tag{6.4}$$

$$\dot{Q}_{in,tip} = \dot{m} c_{p,avg}(T_{out,tip} - \Delta T_{out,tip(nat)} - T_{in,tip}) \tag{6.5}$$

$$\eta_{rec} = \frac{\dot{Q}_{in,sp} + \dot{Q}_{in,tip}}{\dot{Q}_{sol,sp} + \dot{Q}_{sol,tip}} \tag{6.6}$$

Note that the radiation losses in the spike tip are taken into account in some of the applied temperature-dependent UDFs and therefore the simulated outlet fluid temperature, $T_{out,tip}$, takes the radiation losses into account.

6.4 Flux profile parameters

As shown in Figure 5.10 of section 5.5, six different solar flux profiles are developed to study their effects on the thermal characteristics of the jet impingement mechanism implemented in the SCRAP receiver. Four of these ($\dot{q}''_{sol(1)}$, $\dot{q}''_{sol(2)}$, $\dot{q}''_{sol(3)}$ and $\dot{q}''_{sol(4)}$) have the same area-weighted average and are use to observe the sensitivity of the heat transfer mechanism to the shape of the solar flux input.

An additional two solar flux profiles ($\dot{q}''_{sol(5)}$ and $\dot{q}''_{sol(6)}$), also cosine based like $\dot{q}''_{sol(2)}$, simulate a reduced solar flux input as would be the case in the morning or afternoon. In addition to the sensitivity to solar flux input, $\dot{q}''_{sol}$, the effect of radiation losses, $\dot{q}''_{rad}$, is also analysed. Note that there is negligible difference between all of pressure drop, Δp, results of the parametric sets to follow and the ideal gas results of Figure 6.2. The focus henceforth is therefore placed on the heat transfer characteristics unless otherwise stated.

Stellenbosch University https://scholar.sun.ac.za

6.4.1 Uniform vs. cosine profile

Part of the motivation to analyse the local effects of jet impingement in the spike tip stems from the fact that the boasts high heat transfer capabilities in the stagnation region, where the receiver expects to experience a high solar flux. The local effects are therefore of importance because a high local solar flux input at the stagnation point requires elevated cooling to prevent melting of receiver materials. A single node calculation across the average of the end cap does not provide the local information required and will most likely be incorrect.

Figure 6.3 displays some heat transfer results of the uniform solar flux, $\dot{q}''_{\text{sol}(1)}$, and the cosine solar flux profile, $\dot{q}''_{\text{sol}(2)}$.

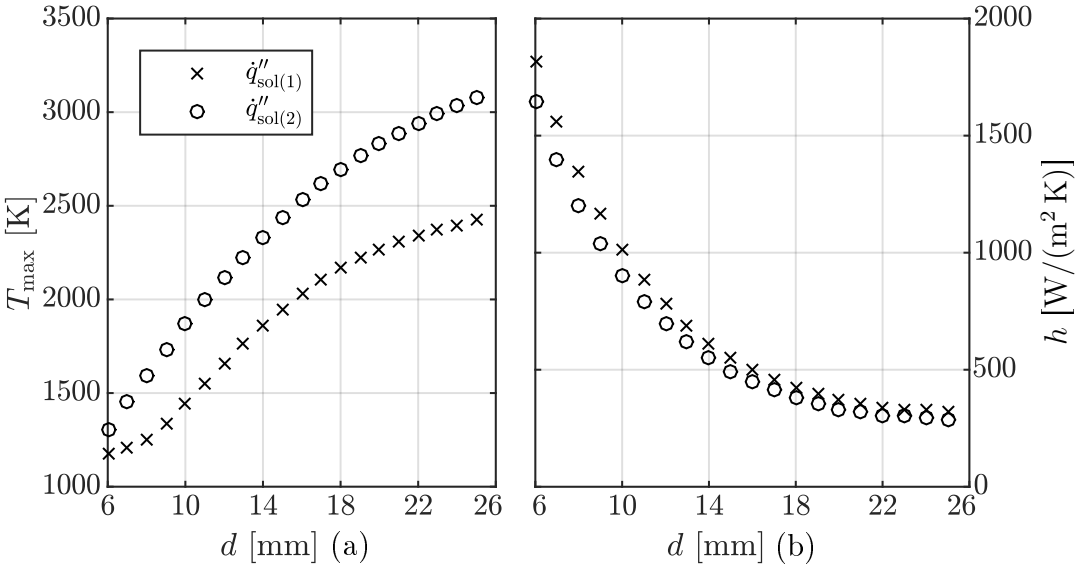

Figure 6.3: A comparison of the application of a uniform flux and a cosine flux profile with the same area-weighted averages at different nozzle diameters, where $L = 12\,\text{mm}$ showing (a) maximum surface temperature and (b) average heat transfer coefficient

Although, in the case of $\dot{q}''_{\text{sol}(2)}$, the jet impinges on the point of maximum flux, the maximum surface temperature is still higher than that of the uniform flux input. This is because the excessive maximum flux, $\dot{q}''_{\max}$, expected from the solar field is $1.265\,\text{MW/m}^2$.

It is noted that the maximum surface temperatures are very high and exceed the melting point of Inconel alloy 718, but these results ignore all losses and therefore all the energy applied by the sun is absorbed by the receiver, which results in these large temperatures.

To demonstrate the significance of the difference between the uniform flux BC[2] and the cosine flux profile BC, Figure 6.4 shows the solid material

[2]Note that the uniform flux BC is simply utilised as a comparison BC with the same area-weighted average as the expected profile, and is not at all realistic

Stellenbosch University https://scholar.sun.ac.za

(coloured by temperature) and the path lines of the fluid (coloured by velocity) for two extreme cases of d, with $L = 22\,\text{mm}$. Note that plots (a) and (b) of Figure 6.4 share temperature and velocity colour maps, and the same applies to plots (c) and (d).

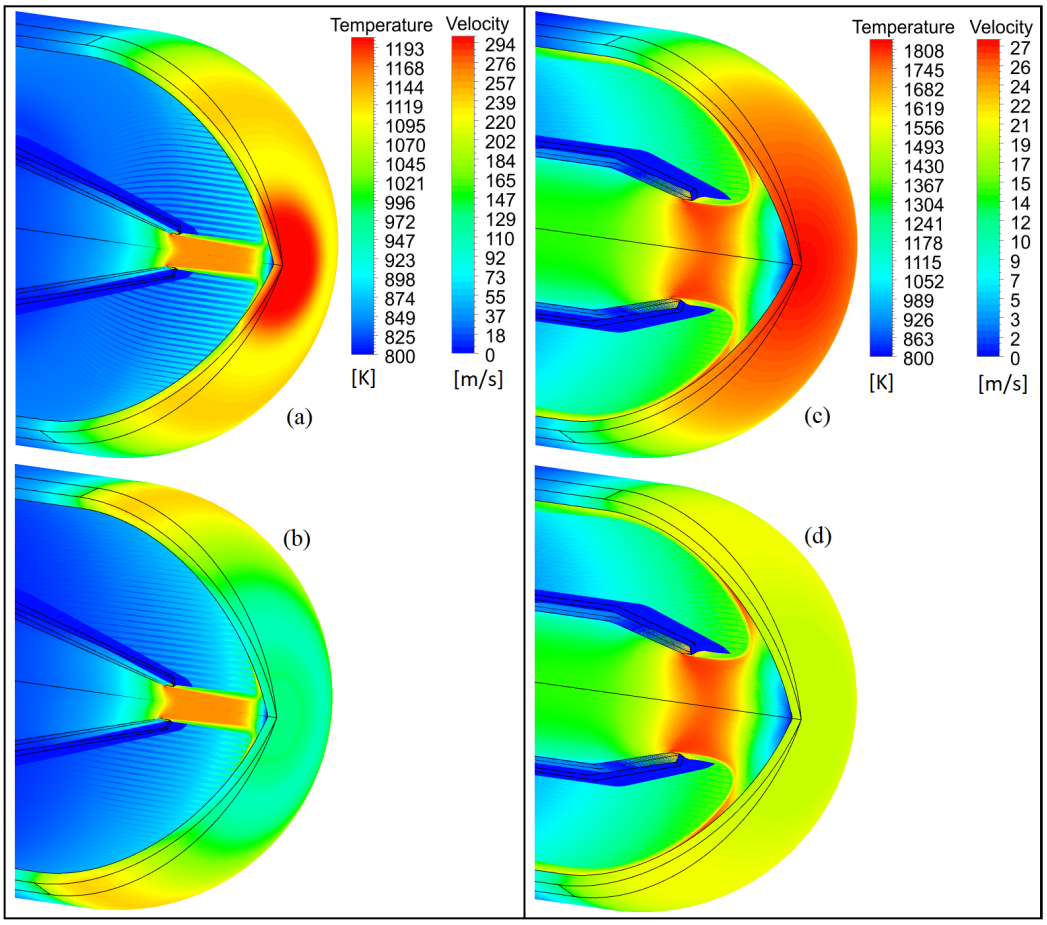

Figure 6.4: Thermocline and path lines showing the difference between the uniform flux BC and the cosine flux profile BC where: (a) $d = 6\,\text{mm}$ cosine flux profile, (b) $d = 6\,\text{mm}$ uniform flux, (c) $d = 18\,\text{mm}$ cosine flux profile, and (d) $d = 18\,\text{mm}$ uniform flux

Since the cosine flux profile, $\dot{q}''_{\text{sol}(2)}$, presents a significantly higher maximum flux, the maximum surface temperature is significantly higher than with the uniform flux, $\dot{q}''_{\text{sol}(1)}$. This reinforces the argument that a nozzle is required.

Reducing the surface temperature by including a smaller nozzle not only reduces material thermal stresses and material limitations, but also reduces external losses significantly. It is known that the reduced nozzle diameter, however, introduces large pressure drops. The trade-off between heat transfer and pressure drop is elaborated on in section 6.5. See Appendix C for more results of the local heat transfer and temperature distributions on the hemisphere.

Stellenbosch University https://scholar.sun.ac.za

6.4.2 Radiation losses

In section 6.3 the application of natural convection assumption is explained to be constant at $\eta_{nat} = 10\,\%$ for the purpose of this study[3]. The radiation losses, however, are simulated. This is done by calculating the temperature-dependant flux loss due to radiation, $\dot{q}''_{rad}$, and subtracting it from the absorbed solar flux, $\dot{q}''_{sol}$, (see Appendix A.4).

The CFD simulation solves the energy equation. Without radiation losses applied to the flux BC, the energy into the fluid is the same for all geometric design points, no matter the heat transfer coefficient, h_{avg}. In this case, it is expected that $T_{out,tip}$ and hence η_{rec} are constant across all geometric design points. This is evident in Figure 6.5 where the η_{rec} results, without radiation losses, are constant at 90 % (10 % lost to natural convection), and the η_{rec} results with radiation losses decrease with increasing nozzle diameters, because of the increasing average surface temperature $T_{avg,s}$.

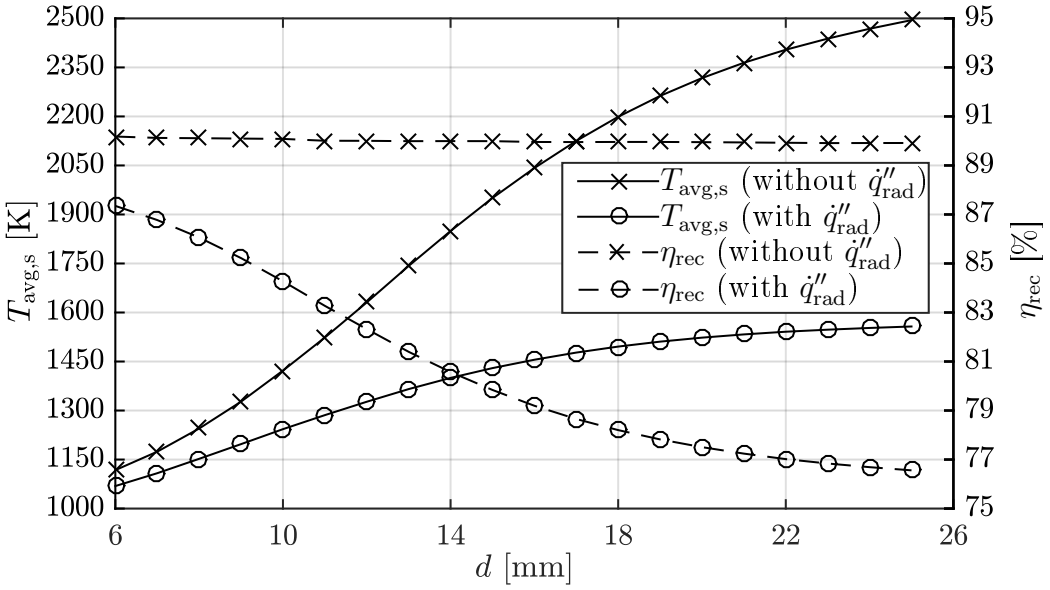

Figure 6.5: $T_{avg,s}$ and η_{rec} vs. d showing the significance of considering radiation losses, where $L = 12\,\text{mm}$

The assumption of $\eta_{nat} = 10\,\%$ originates in the reference design by Lubkoll (2017), where $d = 10\,\text{mm}$ and the resulting $\eta_{rec} = 85.2\,\%$. The natural convective losses are surface temperature-dependant and would therefore vary with different nozzle diameters, but given the result of Lubkoll (2017) as an assumption, a comparison is made between the current study and the study by Lubkoll (2017). The result of the current study is $\eta_{rec} = 84.3\,\%$ while the result by Lubkoll (2017) is $\eta_{rec} = 85.2\,\%$, revealing good thermal correlation.

[3]Note that natural convection is temperature-dependant and since surface temperatures change with different design points, the natural convective losses would also be expected to change with different design points

Stellenbosch University https://scholar.sun.ac.za

Using a UDF as the flux profile of the BC presents the capability to implement natural and forced convection terms as losses to the flux profile. This is recommended for future work.

6.4.3 Flux profile shape

Referring to Figure 5.10 in section 5.5, $\dot{q}''_{\text{sol}(2)}$, $\dot{q}''_{\text{sol}(3)}$, and $\dot{q}''_{\text{sol}(4)}$ have the same area-weighted averages, and are applied to observe the effect of the flux profile shape on the heat transfer performance. The cosine flux profile, $\dot{q}''_{\text{sol}(2)}$, is the reference point. With a lower maximum at the stagnation point, $\dot{q}''_{\text{sol}(3)}$, the quadratic function, makes up for the lower maximum in the wall jet region. The power function with an exponent of 1.5, $\dot{q}''_{\text{sol}(4)}$, has the highest maximum flux.

Comparing the results of h_{avg}, Δp, $T_{\text{avg,s}}$, $T_{\text{out,tip}}$, and η_{rec} for all three profiles across all geometric design points, there is a negligible difference between them. The most significant difference is the maximum surface temperatures, $T_{\text{max,s}}$, in the stagnation region. This region, however, contributes to a small portion of the area-weighted average, and therefore the sensitivity to the shape of the flux profile (given the same averages) is considered to be negligible.

6.4.4 Varying area-weighted average

During the course of a day, the DNI varies significantly. Two additional flux profiles are used to study the sensitivity of spike tip jet impingement heat transfer to transient solar conditions. The two profiles, $\dot{q}''_{\text{sol}(5)}$ and $\dot{q}''_{\text{sol}(6)}$, are approximately 80 % and 60 % respectively of $\dot{q}''_{\text{sol}(2)}$.

Figure 6.6 shows the average surface temperature, $T_{\text{avg,s}}$, and receiver thermal efficiency, η_{rec}, for various nozzle diameters, d. It is interesting to observe that the receiver efficiency is better for smaller nozzle diameters and larger heat flux, while larger nozzle diameters result in reduced efficiency for large diameters.

There are two sensitivities noticed that contribute to the efficiency. One is the temperature difference contributing to radiation losses. The other is the temperature difference contributing to jet impingement heat transfer. In the radiation loss term, a higher temperature difference reduces efficiency, while in the jet impingement heat transfer term, a higher temperature difference increases efficiency.

Since the surface temperature has a quartic contribution in the radiation term, its contribution to an efficiency reduction increases significantly with increasing nozzle diameters. From a design optimisation point of view, to always achieve maximum efficiency, a nozzle with control capabilities to continuously change its diameter would be necessary. This, however, would be expensive, impractical, and the percentage gain would be insignificant. Similar efficiencies are obtained for all flux magnitudes for a 12 mm nozzle.

Stellenbosch University https://scholar.sun.ac.za

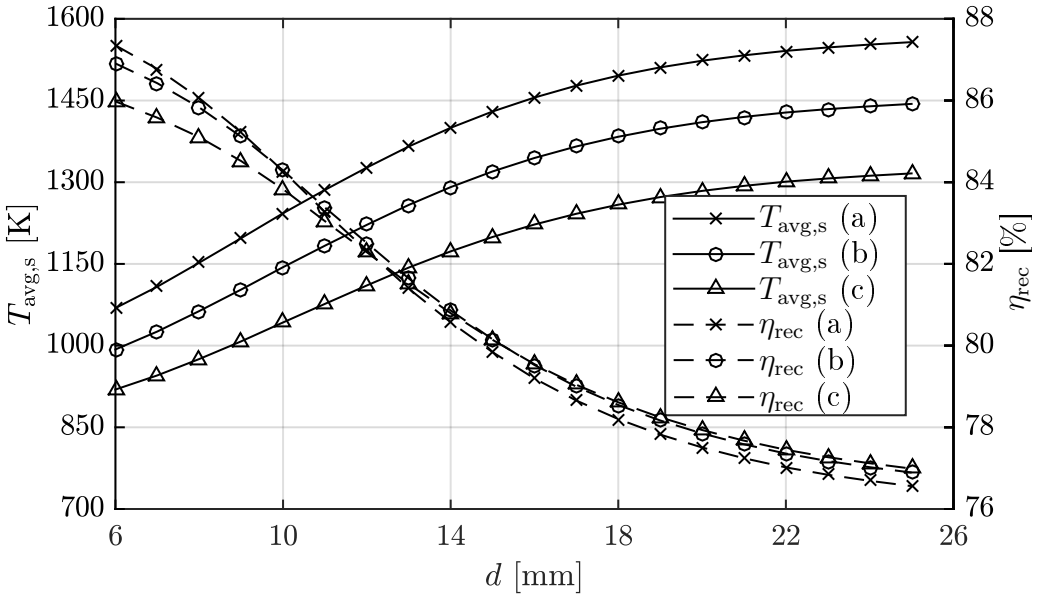

Figure 6.6: $T_{\text{avg,s}}$ and η_{rec} vs. d showing the results for different energy inputs where $L = 12\,\text{mm}$ with a flux BC of (a) $\dot{q}''_{\text{sol}(2)} - \dot{q}''_{\text{rad}}$, (b) $\dot{q}''_{\text{sol}(5)} - \dot{q}''_{\text{rad}}$, and (c) $\dot{q}''_{\text{sol}(6)} - \dot{q}''_{\text{rad}}$

6.5 Cycle efficiency tool

As previously discussed, the thermal efficiency of the receiver is not a quantification of the performance of the design. The pressure drop is not considered in η_{rec}. To incorporate the pressure drop into a performance quantification of the receiver, the Brayton cycle efficiency should be considered, with the inclusion of the pressure drop across the receiver.

A calculation method is suggested as a tool that can be used to quantify the performance of a pressurised air receiver that is used as a pre-heater in a gas turbine Brayton cycle. The components of the system and the numbering convention for the fluid pathway are shown in Figure 6.7.

The typical equations for calculating a gas turbine cycle efficiency are used, with modifications made to accommodate for the pressure drop between the compressor and turbine, as well as the thermal input of the receiver. Calculations are based on the design point performance calculation method presented by Saravanamuttoo *et al.* (2001).

The following assumptions are made in addition to those presented in section 5.2.1:

- Isentropic compressor efficiency, $\eta_{\text{c}} = 85\,\%$
- Isentropic turbine efficiency, $\eta_{\text{t}} = 87\,\%$
- Shaft mechanical efficiency, $\eta_{\text{m}} = 99\,\%$
- Combustion efficiency, $\eta_{\text{b}} = 98\,\%$
- Combustion chamber pressure drop, $\Delta p_{\text{b}} = 6\,\text{kPa}$
- Ambient temperature, $T_{\text{a}} = T_{01} = 288\,\text{K}$
- Sky temperature, $T_{\text{sky}} = 280\,\text{K}$

Stellenbosch University https://scholar.sun.ac.za

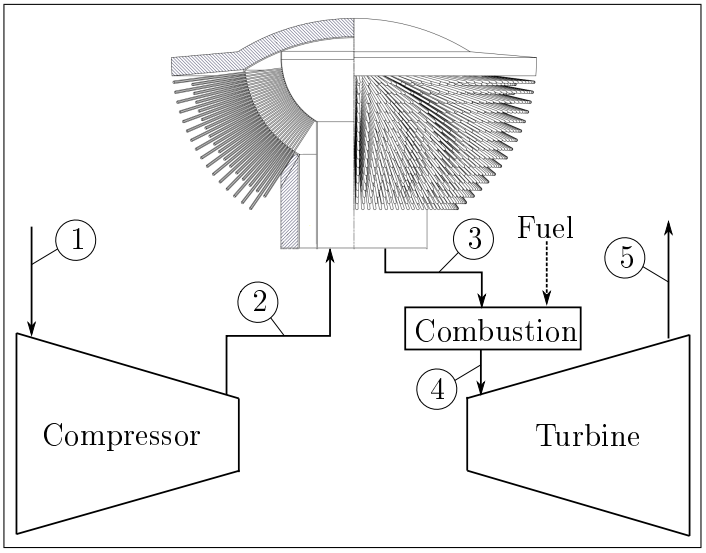

Figure 6.7: Flow diagram showing the different points in the hybrid CSP/gas Brayton cycle

- Ambient pressure, $p_a = p_{01} = p_{05} = 1\,\text{bar}$
- Receiver pressure drop, $\Delta p_{rec} = \Delta p_{rec,tip} + \Delta p_{rec,sp}$ ($\Delta p_{rec,sp} = 2\,\text{kPa}$)
- Maximum allowable pressure drop, $\Delta p_{rec} + \Delta p_b = 30\,\text{kPa}$ (Grange *et al.*, 2011; Uhlig *et al.*, 2014)
- Maximum allowable surface temperature, $T_s \leq 1500\,\text{K}$ (SMC, 2007)
- Heat capacity ratio of air, $\gamma_f = 1.4$ for air, and $\gamma_g = 1.333$ for gas
- Turbine inlet temperature, $T_{04} = 1300\,\text{K}$

With a pressure ratio of 10 and $p_{01} = 1\,\text{bar}$, it follows that $p_{02} = 10\,\text{bar}$. The first step in the process is to calculate the outlet temperature of the compressor, T_{02}, as in equation 6.7. This is also the receiver inlet temperature and it is used to calculate the compressor work, w_{tc}, with equation 6.8. Air and gas specific heats, c_p, are calculated at local temperatures.

$$T_{02} = T_a + \frac{T_a}{\eta_c}\left[\left(\frac{p_{02}}{p_{01}}\right)^{(\gamma_f-1)/\gamma_f} - 1\right] \tag{6.7}$$

$$w_{tc} = \frac{c_{p,01}\,(T_{02} - T_{01})}{\eta_m} \tag{6.8}$$

The conditions at point (3) after the SCRAP receiver are dependant on the receiver's thermal efficiency, η_{rec} (see section 6.3), and its pressure drop, Δp_{rec}. The receiver outlet temperature, T_{03}, can be calculated with the thermal efficiency, as in equation 6.9, where $q_{sol} = \dot{Q}_{sol}/\dot{m}$ is the solar thermal energy input per unit mass flow. The receiver outlet pressure, $p_{03} = p_{02} - \Delta p_{rec}$, where Δp_{rec} is the summation of $\Delta p_{rec,tip}$ and $\Delta p_{rec,sp}$. The assumption is made that $\Delta p_{rec,sp} \approx 2\,\text{kPa}$ (Lubkoll, 2017) and the majority of the receiver pressure drop is in the spike tip ($\Delta p_{rec,tip}$) due to the nozzle, and is an output of the simulations.

$$T_{03} = T_{02} + \frac{q_{sol}\eta_{rec}}{c_{p,02}} \tag{6.9}$$

Stellenbosch University https://scholar.sun.ac.za

The receiver is designed to be a pre-heater to reduce fuel consumption and hence carbon emissions. To get to the required turbine inlet temperature, the pre-heated air from the receiver is combusted with fuel, adding the energy required for the design point of the turbo machinery. The temperature rise $(T_{04} - T_{03})$ and the combustion chamber inlet temperature are used to determine the required fuel/air ratio f from Figure 2.17 of Saravanamuttoo *et al.* (2001).

The fuel in this example is a liquid hydrocarbon with a reference enthalpy of reaction per unit mass of $\Delta H_{25} = 43\,100\,\text{kJ/kg}$. Any type of fuel can be implemented with this analysis tool, as relevant to the combustion chamber in question. The specific fuel consumption can be calculated as $SFC = f/(w_\text{t} - w_\text{tc})$.

An inefficient receiver has a lower outlet temperature, T_{03}, in which case more fuel can be used to reach the required turbine inlet temperature, $T_{04} = 1300\,\text{K}$. The combustion chamber outlet pressure is $p_{04} = p_{03} - \Delta p_\text{b}$. The pressure ratio across the turbine affects its power output. An increased pressure drop in the receiver causes a decreased turbine power, which can trip the entire gas turbine if the pressure drop goes beyond the turbine's allowable limit ($\leq 30\,\text{kPa}$). The specific work transferred to the generator, $w_\text{net} = w_\text{t} - w_\text{tc}$, where w_t and T_{05} are calculated with equation 6.10 and 6.11 respectively.

$$w_\text{t} = c_{\text{p,g}}(T_{04} - T_{05}) \tag{6.10}$$

$$T_{05} = T_{04} - \eta_\text{t}\left[1 - \left(\frac{p_{04}}{p_{03}}^{(\gamma_\text{g}-1)/\gamma_\text{g}} - 1\right)\right] \tag{6.11}$$

Now that the pressure and temperature information is available for all five points in the cycle, the cycle can be analysed. Brayton cycle efficiency is typically calculated as $\eta_\text{th} = w_\text{net}/q_\text{in}$. In this case $w_\text{net} = w_\text{t} - w_\text{tc}$ and $q_\text{in} = q_\text{sol} + q_\text{b}$, where $q_\text{b} = c_{\text{p,g}}(T_{04} - T_{03})$.

This efficiency calculation method is applicable to hybrid solarised Brayton cycles, and can be used to quantify the performance of a receiver such as the SCRAP receiver for design improvement. Some of the outputs resulting from the parametric analysis are shown in Figure 6.8 and Figure 6.9.

The pressure drop limitation of the turbo machinery, assumed to be 30 kPa, is achieved by the spike tip jet impingement pressure drop, $\Delta p_\text{rec,tip}$, and the pressure drop assumptions for $\Delta p_\text{rec,sp}$ and Δp_b being 2 kPa and 6 kPa respectively. This leaves a remainder of an allowable pressure drop of 22 kPa for $\Delta p_\text{rec,tip}$. This limitation is depicted in Figure 6.8 and Figure 6.9. The material temperature limitation of 1500 K is also depicted in Figure 6.8 with symbols for the allowable design points filled in Figure 6.9.

The amount of fuel required to achieve the turbine inlet temperature depends on the receiver outlet temperature which, in turn, depends on the receiver efficiency and the receiver thermal energy input. The higher the receiver outlet temperature, T_{03}, the less fuel is required to reach T_{04}. Specific fuel consumption (SFC) is related to the net specific work, w_net, which explains

Stellenbosch University https://scholar.sun.ac.za

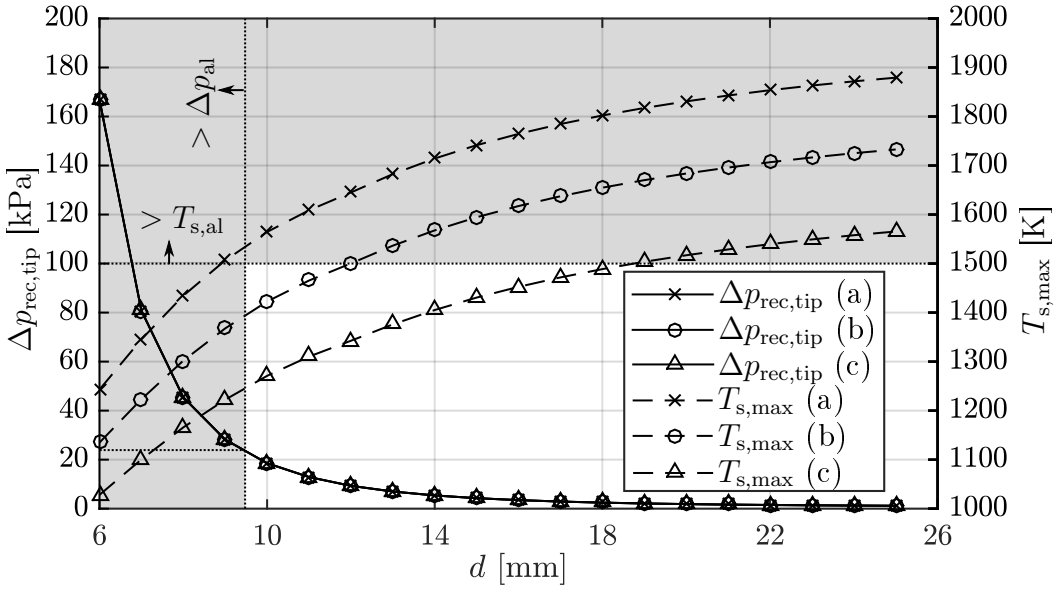

Figure 6.8: $T_{\text{avg,s}}$ and η_{rec} vs. d showing the results for different energy inputs where $L = 12\,\text{mm}$ with a flux BC of (a) $\dot{q}''_{\text{sol(2)}} - \dot{q}''_{\text{rad}}$, (b) $\dot{q}''_{\text{sol(5)}} - \dot{q}''_{\text{rad}}$, and (c) $\dot{q}''_{\text{sol(6)}} - \dot{q}''_{\text{rad}}$

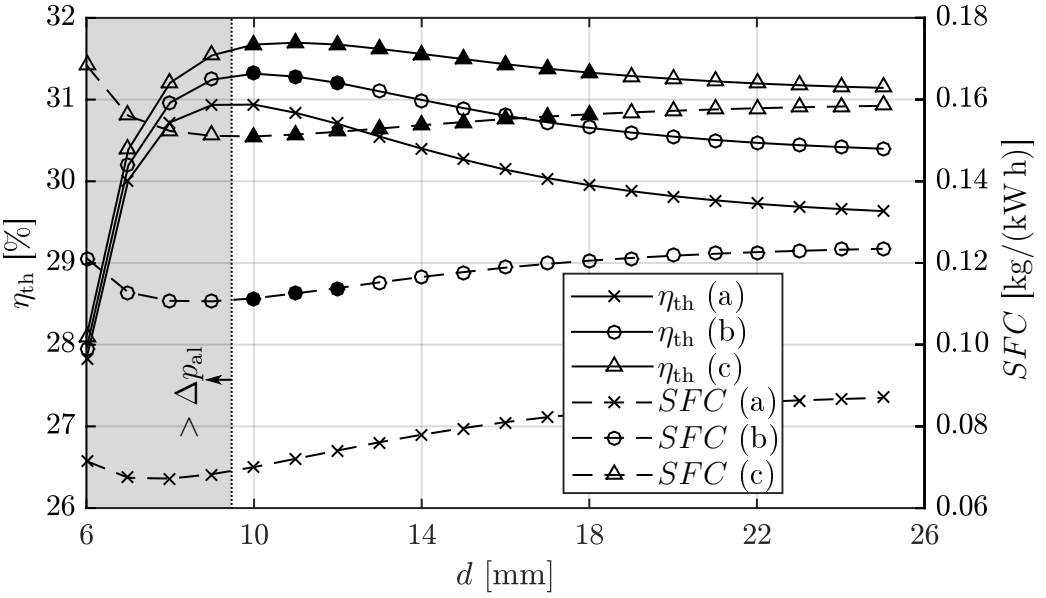

Figure 6.9: $T_{\text{avg,s}}$ and η_{rec} vs. d showing the results for different energy inputs where $L = 12\,\text{mm}$ with a flux BC of (a) $\dot{q}''_{\text{sol(2)}} - \dot{q}''_{\text{rad}}$, (b) $\dot{q}''_{\text{sol(5)}} - \dot{q}''_{\text{rad}}$, and (c) $\dot{q}''_{\text{sol(6)}} - \dot{q}''_{\text{rad}}$

Stellenbosch University https://scholar.sun.ac.za

the sudden increase in fuel consumption for very small nozzles caused by the excessive pressure drop.

In Figure 6.9, the increasing cycle efficiency, η_{th}, with decreasing solar thermal input can be explained by the decrease in surface temperatures, which implies less thermal losses. When solar flux is low (morning or afternoon), the receiver surface temperature and hence thermal losses will be lower, but this comes at the cost of increased fuel consumption.

6.6 Conclusion

In terms of the two geometric parameters studied, significant sensitivities to pressure drop and heat transfer are evident with the nozzle diameter, d, while negligible differences are observed for the nozzle-to-surface distance parameter, L.

Several flux profiles are studied, with the implementation of radiation losses as a temperature-dependant loss in the flux BC as a UDF. This mechanism can also be used to implement other temperature-dependant losses, such as natural and forced convective losses to ambient. Flux profiles with three different DNI magnitudes are compared, to predict the sensitivity of the performance of the receiver at different times of day.

A method of quantifying the thermal efficiency of the receiver is presented, as well as a tool that can be used to calculate the cycle efficiency and fuel consumption of hybrid solarised Brayton cycles.

Since there are so many unknowns with so many assumptions, the actual efficiency values may not be realistic, but the principles underpinning the calculation are presented, and the sensitivities of the geometric and solar thermal input parameters are evident. The cycle efficiency calculation for this solarised gas turbine cycle could prove to be a useful tool, with the possibility of large-scale commercialisation of solarised gas turbines. It could also be modified for use in supercritical carbon dioxide cycles.

The author has presented the results of the parametric analysis and successfully developed a numerical model to calculate the efficiency of a hybrid solarised Brayton cycle. Given the assumptions made and the parametric limitations, none of the design points were within the maximum allowable temperature or pressure ranges, where a maximum concentrated solar flux of $\dot{q}''_{\text{max}} = 1.265\,\text{MW/m}^2$ is experienced. Natural convective losses would reduce this temperature had they been implemented in the model. The reduced flux intensity profiles present design points within the allowable ranges.

Working too close to the turbo machinery limitations can be risky, and working at temperatures close to the material limitations can also be risky. For design point selection, it is recommended that a safety factor be introduced. With the input parameters and assumptions made in this study, a maximum cycle efficiency is achieved for $10\,\text{mm} \leq d \leq 12\,\text{mm}$.

Stellenbosch University https://scholar.sun.ac.za

Chapter 7

Conclusion

In this work, a detailed analysis on the local effects that the jet impingement cooling mechanism offers to the SCRAP receiver is presented. A CFD model for the complex flow field is developed and validated. An initial parametric analysis presents the design sensitivity to various parameters, and a method of quantifying the receiver performance is presented. Some recommendations for further work are also presented in this chapter.

7.1 Contribution

The intention and objective of this study was to develop a CFD model that can be used to analyse the localised effects of the spike tip jet impingement heat transfer in the SCRAP receiver. The findings suggest that the objectives were met, presenting the model validation process and the application of the developed model to the SCRAP receiver.

Chapter 3 and chapter 4 present the development of the CFD model that is validated against the experimental work of Lee *et al.* (1999). Here, the flow phenomena and heat transfer characteristics of jet impingement on a concave hemisphere are analysed. Numerical replication of the large set of experimental results from literature is performed, resulting in relatively good correlation, particularly in the geometric and flow characteristic range of relevance to the SCRAP design point.

With a 2-d axisymmetric numerical environment, relatively low computational resources are required for each simulation. This permitted the author to run multiple simulations in a relatively short amount of time. With the elevated computational power of the HPC, the capability of running several simulations simultaneously presented the opportunity to perform the validation of all 27 published experimental design points of Lee *et al.* (1999). It is noted by the author that the 2-d environment assumes axisymmetry which is of course not the case. It is reasonably assumed, for the scope of this study, that the azimuthal turbulence is insignificant, but this should not be ignored in follow-up work.

Through an extensive sensitivity study in the validation process, it was found that there are two environmental factors to the experiments that are

Stellenbosch University https://scholar.sun.ac.za

not published by Lee *et al.* (1999). The numerical model is highly sensitive to these two factors, namely, the pipe exit turbulence conditions and the outflow surrounding geometry. The pipe exit turbulence has a significant effect on the heat transfer in the stagnation region, and the outflow surrounding geometry determines the amount of flow re-circulation, which can significantly affect the wall jet heat transfer. It was shown that the results of the two extremes of the amount of re-circulation fall above and below the experimental profiles. It is therefore assumed that, given the missing information about the experimental conditions, improved matching would have been attempted with a high expectation of improved results.

The validation study concludes that the k-ω SST turbulence model, with the intermittency transition extension, is the preferred RANS turbulence model for the application of jet impingement on a concave hemisphere.

With the gained insight from the validation study, the SCRAP receiver spike tip is numerically modelled. Good h_{avg} correlation is achieved with the high level CFD performed by Lubkoll (2017), but the local heat transfer profiles differ. This study presents an improved prediction of the Nu profile that captures the local effects more accurately. These local effects are important, due to the significant range of the incoming flux profile on the spike tip.

The sensitivity of three geometric parameters (nozzle slope angle, α, nozzle-to-surface distance, L, and nozzle diameter, d) were studied. It was found that a slope angle of $\alpha \leq 15^{\circ}$ was sufficient for reduced pressure drop. The heat transfer and pressure drop was not significantly sensitive to the nozzle-to-surface distance, L, while it was noted that placing the nozzle too close to the impingement surface throttles the flow, inducing a large pressure drop.

A parametric analysis of 540 design points, including three nozzle-to-surface distances, 20 nozzle diameters, and nine solar flux profiles was performed, resulting in a more in-depth understanding of the design sensitivities. With the inclusion of surface temperature dependant radiation losses in the flux boundary condition, an analysis was done on the performance of the receiver and the effects of radiation losses were reported on.

The most sensitive design parameter is the nozzle diameter, d. The nozzle's purpose is to accelerate the flow as a jet, which, in turn, impinges on the inner surface of the end cap with enhanced heat transfer. This, however, has a significant pressure drop implication due to the sudden expansion of the fluid exiting the nozzle. The introduction of a nozzle presents this trade-off between heat transfer and pressure drop. Two system constraints are the maximum allowable pressure drop for the turbo machinery, and the maximum allowable temperature of the receiver metallic material.

Quantifying the receiver performance is not as simple as calculating the thermal efficiency of the receiver, because the pressure drop has a significant effect on the operation and efficiency of the turbo machinery in the system. A method of quantifying the cycle performance is therefore developed as a tool that can be used for further research on similar solarised gas turbine systems. This study concluded that the maximum cycle efficiency achieved in

Stellenbosch University https://scholar.sun.ac.za

the parametric set is typically a design point in which a nozzle diameter in the range of $10\,\text{mm} \leq d \leq 12\,\text{mm}$ is used.

This work concludes the importance of the local effects of jet impingement in the spike tip including the heat transfer profile, the induced pressure drop, and the maximum material surface temperature. These three aspects are critical output parameters to consider when designing the spike tip geometry, mass flow rate and solar flux. The insight presented in this thesis will aid further development of the SCRAP receiver and help solve other thermo-fluid problems of a similar nature.

7.2 Recommendations

A number of recommendations are presented for each of the two main parts of this study, the CDF model validation and the application of the model.

7.2.1 Further CFD validation

Building a lab-based experimental setup to perform experiments aimed at improving the validation of the model and improving our understanding of jet impingement in the context of the SCRAP spike tip is recommended. Such an experimental setup has the potential to produce novel findings in the jet impingement field, since few publications exist on concave hemispherical jet impingement.

Included in such experiments should be a measurement of the nozzle/pipe exit flow conditions (velocity and turbulence profiles can be obtained using hot wire anemometer technology), the amount of re-circulated flow, and local heat transfer properties in the hemisphere.

The challenge with a closed spike geometry is the measurement of the heat transfer. Being able to do this would permit further investigation into the validity of the k-ω SST turbulence model, with the intermittency transition extension.

In addition, it would be beneficial to observe the capabilities of the v^2f model using OpenFOAM and/or the use of a hybrid RANS/LES model (see Kubacki and Dick (2009, 2010, 2011)).

7.2.2 Further work on the SCRAP receiver

Further investigation on single segments (such as spike tip, channel flow swirling, external interaction with ambient, and structural integrity) of the receiver can continue to be developed, but it is also recommended that a study be conducted on the combining of the results of these component-level analyses in a 3-d CFD model of the entire receiver, or a cluster of spikes. This study should include the local effects and external losses (natural and forced convective losses as well as radiation losses). A systems analysis studying the practical implications of implementing this receiver into an actual combined cycle power plant is also recommended.

Stellenbosch University https://scholar.sun.ac.za

Further, given the necessary funding, building a prototype cluster of spikes to be placed at the top of a CSP tower is recommended to analyse the heat transfer and pressure drop response experimentally from empirical data.

There are several geometric alterations that can be considered in the spike tip. Extending the fins into the spike tip could increase heat transfer, not only by convection, but also by conduction from the maximum flux at the hemisphere's centre. The spike tip's trade-off of heat transfer and pressure drop lends itself ideally to a topology optimisation problem. In a topology optimisation study, the objective would be to maximise the Brayton cycle efficiency with constraints on the pressure drop and maximum material temperature. The geometry of the nozzle and surrounding spike tip region, could be altered to influence the jet flow characteristics, as well as upstream and downstream flow fields, ultimately attempting to decrease pressure drop and increase heat transfer to an optimal ratio that maximises cycle efficiency.

Inducing turbulence into the jet has been shown, by Craig (2018), to drastically increase heat transfer, but typically also increase pressure drop. Craig (2018) investigates this for a molten salt CSP receiver. This could also be investigated for SCRAP. Introducing a swirl into the jet flow could result in a performance enhancement.

A detailed ray-tracing analysis would give insight into more detailed local spike tip flux mapping. The current study shows the importance of the flux profile and local heat transfer. Therefore, a detailed ray-tracing and flux mapping study is recommended.

Since turbo-machinery is sensitive to off-design conditions (i.e. they are designed to work at specified flow rates, temperatures, and pressure ratios), solarised gas turbines are typically supplemented with the combustion of fuel to reach design conditions. There is work being done on de-coupling the compressor and turbine to permit continuous variability in the operating conditions for CSP gas turbines that experience varying solar input. For this reason, it is recommended that a study be done for transient solar and turbo machinery conditions for the SCRAP receiver.

Stellenbosch University https://scholar.sun.ac.za

Appendices

Stellenbosch University https://scholar.sun.ac.za

Appendix A

HPC automation

A.1 Job submission command (HPC interaction)

The following code is presented as an example of an interaction with the Stellenbosch University HPC. The code is essentially identical for any simulation except for the simulation name, "L4_d3_50", and the journal file that is the input commands, "L4_d3_50.jou", for which examples are shown below in section A.2 and section A.3.

```
#!/bin/bash
#PBS -N L4_d3_50
#PBS -l select=1:ncpus=16:mpiprocs=16:mem=32GB:scratch=true
#PBS -l walltime=8:00:00
#PBS -m be
#PBS -e L4_d3_50.err
#PBS -o L4_d3_50.out

INPUT=L4_d3_50.jou

# make sure Im the only one that can read my output
umask 0077
TMP=/scratch-small-local/${PBS_JOBID}
mkdir -p ${TMP}

if [ ! -d "${TMP}" ]; then
echo "Cannot create temporary directory. Disk probably full."
exit 1
fi

# copy the input files to ${TMP}
echo "Copying from ${PBS_O_WORKDIR}/ to ${TMP}/"
/usr/bin/rsync -vax "${PBS_O_WORKDIR}"/ ${TMP}/
```

Stellenbosch University https://scholar.sun.ac.za


```
cd ${TMP}

# choose version of FLUENT
module load app/ansys/17.2

# Automatically calculate the number of processors
np=$(wc -l < ${PBS_NODEFILE})

fluent 2ddp -pdefault -cnf=${PBS_NODEFILE} -mpi=intel -g -t${np}
-ssh -i ${INPUT}

# job done, copy everything back
echo "Copying from ${TMP}/ to ${PBS_O_WORKDIR}/"
/usr/bin/rsync -vax ${TMP}/ "${PBS_O_WORKDIR}/"

# delete my temporary files
[ $? -eq 0 ] && /bin/rm -rf ${TMP}
```

A.2 Fluent TUI commands for validation simulations

The below shown code is an example of the Fluent TUI commands used for one of the validation simulations. With these commands, there is no graphical interaction with Fluent. The mesh is generated in the Workbench environment and exported as a ".msh" file and then imported using the TUI commands. The rest of the code changes settings and defines the numerical setup.

```
rc "L4_d3_stepout.msh"
define models axisymmetric yes
define bc zt 8 axis
/mesh/repair/allow-repair-at-boundaries yes
/mesh/repair-improve/repair
define models energy yes no no no yes
define models viscous kw-sst yes
define models viscous turbulence-expert kato-launder-model? yes
define models viscous turbulence-expert production-limiter? yes
10
define models viscous add-intermittency-transition-model? yes no
define materials change-create air air yes piecewise-linear 26
150 2.355 200 1.767 250 1.413 260 1.360 270 1.311 280 1.265 290
1.220 300 1.177 310 1.141 320 1.106 330 1.073 340 1.042 350
1.012 360 0.983 370 0.956 380 0.931 390 0.906 400 0.883 500
0.706 600 0.589 700 0.507 800 0.442 900 0.392 1000 0.354 1500
0.235 2000 0.176 yes piecewise-linear 26 150 1017 200 1009 250
1009 260 1009 270 1009 280 1008 290 1007 300 1005 310 1005 320
1006 330 1006 340 1007 350 1007 360 1007 370 1008 380 1008 390
```

Stellenbosch University https://scholar.sun.ac.za


```
1009 400 1009 500 1017 600 1038 700 1065 800 1089 900 1111 1000
1130 1500 1202 2000 1244 yes piecewise-linear 26 150 0.0158 200
0.0197 250 0.0235 260 0.0242 270 0.0249 280 0.0255 290 0.0261
300 0.0267 310 0.0274 320 0.0281 330 0.0287 340 0.0294 350 0.03
360 0.0306 370 0.0313 380 0.0319 390 0.0325 400 0.0331 500
0.0389 600 0.0447 700 0.0503 800 0.0559 900 0.0616 1000 0.0672
1500 0.0926 2000 0.1149 yes piecewise-linear 26 150 10.64e-6
200 13.59e-6 250 16.14e-6 260 16.63e-6 270 17.12e-6 280 17.6e-6
290 18.02e-6 300 18.43e-6 310 18.87e-6 320 19.29e-6 330
19.71e-6 340 20.13e-6 350 20.54e-6 360 20.94e-6 370 21.34e-6
380 21.75e-6 390 22.12e-6 400 22.52e-6 500 26.33e-6 600
29.74e-6 700 33.03e-6 800 35.89e-6 900 38.65e-6 1000 41.52e-6
1500 53.82e-6 2000 64.77e-6 no no no
file read-profile d3_50.prof
define bc velocity-inlet inlet no no yes yes yes no "d58"
"axial-velocity" no 0 no 286.15 yes yes no "d58"
"intermittency" yes no "d58" "turb-kinetic-energy" yes no "d58"
"specific-diss-rate"
define bc pressure-outlet outlet no yes no 0 no 286.15 no no yes
no no yes no 1 1 5 no no
define bc wall wall_dome 0 no 0 no no no 45.86 no no no 0 no 0.5
no 1
report reference-values compute velocity-inlet inlet
report reference-values length 0.034
solve set p-v-coupling 24
solve set gradient-scheme no no
solve set high-order-term-relaxation enable yes
solve set discretization-scheme pressure 10
solve set discretization-scheme k 1
solve set discretization-scheme omega 1
solve monitors residual convergence-criteria 1e-6 1e-6 1e-6
1e-12 1e-6 1e-6 1e-6 1e-6
solve initialize repair-wall-distance yes
solve initialize hyb-initialization
it 10000
define custom-field-functions define "h"
"heat_flux/(temperature-286.15)"
define custom-field-functions define "nu"
"heat_flux*0.034/(0.025869015*(temperature-286.15))"
plot plot yes Nu_dome yes no no nusselt-number no no
y-coordinate wall_dome ()
plot plot yes Nu_dome2 yes no no nu no no y-coordinate
wall_dome ()
plot plot yes h_dome yes no no heat-transfer-coef no no
y-coordinate wall_dome ()
plot plot yes h_dome2 yes no no h no no y-coordinate
wall_dome ()
```

Stellenbosch University https://scholar.sun.ac.za


```
plot plot yes y+_dome yes no no y-plus no no y-coordinate
wall_dome ()
plot plot yes PC_dome yes no no pressure-coefficient no no
y-coordinate wall_dome ()
plot plot yes P_dome yes no no pressure no no y-coordinate
wall_dome ()
plot plot yes T_dome yes no no temperature no no y-coordinate
wall_dome ()
report surface-integrals area-weighted-avg 3 () nusselt-number
yes "Nu_av_dome"
report surface-integrals area-weighted-avg 3 ()
heat-transfer-coef yes "h_av_dome"
report surface-integrals area-weighted-avg 3 () nu yes
"Nu_new_av_dome"
report surface-integrals area-weighted-avg 3 () h yes
"h_new_av_dome"
wcd "L4_d3_50_out.cas"
```

A.3 Fluent TUI commands for application simulations

The below shown code is an example of the Fluent TUI commands used for one of the application simulations. With these commands, there is no graphical interaction with Fluent. The mesh is generated in the Workbench environment and exported as a ".msh" file and then imported using the TUI commands. The rest of the code changes settings and defines the numerical setup.

```
rc "d10_L2.msh"
define models axisymmetric yes
/mesh/repair/allow-repair-at-boundaries yes
/mesh/repair-improve/repair
define models energy yes no no no yes
define models viscous kw-sst yes
define models viscous turbulence-expert kato-launder-model? yes
define models viscous turbulence-expert production-limiter? yes 10
define models viscous add-intermittency-transition-model? yes no
define materials change-create air air yes ideal-gas yes polynomial
3 873.829345703125 0.3501025140285492 -8.256000000983477e-05 yes
polynomial 3 0.00891095120459795 6.676215707557276e-05
-7.929999767952722e-09 yes polynomial 3 7.97359552962007e-06
4.228837724440382e-08 -6.89799996636542e-12 no no no
define materials change-create aluminum inconel yes constant
8193.252 yes constant 435 yes polynomial 2 11.032 1.6031e-2 yes
file read-profile inlet_v.prof
define bc velocity-inlet inlet no no yes yes yes no "outlet_0.02"
"axial-velocity" no 0 no 700 yes no 1 yes no "outlet_0.02"
```

Stellenbosch University https://scholar.sun.ac.za


```
"turb-kinetic-energy" yes no "outlet_0.02" "specific-diss-rate"
define bc pressure-outlet outlet no yes no 882710.036 no 790 no
no yes no no no yes no 1 5 0.026 no no
define user-defined compiled-functions load "libudf3"
solve initialize hyb-initialization
define bc wall wall_dome_out 0 no 0 no no yes yes "udf"
"heat_flux_profile::libudf3" no 1
report reference-values compute velocity-inlet inlet
report reference-values length 0.01
solve set p-v-coupling 20
solve set gradient-scheme no yes
solve set high-order-term-relaxation enable yes
solve set discretization-scheme pressure 10
solve set discretization-scheme k 1
solve set discretization-scheme omega 1
solve set discretization-scheme intermit 1
solve monitors residual convergence-criteria 1e-6 1e-6 1e-6 1e-12
1e-6 1e-6 1e-6
solve initialize repair-wall-distance yes
solve initialize hyb-initialization
ok
it 1000
solve set p-v-coupling 24
it 15000
surface line-surface p_out_line -0.1 0.015 -0.1 0.033
define custom-field-functions define "h" "heat_flux/(temperature-700)"
define custom-field-functions define "nu" "heat_flux*0.01/
(0.051758757*(temperature-700))"
plot plot yes Nu_dome_in yes no no nusselt-number no no
y-coordinate wall_dome_in-shadow ()
plot plot yes y+_dome yes no no y-plus no no y-coordinate
wall_dome_in-shadow ()
plot plot yes PC_dome yes no no pressure-coefficient no no
y-coordinate wall_dome_in-shadow ()
plot plot yes P_dome yes no no pressure no no y-coordinate
wall_dome_in-shadow ()
plot plot yes T_dome_in yes no no temperature no no y-coordinate
wall_dome_in-shadow ()
plot plot yes T_dome_out yes no no temperature no no y-coordinate
wall_dome_out ()
plot plot yes h_dome_in yes no no h no no y-coordinate
wall_dome_in-shadow ()
plot plot yes Nu_dome_in2 yes no no nu no no y-coordinate
wall_dome_in-shadow ()
report surface-integrals area-weighted-avg 6 () temperature yes
"T_av_dome_out"
report surface-integrals area-weighted-avg 1 () temperature yes
```

Stellenbosch University https://scholar.sun.ac.za


```
"T_av_dome_in"
report surface-integrals area-weighted-avg 1 () nusselt-number
yes "Nu_av_dome_in"
report surface-integrals area-weighted-avg 0 () nusselt-number
yes "Nu_av_pipe_in"
report surface-integrals area-weighted-avg 1 ()
heat-transfer-coef yes "h_av_dome_in"
report surface-integrals area-weighted-avg 0 ()
heat-transfer-coef yes "h_av_pipe_in"
report surface-integrals area-weighted-avg 1 ()
nu yes "Nu_new_dome_in"
report surface-integrals area-weighted-avg 0 ()
nu yes "Nu_new_pipe_in"
report surface-integrals area-weighted-avg 1 ()
h yes "h_new_dome_in"
report surface-integrals area-weighted-avg 0 ()
h yes "h_new_pipe_in"
report surface-integrals area-weighted-avg 9 ()
pressure yes "P_av_inlet"
report surface-integrals area-weighted-avg 7 ()
pressure yes "P_av_outlet"
report surface-integrals area-weighted-avg 9 ()
total-pressure yes "P_tot_av_inlet"
report surface-integrals area-weighted-avg 14 ()
total-pressure yes "P_tot_av_line"
report surface-integrals area-weighted-avg 7 ()
total-pressure yes "P_tot_av_outlet"
report surface-integrals area-weighted-avg 7 ()
temperature yes "T_out"
report surface-integrals facet-max 6 ()
temperature yes "T_max_wall"
wcd "d10_L2_out.cas"
```

A.4 User defined flux boundary condition for $q''_{\mathrm{sol}(2)} - q''_{\mathrm{rad}}$

The below shown code is an example of a user defined function (UDF). This particular example implements the solar input flux, $q''_{\mathrm{sol}(2)}$ as a cosine function, and from that, subtracts the local temperature dependant radiation losses as q''_{rad}.

Additional terms can be added to calculate local fluid properties at the film temperature which can be used to determine other external losses such as natural and forced convection.

```
#include "udf.h"
```

Stellenbosch University https://scholar.sun.ac.za


```
DEFINE_PROFILE(heat_flux_profile,t,i)
{
real x[ND_ND];
face_t f;
real rad,y;
real Temp ;
real q_solar,q_rad ;


begin_f_loop(f,t)
{
F_CENTROID(x,f,t);

y=x[1];

Temp = F_T(f,t) ;

rad = asin(y/0.035) ;

q_solar = 0.9*(1265000-60000)*cos(rad) + 0.9*60000;
q_rad = 0.9*0.00000005670367*(pow(Temp,4)-pow(280.15,4)) ;


F_PROFILE(f,t,i)= q_solar - q_rad;
}
end_f_loop(f,t)
}
```

Stellenbosch University https://scholar.sun.ac.za

Appendix B

Flat plate impinging round jet validation

Multiple publications exist on flat plate jet impingement heat transfer. Baughn and Shimizu (1989), Yan (1993) and Lee and Lee (1999) published experimental results of Nu distributions of round jets impinging on flat plates.

With similar numerical environment inputs as described in Chapter 3, a flat plate mesh and model is developed.

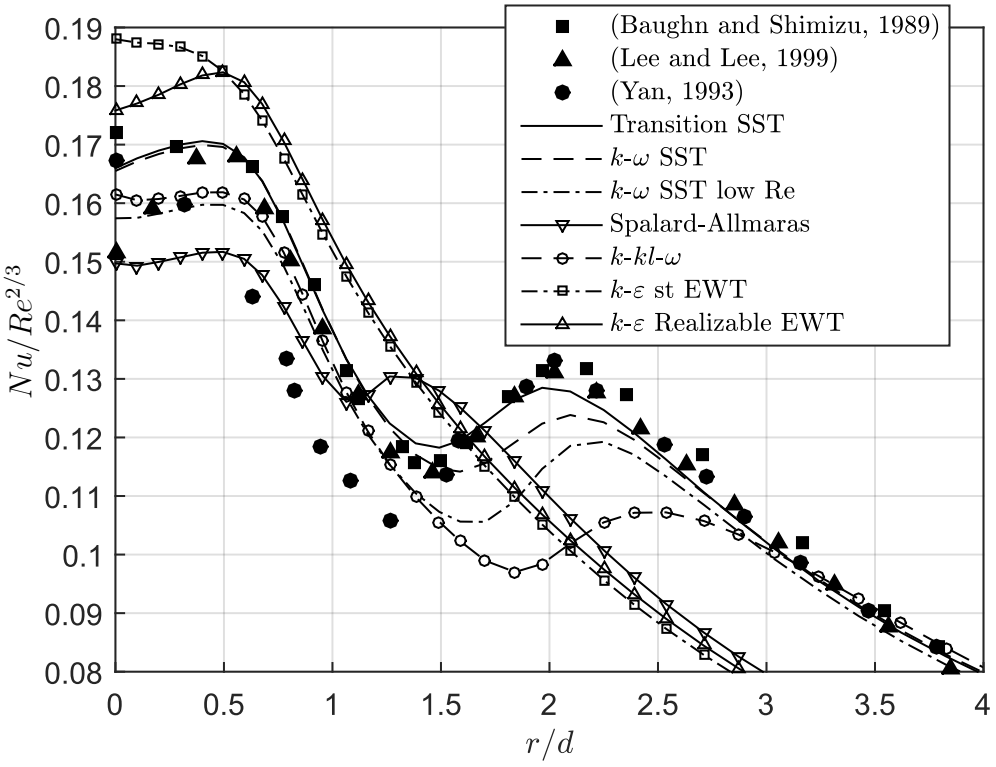

Figure B.1: Nusselt number distributions on a flat plate for model comparison

Figure B.1 and Figure B.2 show the results of the flat plate validation study. Figure B.1 shows that the Transition SST model has the best correlation with

Stellenbosch University https://scholar.sun.ac.za

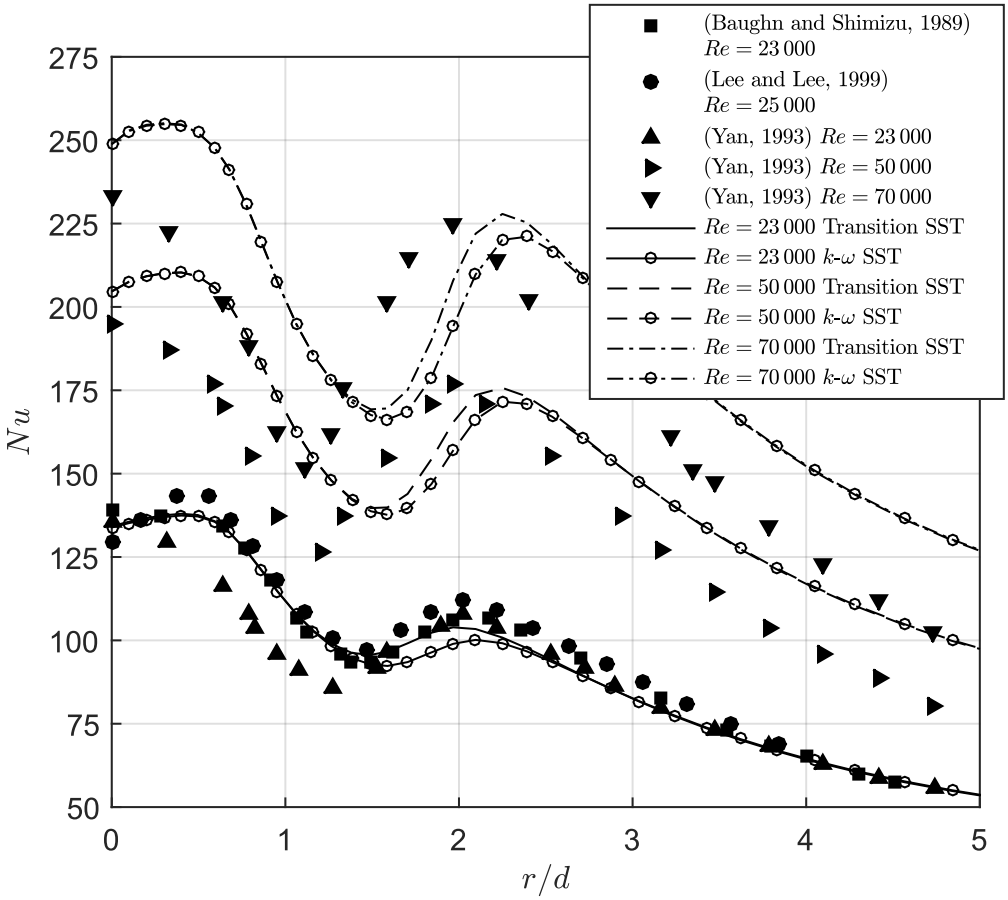

Figure B.2: Nusselt number distributions on a flat plate at different Re

experimental results with the k-ω SST model with the intermittency equation enabled performs very well as well.

Figure B.2 shows that the trend of increasing Re is predicted well with an increasing over-prediction of the stagnation region heat transfer with increasing Re. The second peak position appears to be predicted further from the stagnation point with increasing Re. This study validates the use of the k-ω SST model with the intermittency equation enabled.

Stellenbosch University https://scholar.sun.ac.za

Appendix C

Surface distribution plots

Figure C.1 shows the Nu distributions along the concave surface for different nozzle diameters using a flux profile of $\dot{q}''_{\mathrm{sol}(2)}$ and subtracting $\dot{q}''_{\mathrm{rad}}$. For the same cases, Figure C.2 shows the external surface temperature distributions for the same cases.

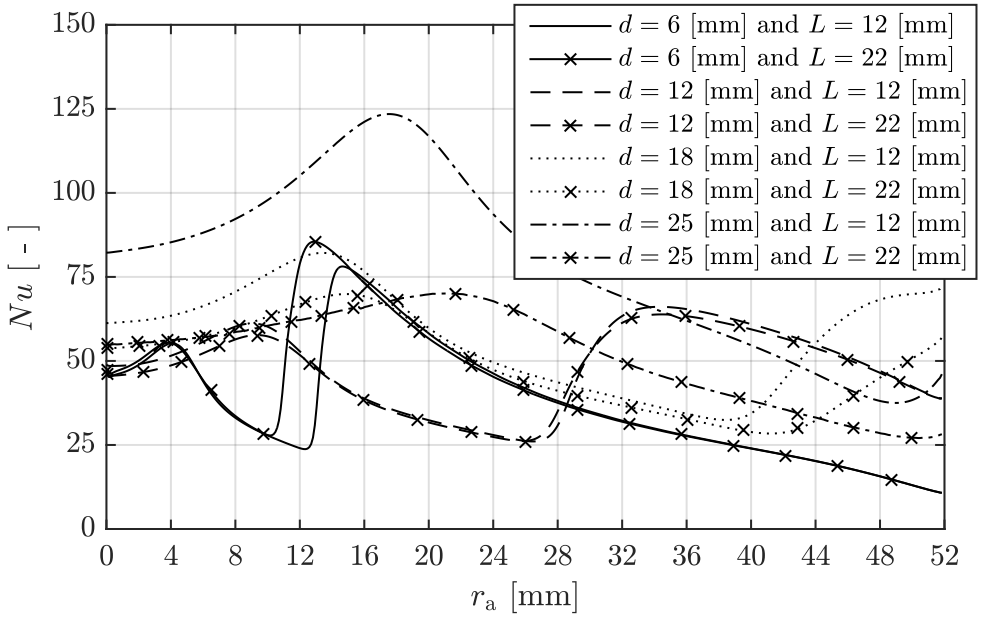

Figure C.1: Nu distributions along the concave surface of the spike tip for different nozzle diameters and nozzle-to-surface distances, using a flux profile of $\dot{q}''_{\mathrm{sol}(2)}$

These plots show the detail of the local heat transfer and temperature distribution. The most significant difference observed between $L = 12\,\mathrm{mm}$ and $L = 22\,\mathrm{mm}$ is for a nozzle diameter of $d = 25\,\mathrm{mm}$. This is because the flow is being throttled since the nozzle's edge is close to the hemisphere surface. This effect is clearly evident in Figure C.1.

Stellenbosch University https://scholar.sun.ac.za

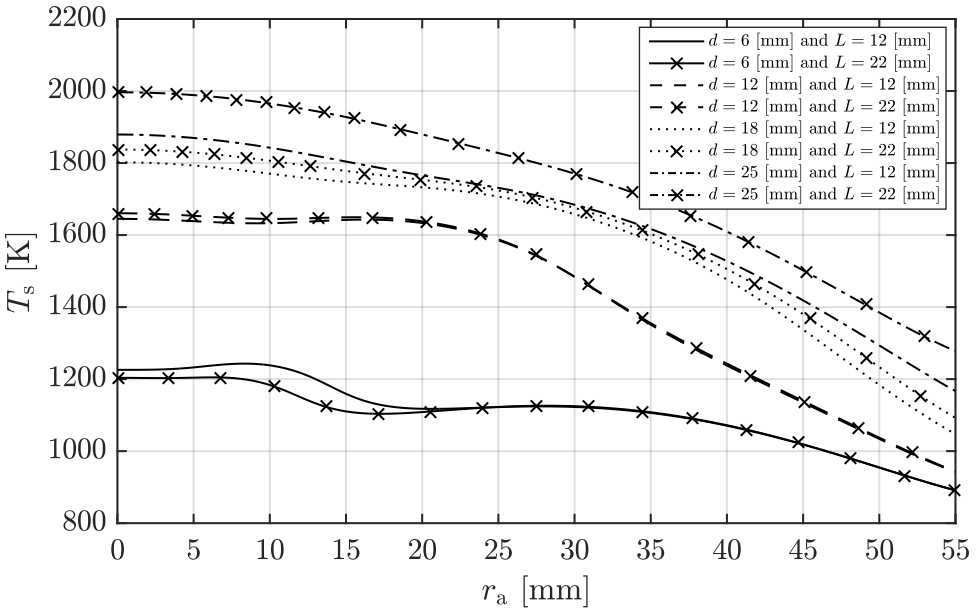

Figure C.2: Surface temperature, T_s, distributions along the external surface of the end cap for different nozzle diameters and nozzle-to-surface distances, using a flux profile of $\dot{q}''_{sol(2)}$

Stellenbosch University https://scholar.sun.ac.za

List of References

Achari, A.M. and Das, M.K. (2015). Application of various RANS based models towards predicting turbulent slot jet impingement. *International Journal of Thermal Sciences*, vol. 98, pp. 332–351.

Angioletti, M., Nino, E. and Ruocco, G. (2005). CFD turbulent modelling of jet impingement and its validation by particle image velocimetry and mass transfer measurements. *International Journal of Thermal Sciences*, vol. 44, no. 4, pp. 349–356. ISSN 12900729.

ANSYS (2016). Flow Field of a Turbulent Jet Impinging on a Heated Plate Case description. Tech. Rep., ANSYS Inc.

Augsburger, G. (2013). *Thermo-economic optimisation of large solar tower power plants*. PhD, Doctoral Thesis.

Avila-Marin, A.L. (2011). Volumetric receivers in Solar Thermal Power Plants with Central Receiver System technology: A review. *Solar Energy*, vol. 85, pp. 891–910.

Baughn, J.W. and Shimizu, S. (1989). Heat Transfer Measurements From a Surface With Uniform Heat Flux and an Impinging Jet. *Journal of Heat Transfer*, vol. 111, no. 4, pp. 1096–1098. ISSN 0022-1481.
Available at: `http://dx.doi.org/10.1115/1.3250776`

Behnia, M., Parneix, S. and Durbin, P.A. (1998). Prediction of heat transfer in an axisymmetric turbulent jet impinging on a flat plate. *International Journal of Heat and Mass Transfer*, vol. 41, no. 12, pp. 1845–1855. ISSN 00179310.

Caggese, O., Gnaegi, G., Hannema, G., Terzis, A. and Ott, P. (2013). Experimental and numerical investigation of a fully confined impingement round jet. *International Journal of Heat and Mass Transfer*, vol. 65, pp. 873–882.
Available at: `https://www-sciencedirect-com.ez.sun.ac.za/science/article/pii/S0017931013005115`

Colucci, D.W. and Viskanta, R. (1996). Effect of nozzle geometry on local convective heat transfer to a confined impinging air jet. *Experimental Thermal and Fluid Science*, vol. 13, no. 1, pp. 71–80. ISSN 08941777.

Cooper, D., Jackson, D.C., Launder, B.E. and Liao, G.X. (1993). Impinging jet studies for turbulence model assessment-I. Flow-field experiments. *International Journal of Heat and Mass Transfer*, vol. 36, no. 10, pp. 2675–2684. ISSN 00179310.

Craig, K.J. (2018). Central Receiver Heat Transfer Enhancement Using Jet Impingement with Passive Velocity Excitation. In: *SolarPACES 2018*, pp. 2–9.

Stellenbosch University https://scholar.sun.ac.za

Craig, K.J., Slootweg, M. and Meyer, J.P. (2018). Heat transfer enhancement in molten salt central receiver using jet impingement. In: *5th Southern African Solar Energy Conference (SASEC)*, 1, pp. 1–7. Durban, South Africa.

Faisst, H. and Eckhardt, B. (2004). Sensitive dependence on initial conditions in transition to turbulence in pipe flow. *Journal of Fluid Mechanics*, vol. 504, no. 1, pp. 343–352.

Fluent (2016). Fluent Theory Guide. In: *ANSYS documentation*, 17th edn, chap. 4.7.

Fox, M.D., Kurosaka, M., Hedges, L. and Hirano, K. (1993). The influence of vortical structures on the thermal fields of jets. *Journal of Fluid Mechanics*, vol. 255, pp. 447–472.

Gardon, R. and Akfirat, C. (1965). The role of turbulence in determining the heat-transfer characteristics of impinging jets. *International Journal of Heat and Mass Transfer*, vol. 8, no. 1, pp. 1261–1272.
Available at: `https://www-sciencedirect-com.ez.sun.ac.za/science/article/pii/0017931065900542`

Gau, C. and Chung, C.M. (1991). Surface Curvature Effect on Slot-Air-Jet Impingement Cooling Flow and Heat Transfer Process. *Journal of Heat Transfer*, vol. 113, no. November, pp. 858–864.

Grange, B., Ferriere, A., Nellard, D., Vrinat, M., Couturier, R., Pra, F. and Fan, Y. (2011). Thermal performances of a high temperature air solar absorber based on compact heat exchange technology. *Journal of Solar Energy Engineering*, vol. 133, no. August 2011, pp. 1–11.

Hadziabdic, M. and Hanjalic, K. (2008). Vortical structures and heat transfer in a round impinging jet. *Journal of Fluid Mechanics*, vol. 596, pp. 221–260.
Available at: `https://www.cambridge.org/core/journals/journal-of-fluid-mechanics/article/vortical-structures-and-heat-transfer-in-a-round-impinging-jet/BEE751344193DF18D01C0ABC9E3FFB43`

Heyerichs, K. and Pollard, A. (1996). Heat transfer in separated and impinging turbulent flows. *International Journal of Heat and Mass Transfer*, vol. 39, no. 12, pp. 2385–2400.
Available at: `https://www-sciencedirect-com.ez.sun.ac.za/science/article/pii/0017931095003479`

Ho, C.K., Mahoney, A.R., Ambrosini, A., Bencomo, M., Hall, A. and Lambert, T.N. (2013 jul). Characterization of Pyromark 2500 Paint for High-Temperature Solar Receivers. *Journal of Solar Energy Engineering*, vol. 136, no. 1, pp. 14502–14504. ISSN 0199-6231.
Available at: `http://dx.doi.org/10.1115/1.4024031`

Idelchik, I. (1986). *Handbook of Hydraulic Resistance - Coefficients of Local Resistance and of Friction*. 2nd edn. Hemisphere Publishing Corporation, Moscow. ISBN 0-89116-284-4.

Stellenbosch University https://scholar.sun.ac.za

Jarmillo, J., Trias, F., Gorobets, A., Perez-Segarra, C. and Oliva, A. (2012). DNS and RANS modelling of a turbulent plane impinging jet. *International Journal of Heat and Mass Transfer*, vol. 55, pp. 789–801.
Available at: https://www-sciencedirect-com.ez.sun.ac.za/science/article/pii/S0017931011006004

Jones, W.P. and Launder, B.E. (1973). The calculation of low-Reynolds-number phenomena with a two-equation model of turbulence. *International Journal of Heat and Mass Transfer*, vol. 16, pp. 1119–1130.

Kast, W. (2010). *VDI Atlas Chapter L - Fluid Dynamics and Pressure Drop*. 2nd edn. VDI-Verlag GmbH, Karlsruhe. ISBN 9783540778776.

Kataoka, K., Suguro, M., Degawa, H., Maruo, K. and Mihata, I. (1987). The effect of surface renewal due to large-scale eddies on jet impingement heat transfer. *International Journal of Heat and Mass Transfer*, vol. 30, no. 3, pp. 559–567.

Kerswell, R.R. (2005). Recent progress in understanding the transition to turbulence in a pipe. *Nonlinearity*, vol. 18, no. 1, pp. R17–R44.
Available at: http://chaosbook.org/library/KerswellNonl0305.pdf

Kröger, D.G. (2008). Spiky Central Receiver Air Pre-heater (SCRAP). Tech. Rep., Stellenbosch University, Technical report, Stellenbosch.

Kröger, D.G. (2012). SUNSPOT - The Stellenbosch UNiversity Solar POwer Thermodynamic cycle. Tech. Rep., Stellenbosch University, Stellenbosch.

Kubacki, S. and Dick, E. (2009). Convective heat transfer prediction for an axisymmetric jet impinging onto a flat plate with an improved k-w model. *International Journal of Numerical Methods for Heat & Fluid Flow*, vol. 19, no. 8, pp. 960–981.

Kubacki, S. and Dick, E. (2010). Simulation of plane impinging jets with k-w based hybrid RANS/LES models. *International Journal of Heat and Fluid Flow*, vol. 31, no. 5, pp. 862–878. ISSN 0142-727X.
Available at: http://dx.doi.org/10.1016/j.ijheatfluidflow.2010.04.011

Kubacki, S. and Dick, E. (2011). Hybrid RANS/LES of flow and heat transfer in round impinging jets. *International Journal of Heat and Fluid Flow*, vol. 32, no. 3, pp. 631–651. ISSN 0142-727X.
Available at: http://dx.doi.org/10.1016/j.ijheatfluidflow.2011.03.002

Laufer, J. (1954). The structure of turbulence in fully developed pipe flow. Tech. Rep., NASA.

Lee, D., Chung, Y. and Kim, D. (1997). Turbulent flow and heat transfer measurements on a curved surface with a fully developed round impinging jet. *International Journal of Heat and Fluid Flow*, vol. 18, no. 1, pp. 160–169. ISSN 0142727X.
Available at: http://www.sciencedirect.com/science/article/pii/S0142727X96001361{#}

Stellenbosch University https://scholar.sun.ac.za

Lee, D., Greif, R., Lee, S. and Lee, J. (1995). Heat transfer from a flat plate to a fully developed axisymmetric impinging jet. *Journal of Heat Transfer*, vol. 117, pp. 772–776.

Lee, D.H., Chung, Y.S. and Won, S.Y. (1999). The effect of concave surface curvature on heat transfer from a fully developed round impinging jet. *International Journal of Heat and Mass Transfer*, vol. 42, pp. 2489–2497.

Lee, D.H., Song, J. and Jo, M.C. (2004). The Effects of Nozzle Diameter on Impinging Jet Heat Transfer and Fluid Flow. *Journal of Heat Transfer*, vol. 126, no. August, pp. 554–557. ISSN 00221481.
Available at: `http://heattransfer.asmedigitalcollection.asme.org/article.aspx?articleid=1447330`

Lee, J. and Lee, S.-j. (1999). Stagnation region heat transfer of a turbulent axisymmetric jet impingement. *Experimental Heat Tranfer*, vol. 12, no. 2, pp. 137–156.

Lee, S., Lee, H. and Lee, D. (1994). Heat transfer measurements using liquid crystal with an elliptic jet impinging upon the flat surface. *International Journal of Heat and Mass Transfer*, vol. 37, pp. 967–976.

Lubkoll, M. (2017). *Performance Characteristics of the Spiky Central Receiver Air Pre-heater (SCRAP)*. PhD, Doctoral Thesis, Stellenbosch University.

Lubkoll, M., Harms, T.M. and von Backström, T.W. (2016). Introduction to heat transfer test setup and manufacturing process for the SCRAP receiver. Tech. Rep., Stellenbosch University, Stellenbosch.

Lubkoll, M., Von Backström, T.W. and Harms, T.M. (2015). Performance outlook of the SCRAP receiver. In: *SolarPACES 2015*, vol. 1734, pp. 1–8. ISBN 9780735413863.

Lytle, D. and Webb, B.W. (1994). Air jet impingement heat transfer at low nozzle-plate spacings. *International Journal of Heat and Mass Transfer*, vol. 37, no. 12, pp. 1687–1697.

McDougall, D., von Backström, T., Lubkoll, M. and Sebitosi, B. (2018). Jet impingement heat transfer effect on SCRAP. In: *5th Southern African Solar Energy Conference (SASEC)*, pp. 1–8. Durban, South Africa.

Menter, F.R. (1992). Improved Two-Equation Turbulence Models for Aerodynamic Flows. Tech. Rep., NASA, California.

Menter, F.R. (1993). Zonal Two Equation k-w Turbulence Models for Engineering Applications. In: *24th Fluid Dynamics Conference*, pp. 1–21. AIAA, Orlando.

Menter, F.R., Langtry, R.B., Likki, S.R., Suzen, Y.B., Huang, P.G. and Völker, S. (2004 mar). A Correlation-Based Transition Model Using Local Variables-Part I: Model Formulation. *Journal of Turbomachinery*, vol. 128, no. 3, pp. 413–422. ISSN 0889-504X.
Available at: `http://dx.doi.org/10.1115/1.2184352`

Mills, A. and Ganesan, V. (1999). *Heat Transfer*. 2nd edn. Pearson.

Stellenbosch University https://scholar.sun.ac.za

Öztekin, E., Aydin, O. and Avci, M. (2013). Heat transfer in a turbulent slot jet flow impinging on concave surfaces. *International Journal of Heat and Mass Transfer*, vol. 44, no. 1, pp. 77–82.
Available at: `https://www-sciencedirect-com.ez.sun.ac.za/science/article/pii/S073519331300050X`

Rahimi, M., Owen, I. and Mistry, J. (2003). Heat transfer between an under-expanded jet and a cylindrical surface. *International Journal of Heat and Mass Transfer*, vol. 46, no. 1, pp. 3135–3142.
Available at: `https://www-sciencedirect-com.ez.sun.ac.za/science/article/pii/S0017931003001169`

Rama Kumar, B. and Prasad, B. (2008). Computational flow and heat transfer of a row of circular jets impinging on a concave surface. *Heat Mass Transfer*, vol. 44, pp. 667–678.
Available at: `https://link.springer.com/content/pdf/10.1007%2Fs00231-007-0274-3.pdf`

Reynolds, O. (1895). On the Dynamical Theory of Incompressible Viscous Fluids and the Determination of the Criterion. *Philosophical Transactions of the Royal Society of London*, vol. 186, pp. 123–164.

Samuel, A.E. and Joubert, P.N. (1974). A boundary layer developing in an increasingly adverse pressure gradient. *Journal of Fluid Mechanics*, vol. 66, no. 3, pp. 481–505. ISSN 0022-1120.

Saravanamuttoo, H., Rogers, G. and Cohen, H. (2001). *Gas turbine theory*. 5th edn. Dorling Kindersley Pvt. Ltd., New Delhi.

Sawin, J., Seyboth, K. and Sverrisson, F. (2017). RENEWABLES 2017 GLOBAL STATUS REPORT. Tech. Rep., REN21.
Available at: `http://www.ren21.net/wp-content/uploads/2017/06/17-8399_GSR_2017_Full_Report_0621_Opt.pdf`

Schabel, W. and Martin, H. (2010). Impinging Jet Flow Heat Transfer. In: Stephan, P. (ed.), *VDI Heat Atlas*, 2nd edn, chap. Chapter G1, pp. 745–751. VDI-Verlag GmbH, Karlsruhe. ISBN 9783540778769.

Schobeiri, M.T. (2010). *Fluid Mechanics for Engineers*. 1st edn. Springer-Verlag, Berlin.

Sharif, M. and Mothe, K. (2010). Parametric study of turbulent slot-jet impingement heat transfer from concave cylindrical surfaces. *International Journal of Thermal Sciences*, vol. 49, no. 1, pp. 428–442.

Shuja, S.Z., Yilbas, B.S. and Rashid, M. (2003). Confined swirling jet impingement onto an adiabatic wall. *International Journal of Heat and Mass Transfer*, vol. 46, no. 16, pp. 2947–2955. ISSN 0017-9310.
Available at: `http://www.sciencedirect.com/science/article/pii/S0017931003000735`

SMC (2007). Inconel alloy 718.

Stellenbosch University https://scholar.sun.ac.za

Span, R. (2010). Properties of dry air. In: Stephan, P. (ed.), *VDI Heat Atlas*, 2nd edn, chap. Chapter D2, pp. 172–191. VDI-Verlag GmbH, Bochum, Germany.

Thomann, H. (1968). Effect of streamwise wall curvature on heat transfer in a turbulent boundary layer. *Journal of Fluid Mechanics*, vol. 33, no. 2, pp. 283–292.

Uddin, N., Neumann, S.O. and Weigand, B. (2013). LES simulations of an impinging jet: On the origin of the second peak in the Nusselt number distribution. *International Journal of Heat and Mass Transfer*, vol. 57, pp. 356–368.

Uhlig, R., Gobereit, B. and Rheinländer, J. (2014). Advancing tube receiver performance by using corrugated tubes. In: *SolarPACES 2014*, vol. 69, pp. 563–572. Stuttgart.

White, F. (2009). *Fluid Mechanics*. 7th edn. The McGraw-Hill Companies.

Wilcox, D.C. (1988 nov). Reassessment of the scale-determining equation for advanced turbulence models. *AIAA Journal*, vol. 26, no. 11, pp. 1299–1310. ISSN 0001-1452.
Available at: `https://doi.org/10.2514/3.10041`

Yakhot, V. and Orszag, S.A. (1987). Renormalization group and local order in strong turbulence. *Nuclear Physics B (Proceedings Supplements)*, vol. 2, no. C, pp. 417–440. ISSN 09205632.

Yan, X. (1993). *A Preheated-Wall Transient Method Using Liquid Crystals for the Measurement of Heat Transfer on External Surfaces and in Ducts*. PhD Thesis, University of California, Davis, CA.

Yang, G., Choi, M. and Lee, J.S. (1999). An experimental study of slot jet impingement cooling on concave surface effects of nozzle configuration and curvature. *International Journal of Heat and Mass Transfer*, vol. 42, pp. 2199–2209.

Yap, C. (1987). *Turbulent heat and momentum transfer in recirculating and impinging flows*. Ph.D. thesis.

Zuckerman, N. and Lior, N. (2006). *Jet impingement heat transfer: Physics, correlations, and numerical modeling*, vol. 39. Elsevier Masson SAS. ISBN 0065-2717.
Available at: `http://dx.doi.org/10.1016/S0065-2717(06)39006-5`